

1 Overview of the Chemistry-Aerosol Mediterranean Experiment/Aerosol Direct Radiative
2 Forcing on the Mediterranean Climate (ChArMEx/ADRI-MED) summer 2013 campaign.

3
4 Mallet M.¹, F. Dulac², P. Formenti³, P. Nabat⁴, J. Sciare^{2,5}, G. Roberts⁴, J. Pelon⁶, G. Ancellet⁶, D. Tanré⁷, F.
5 Parol⁷, C. Denjean⁴, G. Brogniez⁷, A. di Sarra⁸, L. Alados⁹, J. Arndt¹⁰, F. Aurio⁷, L. Blarel⁷, T. Bourriane⁵, P.
6 Chazette², S. Chevaillier³, M. Claeys⁵, B. D'Anna¹¹, Y. Derimian⁷, K. Desboeufs³, T. Di Iorio⁸, J.-F. Doussin³, P.
7 Durand¹, A. Féron³, E. Freney¹³, C. Gaimoz³, P. Goloub⁷, J. L. Gómez-Amo⁸, M. J. Granados-Muñoz⁹, N. Grand³,
8 E. Hamonou², I. Jankowiak⁷, M. Jeannot¹⁴, J.-F. Léon¹, M. Maillé³, S. Mailler¹⁵, D. Meloni⁸, L. Menut¹⁵, G.
9 Momboisse⁵, J. Nicolas¹¹, T. Podvin⁷, V. Pont¹, G. Rea¹⁵, J.-B. Renard¹⁴, L. Roblou¹, K. Schepanski¹⁶, A.
10 Schwarzenboeck¹³, K. Sellegri¹³, M. Sicard¹⁷, F. Solmon¹⁸, S. Somot⁵, B. Torres⁷, J. Totems¹, S. Triquet³, N.
11 Verdier¹⁹, C. Verwaerde⁷, J. Wenger¹⁰ and P. Zapf³.

- 12
13 1 Laboratoire d'Aérodynamique, Observatoire Midi-Pyrénées, 14 Avenue Edouard Belin, 31400 Toulouse, France
14 2 LSCE-CEA/IPSL, CEA Saclay 701, 91191 Gif-sur-Yvette, France
15 3 Laboratoire Inter-Universitaire des Systèmes Atmosphériques (LISA), UMR CNRS 7583, Université Paris Est
16 Créteil et Université Paris Diderot, Institut Pierre Simon Laplace, Créteil, France
17 4 Météo-France, CNRM-GAME, Centre national de recherches météorologiques, UMR3589, Toulouse,
18 France
19 5 The Cyprus Institute, Energy Environment and Water Research Center, Nicosia, Cyprus
20 6 LATMOS-ISPL, UPMC Univ. Paris 06; Université Versailles St-Quentin; CNRS/INSU, Paris, France
21 7 LOA, Université Lille 1, Villeneuve d'Ascq, France
22 8 ENEA, Laboratory for Earth Observations and Analyses, Via Anguillarese 301, 00123 Roma, Italy
23 9 Department of Applied Physics, University of Granada, 18071, Granada, Spain
24 10 Department of Chemistry and Environmental Research Institute, University College Cork, Ireland
25 11 Institute de recherches sur la catalyse et l'environnement de Lyon (IRCE Lyon), University of Lyon, 69100
26 Villeurbanne, France
27 12 Leibniz Institute for Tropospheric Research (TROPOS), Permoserstraße 15, 04318, Leipzig, Germany
28 13 Laboratoire de Météorologie Physique CNRS UMR6016, Observatoire de Physique du Globe de Clermont-
29 Ferrand, Université Blaise Pascal, 63171 Aubière, France
30 14 LPC2E-CNRS/Université d'Orléans, 3A avenue de la recherche scientifique, 45071 Orléans, France
31 15 LMD, IPSL, CNRS, Ecole Polytechnique, École Normale Supérieure, Université Paris 6, UMR8539 91128
32 Palaiseau CEDEX, France
33 16 Leibniz Institute for Tropospheric - Research - Permoserstr. 15, 04318 Leipzig, Germany
34 17 RSLab/CTE-CRAE-IEEC, Universitat Politècnica de Catalunya, Barcelona, Spain
35 18 The Abdus Salam International Center for Theoretical Physics, Strada Costiera 11, 34100 Trieste, Italy
36 19 Centre National d'Études Spatiales (CNES), DCT/BL/NB, 18 avenue Edouard Belin, 31401 Toulouse CEDEX
37 9, France

38
39
40
41
42
43
44
45
46
47
48
49
50
51
52
53

54 **Abstract**

55
56 The Chemistry-Aerosol Mediterranean Experiment (ChArMEx; <http://charmex.lsce.ipsl.fr>) is a collaborative
57 research program federating international activities to investigate Mediterranean regional chemistry-climate
58 interactions. A special observing period (SOP-1a) including intensive airborne measurements was performed
59 in the framework of the Aerosol Direct Radiative Forcing on the Mediterranean Climate (ADRIMED) project
60 during the Mediterranean dry season over the western and central Mediterranean basins, with a focus on
61 aerosol-radiation measurements and their modeling. The SOP-1a took place from 11 June to 05 July 2013.
62 Airborne measurements were made by both the ATR-42 and F-20 French research aircraft operated from
63 Sardinia (Italy) and instrumented for in situ and remote-sensing measurements, respectively, and by
64 sounding and drifting balloons, launched in Minorca. The experimental set-up also involved several ground-
65 based measurement sites on islands including two ground-based reference stations in Corsica and
66 Lampedusa and secondary monitoring sites in Minorca and Sicily. Additional measurements including lidar
67 profiling were also performed on alert during aircraft operations at EARLINET/ACTRIS stations at Granada
68 and Barcelona in Spain, and in southern Italy. Remote sensing aerosol products from satellites (MSG/SEVIRI,
69 MODIS) and from the AERONET/PHOTONS network were also used. Dedicated meso-scale and regional
70 modelling experiments were performed in relation to this observational effort. We provide here an
71 overview of the different surface and aircraft observations deployed during the ChArMEx/ADRIMED period
72 and of associated modeling studies together with an analysis of the synoptic conditions that determined the
73 aerosol emission and transport. Meteorological conditions observed during this campaign (moderate
74 temperatures and southern flows) were not favorable to produce high level of atmospheric pollutants nor
75 intense biomass burning events in the region. However, numerous mineral dust plumes were observed
76 during the campaign with main sources located in Morocco, Algeria and Tunisia, leading to aerosol optical
77 depth (AOD) values ranging between 0.2 to 0.6 (at 440 nm) over the western and central Mediterranean
78 basins. One important point of this experiment concerns the direct observations of aerosol extinction on-
79 board the ATR-42, using CAPS system, showing local maxima reaching up to 150 Mm^{-1} within the dust
80 plume. Non negligible aerosol extinction (about 50 Mm^{-1}) was also been observed within the Marine
81 Boundary Layer (MBL). By combining the ATR-42 extinction coefficient observations with absorption and

82 scattering measurements, we performed a complete optical closure revealing excellent agreement with
83 estimated optical properties. This additional information on extinction properties has allowed calculating
84 the dust single scattering albedo (SSA) with a high level of confidence over the Western Mediterranean. Our
85 results show a moderate variability from 0.90 to 1.00 (at 530 nm) for all flights studied that is contrary to
86 the available literature on this optical parameter. Our results underline also a relatively low difference in SSA
87 with values derived near dust sources. In parallel, active remote-sensing observations from the surface and
88 onboard the F-20 aircraft suggest a complex vertical structure of particles and distinct aerosol layers with
89 sea-spray and pollution located within the MBL, and mineral dust and/or aged north American smoke
90 particles located above (up to 6-7 km in altitude). Aircraft and balloon-borne observations allow to
91 investigate the vertical structure of aerosol size distribution showing particles characterized by large size
92 ($>10\ \mu\text{m}$ in diameter) within dust plumes. In most of cases, a coarse mode characterized by an effective
93 diameter ranging between 5 and $10\ \mu\text{m}$, has been detected above the MBL. In terms of shortwave (SW)
94 direct forcing, in-situ surface and aircraft observations have been merged and used as inputs in 1-D radiative
95 transfer codes for calculating the direct radiative forcing (DRF). Results show significant surface SW
96 instantaneous forcing (up to $-90\ \text{W m}^{-2}$ at noon). Aircraft observations provide also original estimates of the
97 vertical structure of SW and LW radiative heating revealing significant instantaneous values of about 5°K per
98 day (in the solar spectrum (for a solar angle of 30°) within the dust layer. Associated 3-D modeling studies
99 from regional climate (RCM) and chemistry transport (CTM) models indicate a relatively good agreement for
100 simulated AOD compared with observations from the AERONET/PHOTONS network and satellite data,
101 especially for long-range dust transport. Calculations of the 3-D SW (clear-sky) surface DRF indicate an
102 average of about -10 to $-20\ \text{W m}^{-2}$ (for the whole period) over the Mediterranean Sea together with maxima
103 ($-50\ \text{W m}^{-2}$) over northern Africa. The top of the atmosphere (TOA) DRF is shown to be highly variable within
104 the domain, due to moderate absorbing properties of dust and changes in the surface albedo. Indeed, 3-D
105 simulations indicate negative forcing over the Mediterranean Sea and Europe and positive forcing over
106 northern Africa. Finally, a multi-year simulation, performed for the 2003 to 2009 period and including an
107 ocean-atmosphere (O-A) coupling, underlines the impact of the aerosol direct radiative forcing on the sea
108 surface temperature, O-A fluxes and the hydrological cycle over the Mediterranean.

109 **1. Introduction**

110 The Mediterranean region has been identified as one of the most prominent “Hot-Spots” in future climate
111 change projections (Giorgi and Lionello, 2008). It is characterized by its vulnerability to changes in the water
112 cycle (e.g. Chenoweth et al., 2011; García-Ruiz et al., 2011). General Circulation Model (GCM) and Regional
113 Climate Model (RCM) simulations show a substantial precipitation decrease and a warming of the region,
114 especially in the long warm and dry Mediterranean season. At the end of 21st century, the average of the
115 model outputs predicts a significant loss of freshwater (+40% for the period 2070-2090 compared to 1950-
116 1999; Sanchez-Gomez et al, 2009) over the Mediterranean region. More recently, Mariotti et al. (2015) have
117 used the newly available Coupled Model Intercomparison Project-Phase 5 (CMIP5) experiments and show a
118 significant increase of the projected surface air temperature (by ~+ 2-3 °C) for the 2071-2098 period
119 compared to 1980-2005. These results need to be put in the context of an increasing anthropogenic
120 pressure on the Mediterranean region, with an expected doubling of the population in countries around the
121 Mediterranean basin in the next decades, with a contrast between a small decrease in European countries
122 and a strong increase in African and Middle-East countries (Brauch, 2003). However, as highlighted by
123 Mariotti et al. (2008), despite the high degree of model consistency, the results concerning the future
124 climate projections for the Mediterranean Sea water budget from the global coupled models are still
125 uncertain due to their horizontal spatial resolutions that are not capable of resolving the local to regional
126 Mediterranean specific processes (air-sea exchanges, coastline, topography, north-south gradient of
127 albedo). Indeed, the Mediterranean climate is affected by local processes induced by the complex
128 physiography of the region and the presence of a large body of water (the Mediterranean Sea). For example,
129 the Alpine chain is a strong factor in modifying traveling synoptic and mesoscale systems and the
130 Mediterranean Sea is an important source of moisture and precipitation in the region (Gimeno et al., 2010;
131 Schicker et al., 2010) and of energy for storms (Lionello et al., 2006). The complex topography, coastline and
132 vegetation cover of the region are well known to modulate the regional climate signal at small spatial scales
133 (e.g. Millan et al., 1997; Gangoiti et al., 2001; Lionello et al., 2006).

134 So far, most global and regional climate simulations have investigated the impact of global warming on the
135 Mediterranean climate without detailed considerations of the possible radiative influence and climatic

136 feedback from the different Mediterranean aerosols (anthropogenic, marine, biomass burning, secondary
137 biogenic and mineral dust particles). The Mediterranean region is rich in a variety of particles (natural and
138 anthropogenic) from both continental and marine sources (Lelieveld et al., 2002). In figure 1, we illustrate
139 the significant differences in aerosol loading between the eastern, central, and western sub-basins and
140 between the North and the South of the Mediterranean shown by long-term aerosol satellite products. The
141 aerosol optical depth (AOD), which represents the integration of the extinction by particles along the whole
142 atmospheric column displays annual mean values (Figure 1) from 0.2 to 0.5 (in the visible wavelengths),
143 depending on the aerosol types observed over the Euro-Mediterranean region (Nabat et al., 2013).

144 Numerous studies have documented the AOD for polluted-anthropogenic Mediterranean aerosols at local
145 scale over southeastern France (Mallet et al., 2006; Roger et al., 2006), Spain (Horvath et al., 2002, Alados-
146 Arboledas et al., 2003, 2008), Western Mediterranean (Lyamani et al., 2015), Greece (Chazette and Liousse,
147 2001; Gerasopoulos et al., 2003), the Greek island of Crete (Fotiadi et al., 2006), and Italy (Tafuro et al.,
148 2007, Ciardini et al., 2012). Under polluted conditions, they report low to moderate AOD values ranging
149 between 0.1 to 0.5 (at visible wavelengths). In parallel, multi-year TOMS and MODIS observations over the
150 eastern Mediterranean (Hatzianastassiou et al., 2009) or the Po Valley (Royer et al., 2010) indicate the
151 occurrence of high AOD values (up to more than 0.8 at 500 nm) over large urban areas surrounding
152 megacities.

153 Numerous studies (Markowicz et al. (2002), Ravetta et al. (2007), Liu et al. (2009), Kaskaoutis et al. (2011),
154 Barnaba et al. (2011), Amiridis et al. (2012), Baldassarre et al. (2015)) have been also dedicated to biomass
155 burning aerosols over the Mediterranean, which are mainly observed in July and August (driest months of
156 the year) when the development of forest fires is favoured (Pace et al., 2005). Long-term observations of
157 absorbing aerosols have clearly shown the major role of long range transport of biomass (agriculture waste)
158 burning in the eastern Mediterranean (Sciare et al., 2008). AOD data available for smoke particles show
159 “intermediate” values between those observed for dust and anthropogenic particles. For example, AOD
160 ranging between 0.3 and 0.8 (Pace et al., 2005) have been observed at Lampedusa from 5 to 22 August
161 2003, in relation with intense fires developed in southern Europe and transported over the Mediterranean
162 basin during a regional heat wave. In addition, the STAAARTE-MED experiment (August 1998 in the Eastern

163 Mediterranean) has also documented a mean AOD of 0.39 (at 550 nm) for aged smoke plume from
164 Canadian fires (Formenti et al., 2002). This kind of long-range transport has been also observed over the
165 Western Mediterranean (Ortiz-Amezcuca et al., 2014).

166 Concerning natural aerosols, different cases of Saharan mineral dust have been regularly documented with
167 local optical measurements on the island of Lampedusa by Meloni et al. (2003, 2004), who indicate
168 moderate AOD (at 415.6 nm) of about 0.23-0.26 and one significantly larger event with AOD values of 0.51.
169 Meloni et al. (2008) also report AOD (at 500 nm) measurements ranging between 0.29 and 1.18 for the
170 1999 to 2006 period. For some extreme cases, dust AOD peaks may be even larger reaching values up to 2
171 as observed by di Sarra et al. (2011). In parallel to Lampedusa observations, Kubilay et al. (2003) have also
172 documented three dust intrusion events at Erdemli (Turkish coast), occurring in spring from central Sahara,
173 in summer from eastern Sahara, and in autumn from the Middle East/Arabian peninsula. In each case, the
174 presence of dust particles significantly increased the AOD, up to 1.8. Over the western Mediterranean,
175 different studies also reveal the impact of Saharan dust that occasionally can lead to extreme events with
176 AOD (at 500 nm) above 1 (Guerrero-Rascado et al., 2009).

177 For sea-spray particles, which are the second main natural species observed over the Mediterranean, Nabat
178 et al. (2013) report a relatively low monthly mean AOD derived from satellites and modeling data, with
179 values lower than 0.05 (in the visible wavelengths). By using recent improvements in the sea-spray emission
180 scheme, Spada et al. (2013) show an averaged sea-spray AOD around 0.04 for the month of January (5 year
181 period, 2002-2006) which is the favourable period for generating primary sea-spray due to strong sea-
182 surface winds. Finally, and in the case of extreme wind episodes occurring over the western basin, Salameh
183 et al. (2007) show that the amount of aerosol loading, solely due to the Mistral, Tramontane and Ligurian
184 outflows, is as large as 3–4 times the background aerosol amount. They indicate that the contribution of
185 sea-spray particles to the total aerosol loading and optical depth ranges from 1 to 10%. Salameh et al.
186 (2007) report AOD around 0.15-0.20 (at 865 nm) within the sea-spray aerosol plume during such strong
187 wind events. In addition, Mulcahy et al. (2008) reported a high correlation between AOD and wind-speed
188 with AOD values of 0.3-0.4 at moderately-high wind speed.

189 In addition to AOD, the knowledge of SSA is essential to estimate the aerosol direct and semi-direct

190 radiative forcing. Concerning mineral dust particles observed over the Mediterranean, it should be noted
191 that significant variations in SSA are reported, with values near 1 for purely scattering aerosols, and quite
192 remarkable low values (0.74, 0.77 or 0.81) at Lampedusa (Pace et al., 2006; Meloni et al., 2003). At the high
193 altitude Alpine Jungfrauoch station, SSA values are generally higher than 0.9 in case of African dust but
194 occasional SSA as low as 0.75-0.80 are reported by Collaud-Coen et al. (2004). Intermediate values (0.85-
195 0.92) have been also reported over the Mediterranean basin (Kubilay et al., 2003; Meloni et al., 2004; Saha
196 et al., 2008). These estimates clearly indicate that significantly different SSA values are obtained following
197 the dust particle origins and/or possible mixing of mineral dust with other species. For example, Kubilay et
198 al. (2003) underlined the importance of mixing, showing SSA values clearly lower (0.85-0.90) in case of
199 mineral dust transport coincident with urban-industrial aerosols, as compared to pure dust (0.96-0.97).

200 In addition, SSA observed in case of urban/industrial regimes has been also well documented over the
201 Mediterranean Sea and coastal regions. In most cases, moderate or low SSA (0.78-0.94) is observed due to
202 emissions containing absorbing black carbon aerosols. Over southeastern France, optical computations
203 performed by Saha et al. (2008) and Mallet et al. (2004) indicate SSA values of 0.83 and 0.85 (at 550 nm)
204 near the cities of Marseille and Toulon, respectively. Aircraft observations performed over the
205 Marseille/Etang de Berre area during the ESCOMPTE campaign show values ranging between 0.88 and 0.93
206 (at 550 nm) in the PBL (Mallet et al., 2005). These SSA values are close to those observed in South Spain
207 (0.86-0.90) by Horvarth et al. (2002). Over southeastern Italy, Tafuro et al. (2007) reported a value of 0.94
208 during summer time corresponding to anthropogenic particles. Finally, polluted particles transported over
209 the Mediterranean basin have also relatively low values as reported by Markowick et al. (2002) over Crete
210 Island (0.87) and by Di Iorio et al. (2003) (0.79-0.83) over the Lampedusa Island for two cases (25 and 27
211 May 1999) of "aged" anthropogenic aerosols originating from Europe.

212 As opposed to dust and polluted aerosols, few studies have derived the biomass burning SSA over the
213 Mediterranean Sea. One estimate has been obtained during STAAARTE-MED by Formenti et al. (2002) who
214 reported a mean dry SSA of 0.89 (at 500 nm) for aged smoke from North America. Meloni et al. (2006)
215 report estimations at Lampedusa with values of 0.82 ± 0.04 (at 415 nm) for smoke aerosols over the
216 Mediterranean region. The observed differences between SSA values could be due to the fact that the

217 smoke events described by Meloni et al. (2006) are more “local” and not (or somewhat less) mixed with
218 other secondary species, as compared to biomass burning particles documented by Formenti et al. (2002),
219 which were issued from very distant Canadian fires. Finally, at Palencia (Spain), Cachorro et al. (2008)
220 reported a column-integrated SSA of 0.88 (at 440 nm) for a biomass burning event occurring in July 28,
221 2004. It should be remained that most estimations of SSA over the Mediterranean have been obtained from
222 surface in-situ or remote-sensing techniques. In that sense, the ChArMEx/ADRIMED project provides
223 innovative observations of 3-D aerosol SSA, allowing investigating changes in its optical property during the
224 transport of aerosols over the Mediterranean.

225 Concerning the aerosol vertical profiles and apart from a few airborne in-situ measurements (Formenti et
226 al., 2002), most of the available information in the Mediterranean region comes from lidar observations,
227 which provide highly resolved vertical profiles of aerosol backscattering at one or more wavelengths and,
228 depending on the complexity of the instrumental setup, particles depolarization and extinction. Several
229 sites are equipped with aerosol lidar systems and carry out regular observations in a coordinated way within
230 the European aerosol research lidar network EARLINET (European Aerosol Research Lidar Network;
231 Pappalardo et al., 2014; Wang et al., 2014). Numerous studies have been specifically dedicated to the
232 vertical distribution of Saharan dust during extended time periods and/or selected events from various
233 Mediterranean regions, mainly from ground-based systems: (i) the eastern basin in Thessaloniki (Hamonou
234 et al., 1999; Balis et al., 2004), Crete (Balis et al., 2006), the Aegean sea (Dulac et al., 2003), and Athens plus
235 Thessaloniki (Papayannis et al., 2005; Balis et al., 2006); (ii) the central basin in Lampedusa (Di Iorio et al.,
236 2003; Meloni et al., 2004), Lecce (Tafuro et al., 2006), and at Etna (Tafuro et al., 2006); and (iii) across the
237 western basin with the first spaceborne lidar (Berthier et al., 2006) and at Observatoire de Haute Provence
238 (Hamonou et al., 1999), and Barcelona (Pérez et al., 2006; Sicard et al., 2011). Finally, using data from 20
239 EARLINET lidar stations, Papayannis et al. (2008) indicate that African dust transport over the Mediterranean
240 basin is layered. Their analysis confirms early observations by Hamonou et al. (1999) that not only different
241 dust layers are superimposed at different altitudes, but that these layers have different source regions. The
242 dust layers were generally detected between 1.8 and 9 km altitude.

243 Not only desert dust, however, can be transported above the marine atmospheric boundary layer. Balis et

244 al. (2004) report non-dust aerosols within elevated layers over Thessaloniki, and Formenti et al. (2002)
245 report a forest fire haze layer from Canada observed from airborne measurements between approximately
246 1 and 3.5 km above the northeastern Mediterranean in August 1998. Pérez et al. (2004) describe the
247 complex interaction among orography, sea-breeze and pollution that cause the recirculation of pollutants
248 and produce a strong layering with pollution aerosol layers above the boundary layer in the region of
249 Barcelona. In addition, aerosol plumes are emitted sporadically in the Mediterranean free troposphere by
250 Etna volcano. Such plumes have been observed to travel at altitudes between 4 and 5 km (Pappalardo et al.,
251 2004) or above (Sellitto et al., 2015) at relatively short distance from Etna. To summarize, the lidar
252 observations clearly show that only part of the aerosol transport occurs in the MBL demonstrating the need
253 of using aircraft observations within the aerosol plume to determine the aerosol microphysical-chemical
254 and optical properties of particles transported in altitude and so not detectable at the surface. Indeed,
255 although lidar observations provide obviously crucial information on the aerosol vertical profiles, most of
256 lidar systems cannot derive information on the aerosol size distribution, optical properties and chemical
257 composition along the vertical. Such observations can only be obtained using in-situ aircraft vertical profiles
258 as proposed in this ChArMEx/ADRIMED experiment. As an example, this project provides interesting and
259 unique observations of 3-D aerosol size distribution during the transport over the Mediterranean basin,
260 allowing to investigate changes in size distribution between mixed and pure mineral dust.

261 In terms of radiative effects, such atmospheric aerosol characteristics (loadings, absorbing properties,
262 vertical layering) are known (Nabat et al., 2012; Papadimas et al., 2012; Zanis et al., 2012) to significantly
263 change the radiative budget of the Mediterranean region by (1) decreasing the sea-surface incoming
264 shortwave radiations, (2) increasing/decreasing outgoing shortwave fluxes depending on the surface albedo
265 and (3) possibly heating turbid atmospheric layers when particles absorb solar light. This is the so-called
266 aerosol "Direct Radiative Forcing (DRF)". As for the AOD, many of the aerosol DRF calculations are now
267 referenced over the Mediterranean clearly showing that the DRF is significantly larger at daily time scales
268 than the one exerted by the additional anthropogenic greenhouse gases.

269 Concerning polluted aerosols, shortwave DRF have been estimated by many authors (Horvath et al., 2002;
270 Markowicz et al., 2002; Meloni et al., 2003; Roger et al., 2006; Mallet et al., 2006; Saha et al., 2008; di Sarra

271 et al., 2008; Di Biagio et al., 2009, 2010). Studies show significant decreases of surface solar fluxes of about
272 $20\text{-}30\text{ W m}^{-2}$ (daily mean) for different locations as Almeria (South Mediterranean coast of Spain), Finokalia
273 (Crete Island), Lampedusa, Marseilles and Toulon (southeastern France). In parallel, the combination of
274 surface and satellite remote-sensing observations performed at Lampedusa have been used to perform
275 calculations of the DRF, both in the shortwave (SW; Di Biagio et al., 2010) and longwave (LW; di Sarra et al.,
276 2011; Meloni et al., 2015) spectral regions for different cases of Saharan dust intrusions. These studies
277 emphasize that the radiative effect of desert dust in the LW spectral range is significant, and offsets a large
278 fraction of the SW forcing (di Sarra et al., 2011; Meloni et al., 2015). More recently, Sicard et al. (2014a,
279 2014b) have also produced estimations of the dust LW radiative effect, based on remote-sensing
280 observations in Barcelona and 1-D radiative transfer calculations.

281 Concerning the smoke DRF, some calculations have been conducted over the Mediterranean region by
282 Markowicz et al. (2002), di Sarra et al. (2008), Kaskaoutis et al. (2011) or Formenti et al. (2002). One
283 estimate, proposed by Formenti et al. (2002) for an aged Canadian biomass-burning plume, reveals a
284 significant SW surface dimming of about $\sim 60\text{ W m}^{-2}$. In addition, the DRF induced by smoke aerosols at
285 Lampedusa between 3 and 23 August 2003, during the exceptionally hot and dry season, was derived by
286 Pace et al. (2005) for the 300-800 nm spectral range. The smoke atmospheric forcing was estimated to be
287 between $+22$ and $+26\text{ W m}^{-2}$, with a corresponding SW heating rate possibly exceeding 2 K d^{-1} at the smoke
288 plume altitude.

289 At the regional scale, Papadimas et al. (2012) have proposed a recent estimation of the aerosol DRF using
290 MODIS data from 2000 to 2007 for both all-sky and clear-sky conditions. They derived a multi-year regional
291 mean surface of -19 W m^{-2} , associated with a TOA DRF of -4.5 W m^{-2} . Regional modelling studies have been
292 also recently proposed by Nabat et al. (2012, 2015a) using the coupled-chemistry RegCM and the CNRM-
293 Regional Climate System Model (RCSM) models for multi-year simulations. These works reported a mean
294 regional surface (TOA) forcing of about -12 W m^{-2} (-2.4 W m^{-2}) and -16 W m^{-2} (-5.7 W m^{-2}) for the RegCM and
295 CNRM-RCSM models, respectively. RegCM has been also used to investigate direct and semi-direct radiative
296 effects of mineral dust over the Sahara and Europe in a test case of July 2003 (Santese et al., 2010). In this
297 work, Santese et al. (2010) computed a daily-mean SW DRF of -24 W m^{-2} (resp. -3.4 W m^{-2}) on 17 July and -

298 25 W m^{-2} (-3.5 W m^{-2}) on 24 July at the surface (TOA) on average over the simulation domain. Zanis et al.
299 (2012) also proposed a regional estimate of the DRF of anthropogenic particles over the 1996-2007 period
300 using RegCM and showed a significant forcing of up to -23 W m^{-2} at TOA over Eastern Europe. In addition,
301 Pere et al. (2011) have used the CTM-CHIMERE model coupled to the WRF model, for estimating the DRF of
302 anthropogenic particles during the heat wave of summer 2003 and showed significant effects with
303 implications on the planetary boundary layer height (decrease up to 30% in the presence of anthropogenic
304 aerosols) and local air-quality. In addition to their important effects on the surface and TOA DRF, most of
305 the Mediterranean aerosols are also able to absorb more or less effectively the solar radiations leading to a
306 significant atmospheric forcing and associated SW heating rate. Local studies previously mentioned (Roger
307 et al., 2006; Saha et al., 2008; Pace et al., 2005; Pere et al., 2011; Meloni et al., 2015) clearly report
308 significant SW heating rate due to absorbing particles with values reaching up to 2-3 K per day, depending
309 on the aerosol types. Finally, aerosols also have a significant effect on photolysis rates that may affect
310 tropospheric chemistry and ozone production over the basin (Casasanta et al., 2011, Mailler et al., 2015).

311 In regards to such surface, TOA and atmospheric forcings, there is a need to investigate how the change in
312 the radiative budget due to natural/anthropogenic aerosols influence the surface temperature (both over
313 land and sea), relative humidity profiles, exchanges (latent heat fluxes) between ocean and atmosphere,
314 cloud-cover (semi-direct effect of absorbing particles), precipitation and finally the whole Mediterranean
315 hydrological cycle. The induced perturbations in the sea surface-atmosphere fluxes is expected to be
316 important despite the relatively small size of the Mediterranean Sea, since this basin plays an important role
317 at much larger scale by providing moisture for precipitation to its surroundings land region extending to
318 northern Europe and northern Africa (Gimeno et al., 2010 and Schicker et al., 2010). Indeed and as shown
319 by Ramanathan et al. (2001) for the Indian region or Foltz and McPhaden (2008) and Yue et al. (2011) for
320 the Atlantic Ocean, a modification of the sea-surface evaporative fluxes, due to the dimming radiative effect
321 of aerosols at the sea surface could significantly influence the lower troposphere moisture content and the
322 associated precipitation distribution around the Mediterranean. In parallel, the absorbing particles over the
323 Mediterranean (Mallet et al., 2013) could exert a semi-direct effect that could modify the vertical profiles of
324 relative humidity and cloud cover, which has to be quantified. To our knowledge, there is no regional

325 climate simulation over the Mediterranean basin at this time that includes an Ocean-Atmosphere (O-A)
326 coupled system model for investigating this specific question.

327 In that context of the referenced modelling and observations researchs over the Mediterranean basin, the
328 main objectives of the ChArMEx/ADRIMED project were the following:

- 329 - to conduct an experimental campaign, based on surface and aircraft observations, for creating a rich 3-D
330 database of physical, chemical and optical properties of the main Mediterranean aerosols, including (i)
331 original in-situ aircraft observations of extinction coefficients, size distribution, black carbon concentrations
332 as well as (SW and LW) radiative fluxes and associated heating rates, (ii) balloons observations of aerosol
333 size distribution and (iii) surface measurements including original characterization of chemical properties
- 334 - to investigate how the aerosol size distribution and optical (especially SSA) properties evolve along the
335 vertical, between the MBL and elevated layers, and during the transport over the Mediterranean
- 336 - to use experimental surface and aircraft observations to estimate the 1D-local DRF and forcing efficiency
337 of different aerosols at the surface, TOA and within the atmospheric layer
- 338 - to investigate how the modifications of the radiative budget due to aerosols affect the sea-surface
339 evaporation fluxes, relative humidity profiles, cloud-cover, precipitation and more largely the
340 Mediterranean hydrological cycle

341 The present article describes the experimental setup of the campaign and the meteorological context and
342 illustrates important results detailed in a series of companion papers. The rest of this article is divided into
343 six different parts. In the first and second part (sections 2 & 3), we describe the in-situ and remote-sensing
344 instrumentation deployed at the two super sites (Ersa and Lampedusa) and secondary sites (Minorca, Capo
345 Granitola and the Barcelona and Granada EARLINET/ACTRIS stations), the additional AERONET/PHOTONS
346 (AErosol RObotic NETwork / PHOtométrie pour le Traitement Opérationnel de Normalisation Satellitaire,
347 <http://aeronet.gsfc.nasa.gov/>; Holben et al., 1998) and EARLINET/ACTRIS (European Aerosol Research Lidar
348 Network / Aerosols, Clouds, and Trace gases Research InfraStructure Network, <http://www.actris.net/>;
349 Pappalardo et al., 2014) network stations that we used, and the airborne observations obtained onboard
350 the two French research aircraft (ATR-42 and F-20) and with sounding and drifting balloons. The section 4 is
351 dedicated to present the main meteorological conditions, cloud cover and precipitation, which controlled

352 the aerosol emission and transport during the period of observations. The section 5 presents some
353 examples of results concerning the in-situ and remote-sensing observations, in terms of aerosol physical,
354 chemical, optical properties, and vertical profiles, as well as 1-D DRF SW and LW calculations. In the last part
355 (section 6), the modelling effort is presented. Different models are involved in this project, from high
356 resolution meteorological and chemistry transport models to regional climate models. The modelling results
357 are used to describe the anthropogenic (carbonaceous, secondary inorganic and organic species) and
358 natural (dust and sea-spray) loading and the estimated DRF at the regional scale for the period of
359 experiment. An example of results of longer (inter-seasonal and inter-annual) aerosol-climate simulations is
360 presented in the section 6, based on the work of Nabat et al. (2015a).

361 **2. Overview of the surface observation network**

362 The regional experimental set-up deployed in the western and central Mediterranean during the campaign
363 ChArMEx SOP-1a is shown in Figure 2. Two super sites (Cape Corsica and Lampedusa) and 10 secondary
364 sites (Figure 2) have been used in this project.

365 **2.1 The Cape Corsica and Lampedusa surface super sites**

366 Two super-sites were fully equipped for documenting the aerosol chemical, physical and optical properties
367 as well as their possible mixing and their vertical structure at local scale (Table 1). The main characteristics
368 of these two surface stations are presented here. The first station was located in Erba on Cape Corsica
369 ($42^{\circ}58'10''\text{N}$, $09^{\circ}22'49''\text{E}$), near the North tip of Corsica Island. This station was primarily instrumented for
370 investigating polluted air masses transported over the Mediterranean basin from the highly industrialized
371 regions of the Po Valley (Royer et al., 2010) and/or the Marseille-Fos-Berre (Cachier et al., 2005) zone and
372 Rhone Valley. This ground-based remote station is located at an altitude of about 530 m above mean sea
373 level (amsl) on a ridge equipped with wind mills and benefit from a direct view to the sea over a North
374 sector of $\sim 270^{\circ}$ extending from the SW to SE. The Cape Corsica peninsula is a remote site ensuring that the
375 in-situ measurements are not contaminated by local anthropogenic pollution.

376 The Lampedusa super-site ($35^{\circ}31'5''\text{N}$, $12^{\circ}37'51''\text{E}$) was established at the “Roberto Sarao” station
377 permanently operated by ENEA in the small island of Lampedusa ($\sim 20 \text{ km}^2$), and it was augmented during
378 the field campaign by the observations of the Portable Gas and Aerosol Sampling UnitS (PEGASUS) mobile

379 station operated by LISA . This surface station was mainly used for documenting very aged air masses in
380 south westerly flow from Europe, southern air masses from northern Africa (Tunisia, Algeria and Libya)
381 possibly laden with mineral dust, as well as marine aerosols. It is situated on a cliff at about 45 m amsl on
382 the NE tip of the island.

383 The complete instrumentation deployed during the SOP-1a experiment for both super-sites is detailed in
384 Table 1. Briefly, it served to determine the complete aerosol physical, chemical and optical properties as
385 well as vertical profiles, and to measure radiative fluxes (broadband SW and LW, and spectral SW).

386 **2.1.1 In situ measurements at super-sites**

387 Both super-sites measured the mass concentration online using Tapered Element Oscillating Microbalance
388 (TEOM) analysers. The number size distribution of particles are also measured, including fine and coarse
389 fractions (radius ranges and corresponding instruments are reported in Table 1). The aerosol composition
390 was derived from chemical analyses of filters and cascade impactors (DEKATI and MOUDI) with time
391 resolution varying from 12 to 48h (depending on the aerosol load), but also from high-time resolution
392 online measurements by an ACSM (Aerosol Chemical Speciation Monitor) at Ersa, a C-TOF-AMS (Time of
393 Flight Aerosol Mass Spectrometer) at Lampedusa, and two PILS (Particle Into Liquid Sampler) systems at
394 both sites (Table 1). The original observations of aerosol chemical properties obtained from PM10-PILS
395 instrument at Ersa are detailed in Claeys et al. (2015). Concerning aerosol optical properties, scattering and
396 absorption coefficients (at wavelengths listed in table 1) have been estimated for both super-sites using a 3-
397 λ nephelometer and a 7- λ aethalometer, respectively. At Ersa station, the extinction coefficient (at 870 nm)
398 was also estimated using a Photoacoustic Extinctionmeter (PAX) instrument, while it has been estimated at 2-
399 λ (450 and 630 nm) at Lampedusa using 2 Cavity Attenuated Phase Shift Spectroscopy (CAPS) systems.

400 Additional in-situ measurements were performed at the Ersa station. The mixing state of fine particles (at
401 the two selected diameters of 50 and 110 nm in dry conditions) has also been estimated from their
402 hygroscopic behaviour using a VHTDMA (volatilization and humidification tandem differential mobility
403 analyser) system (Johnson et al., 2004). In parallel, a TSI (model 3800) aerosol time of flight mass
404 Spectrometer (ATOFMS) (Gard et al., 1997) was used to measure the size-resolved chemical composition of
405 single particles in the vacuum aerodynamic diameter (d_{va}) size range 100–3000 nm.

406 **2.1.2 Remote sensing and radiation measurements at super-sites**

407 A Leosphere Raman lidar model RMAN510 was setup at low altitude (~11 m above sea level) in the small
408 village of Macinaggio (42°57'44"N, 9°26'35"E) located on the eastern coast of Cape Corsica. The lidar was
409 operated at about 6 km East from the Ersa station and less than 700 m from the shoreline. The RMAN510
410 uses a laser emitting at 355 nm. It measures the total and polarized backscatter at 355 nm and the Raman
411 nitrogen signal at 387 nm at night-time. A second ALS300 510 lidar system has been deployed in Lampedusa
412 (Formenti et al., in prep.) as well as a more powerful University of Rome-ENEA homemade lidar measuring
413 backscatter at 532 and 1064 nm (Di Iorio et al., in prep.). The main characteristics of lidar systems are
414 provided and detailed in Table 1.

415 At each station, a multi-wavelength sun-photometer from the AERONET/PHOTONS network was operated,
416 allowing the operational retrieval of column integrated AOD at 340, 380, 440, 500, 675, 870, 1020 nm (and
417 also at 1650 nm at Ersa) and aerosols optical and microphysical properties such as the single scattering
418 albedo, refractive index and particle size volume distribution (Dubovik and King, 2000; Dubovik et al., 2000,
419 2002, 2006). The Ersa sun-photometer is positioned since June 2008 near the navy semaphore on the
420 northwestern tip of Cape Corsica (43°00'13"N, 09°21'33"E, alt. ~75 m amsl) at about 4.2 km NNW of the
421 Ersa surface station.

422 Both super-sites were complemented by a pyrgeometer and a pyranometer for monitoring longwave and
423 shortwave downward fluxes measurements, respectively. Additional radiation measurements were
424 performed at Lampedusa (Table 1). Spectral measurements of global, diffuse, and direct radiation were
425 carried out with other instruments deployed by ENEA and the Physikalisch-Meteorologisches
426 Observatorium Davos, World Radiation Center, (PMOD/WRC, Switzerland). Multi-filter rotating
427 shadowband radiometer observations were carried out jointly with AERONET sun-photometer (di Sarra et
428 al., 2015) and allowed the derivation of the AOD at several wavelengths. By combining these two
429 measurements, a long-term series of AOD, started in 2001, was obtained. Measurements of the spectral
430 actinic flux, allowing the determination of the photolysis rates (Mailler et al., 2015), were carried out with a
431 diode array spectrometer. Measurements of broadband irradiance included a CG3 pyrgeometer sensitive to
432 radiation in the atmospheric infrared window. Finally, the total ozone and spectral UV irradiance were

433 obtained with a Brewer spectrophotometer. Several radiosondes were also launched from Lampedusa
434 during the SOP-1a, and vertical profiles of temperature and humidity were continuously measured by a
435 microwave radiometer.

436 **2.2 The secondary sites**

437 **2.2.1 Montesorro station**

438 The Cape Corsica station was complemented by an additional remote-sensing setup at the peri-urban air
439 quality station of Montesorro, southward of Bastia at about 45 m amsl (Leon et al., 2015), including a
440 Leosphere model EZ lidar operating at 355 nm (42°40'17"N, 09°26'05"E) and a Cimel AERONET/PHOTONS
441 sun-photometer (42°40'19"N, 09°26'06"E). In addition, some air-quality parameters were monitored by
442 Qualitair Corse, including PM_{2.5} and PM₁₀. This station is less than 1 km far from the shore on the
443 northeastern coast of Corsica, about 32 km South of Macinaggio.

444 **2.2.2 Barcelona station**

445 The Barcelona station (41.39°N, 2.11°E, 115 m amsl) was equipped with the following fixed instruments
446 including an AERONET sun-photometer, an automated Sigma Space-NASA Micro Pulse Lidar (MPL) and a
447 Universitat Politècnica de Catalunya (UPC) home-made multi-wavelength lidar (Kumar et al., 2011). The MPL
448 lidar works at 532 nm and has a depolarization channel, while the UPC lidar works at 355, 532 and 1064 nm,
449 and also includes two N₂- (at 387 and 607 nm) and one H₂O-Raman (at 407 nm) channels. The MPL system
450 worked continuously. The UPC system was operated on alert in coordination with the two research aircraft
451 plans involved in the SOP-1a campaign. The UPC system is part of the EARLINET network.

452 **2.2.3 Minorca station**

453 An additional station was setup during the campaign, located at Cap d'en Font, on the southeastern coast of
454 the Balearic island of Minorca (Spain, 39°53'12"N and 4°15'31" E, ~10 m amsl), which is relatively central in
455 the western Mediterranean basin. The Mobile Aerosol Station (MAS) of the LSCE (Laboratoire des Sciences
456 du Climat et de l'Environnement) laboratory was equipped with the new Raman lidar WALI (Chazette et al.,
457 2014a, 2014b), an AERONET/PHOTONS sun-photometer, and a set of in-situ instruments. A 5-wavelength
458 Solar Light Microtops-II manual sun-photometer was also used. The WALI instrument, its calibration and the
459 associated errors are documented in Chazette et al. (2014a). During all the experiment, the acquisition was

460 performed continuously with a vertical resolution of 15 m. AOD at the lidar wavelength of 355 nm has been
461 extrapolated from that measured by sun-photometer at 380 nm and 440 nm using the Angström exponent
462 (Chazette et al., 2015).

463 The in-situ instruments installed on-board the MAS included a 3-wavelength TSI nephelometer, a Magee
464 Scientific Model AE31 7-wavelength aethalometer, a TEOM microbalance, and a Vaisala meteorological
465 probe type PTU300. The nephelometer was sampling through a PM₁₀ inlet to measure the aerosol scattering
466 coefficient at 3 wavelengths (450, 550 and 700 nm) with an integrating time step of 5-min. The
467 aethalometer was sampling through a PM_{2.5} inlet to measure aerosol absorption (at 7 wavelengths) and
468 derive a 5-min average black carbon concentration. The TEOM measured dry PM₁₀ concentration every 30
469 min. In addition two optical particle counters (OPCs) were installed outdoors next to the sun-photometer on
470 a mobile platform. A MetOne HHPC-6 and a LOAC (Renard et al., 2015a, 2015b) respectively measured
471 aerosol particle number concentration in 6 channels above 0.3µm in diameter and in 19 channels above 0.2
472 µm. The LOAC instrument accuracy is discussed in detail by Renard et al. (2015a, 2015b).

473 **2.2.4 Granada station**

474 The station of the Atmospheric Physics Group (GFAT) is located in the Andalusian Institute for Earth System
475 Research (IISTA-CEAMA), in Granada, Spain (37.16°N, 3.61°W, 680 m amsl). The station is at a relatively
476 short distance, about 200 km away, from the African continent and approximately 50 km away from the
477 western Mediterranean Sea. During the SOP-1a campaign, lidar measurements were performed
478 simultaneously with a multiwavelength Raman lidar and a scanning Raman lidar both from Raymetrics S.A.
479 The multi-wavelength Raman system is part of the EARLINET network. In addition, a ceilometer was
480 operated. Column integrated characterization of the atmospheric aerosol was performed following
481 AERONET protocols with two Cimel sun-photometers deployed at two different heights: Granada (680
482 m asl) and Cerro Poyos (37°6'32"N, 03°29'14"W, 1790 m asl) stations. In addition, in-situ instrumentation
483 was continuously operated providing measurements of aerosol light-absorption coefficient at multiple
484 wavelengths (multi-angle absorption photometer (MAAP) from Thermo ESM Andersen Instruments and
485 Aethalometer model AE31), size distribution and particle number concentration for diameters larger than
486 0.5 µm (TSI aerodynamic particle sizer APS model 3321) and light-scattering and backscattering coefficient

487 at dry and at relative humidity of 85% by means of a TSI tandem nephelometer humidograph system.
488 Furthermore, the chemical composition in the PM₁ and PM₁₀ size fractions was determined during 16 and
489 17 June by collecting aerosol samples using two high-volume samplers (Alados-Arboledas et al., in prep.).

490 **2.2.5 Capo Granitola station**

491 Several instruments were also deployed at Capo Granitola (37°34'N, 12°40'E), a site along the Southern
492 coast of Sicily. The site, within a combined effort of ENEA, Univ. of Florence, and Univ. of Valencia, was
493 equipped with a PM₁₀ sampler, a MultiFilter Rotating Shadowband Radiometer (MFRSR) to derive spectral
494 AOD, and radiometers and spectrometers for the measurement of global, direct, and diffuse radiation
495 throughout the SW and LW spectral ranges.

496 **2.3 Surface remote-sensing network**

497 Two surface remote-sensing networks were operated during the ChArMEx SOP-1a experiment, namely the
498 AERONET/PHOTONS and EARLINET/ACTRIS (Pappalardo et al., 2014) networks. These networks were highly
499 useful as they allow estimating the column-integrated aerosol loading as well as the vertical structure of
500 particles.

501 **2.3.1 The AERONET/PHOTONS Sun-Photometer Network**

502 AERONET (Aerosol Robotic Network; <http://aeronet.gsfc.nasa.gov/>) is a federated network of ground-based
503 sun-photometers and the associated data inversion and archive system, that routinely performs direct sun
504 observations about every 15 min during daytime, and both almucantar and principal plane sky radiance
505 measurements, at selected solar angles (Holben et al., 1998). Along with AOD observations, the AERONET
506 aerosol retrieval algorithm (Dubovik and King, 2000) delivers the complete set of column-effective aerosol
507 microphysical parameters, including volume size distribution, refractive index at several wavelengths and
508 fraction of spherical particles (Dubovik et al., 2006). In addition, using these microphysical parameters, the
509 algorithm provides other column-effective aerosol optical properties such as wavelength dependent SSA,
510 phase function, and asymmetry parameter, as well as integral parameters of bi-modal particle size
511 distributions (concentration, mode radii and variances) (Dubovik et al., 2002). The accuracy of AERONET
512 retrievals is evaluated and discussed by Dubovik et al. (2000, 2002). In addition to microphysical and optical
513 aerosol properties, we also have used direct radiative forcing calculations operationally provided at any

514 AERONET location as an operational product of the network. The method of derivation is described in detail
515 by Garcia et al. (2012). Briefly, the broadband fluxes were calculated using the radiative transfer model
516 GAME (Dubuisson et al., 2004; Roger et al., 2006) that has been integrated into operational AERONET
517 inversion code. Sun-photometer stations used during the SOP-1a campaign over the Western basin are
518 listed in the Table 2. The new instruments deployed specifically during the ChArMEx/ADRIMED project are
519 the Ersa, Cap d'En Font, Cagliari and Majorque stations.

520 **2.3.2 The EARLINET/ACTRIS network**

521 Between 22 and 24 of June, four ACTRIS/EARLINET lidar stations (in addition to the EARLINET sites of
522 Barcelona and Granada), were operated (Sicard et al., 2015a; Barragan et al., in prep.):

- 523 • Naples: backscatter (355 and 532 nm) and depolarization ratio (532 nm) profiles (22 June),
- 524 • Serra La Nave (Sicily): backscatter (355 nm) and depolarization ratio (355 nm) profiles (22 June),
- 525 • Potenza: extinction profiles (355 and 532 nm), backscatter (1064 nm) and depolarization ratio (532
526 nm) profiles (22 and 23 June),
- 527 • Lecce: extinction (355 and 532 nm), backscatter (1064 nm), water vapour and depolarization ratio
528 (355 nm) profiles (22 and 24 June),

529 **3. Overview of the aircraft and balloon operations**

530 **3.1 Overview of the ATR-42 and F-20 flights**

531 Figure 3 summarizes ATR-42 and F-20 flights trajectories performed during the experiment and their main
532 characteristics. Most of the western Mediterranean basin has been investigated during the campaign by
533 both aircrafts, excluding areas under the control of African aviation authorities where authorizations for
534 scientific operations are very difficult to obtain. The first period of the campaign (16 to 20 June) was mainly
535 dedicated to ATR-42 flights over Spain and Minorca islands (16-17 June, flights 29-32) and Southern France-
536 Corsica Island (19-20 June, flights 33-34). During the second period (21-28th of June) of the SOP-1a, ATR-42
537 flights have been mostly conducted over the Sardinia-Sicily-Lampedusa region in the central Mediterranean
538 (flights 35-40). In July, two ATR-42 flights (41 and 42) were conducted over Lampedusa on 02-03 July and
539 two others (43 and 44) on 04 July over the Gulf of Genoa. It should be noted that most ATR-42 flights
540 included some transects at fixed altitudes (generally ~30 min of duration) associated with vertical profiles

541 over surface super-sites and secondary stations. Details about each flight track are available on the
542 ChArMEx Operation Centre website (ChOC; <http://choc.seedoo.fr>). On Figure 3, F-20 flights trajectories are
543 also indicated with the day corresponding to each flight. Except for the 16 and 17 June when F-20 is not
544 flying, most of flights have been made jointly between the two aircraft. The longer flight range of the F-20
545 allowed us to document the Tyrrhenian Sea (not covered by the ATR-42) and to perform vertical profiles of
546 aerosols over Southern Italy in association with EARLINET/ACTRIS lidar observations. It should be finally
547 noted the additional F-20 flight between Sardinia and Spain on 27 June specifically dedicated to sample a
548 forest fire plume transported long-range from North America.

549 **3.2 In-situ and remote sensing observations on board the ATR-42**

550 The instrumentation deployed onboard the ATR-42, described in detail in Denjean et al. (2015) and Nicolas
551 et al. (in prep.) is summarized in Table 3. It is analogous to the one used for the two super-sites and was
552 devoted to the characterization of microphysical, chemical and optical properties of aerosols that have been
553 advected above the MBL and so not detectable at the surface. As indicated in Table 3, the number size
554 distribution of aerosols, including fine and coarse fractions, as well as the total concentration of particles
555 have been evaluated using SMPS, GRIMM, FSSP and UHSAS systems. The corresponding size ranges for all
556 instruments are indicated in Table 3. A $3\text{-}\lambda$ nephelometer and $1\text{-}\lambda$ Cavity Attenuated Phase Shift (CAPS
557 PMex) particle light extinction monitor system (Petzold et al., 2013) have been used conjointly for
558 estimating scattering and extinction properties of particles. The CAPS-PMex system, used for the first time
559 onboard the ATR-42, provides an additional constrain on the aerosol optical properties, useful to determine
560 the absorbing properties. Indeed, the aerosol absorbing characterization remains largely challenging using
561 filter techniques (Moosmüller et al., 2009). These optical inter-comparisons have been performed for
562 different aerosol plumes and are presented in Denjean et al. (2015).

563 In addition, passive remote-sensing observations have been conducted during the SOP-1a experiment using
564 the PLASMA (Photomètre Léger Aéroporté pour la Surveillance des Masses d'Air) system, which is an
565 airborne sun-tracking photometer with two main characteristics: lightness and a wide spectral coverage (15
566 channels between $0.34\text{--}2.25\ \mu\text{m}$; see Karol et al., 2013). The instrument contains also a microprocessor
567 which derives the Sun position depending on time, latitude, longitude (provided by a GPS system) and the

568 rotation of the airborne (provided by a gyroscope). Spectral AOD is derived from these direct sun
569 measurements and the calibration coefficients. During the campaign, several AOD comparisons were done
570 between PLASMA and AERONET/PHOTONS sun-photometers (Cagliari, Lampedusa, Granada) showing
571 differences within 0.01 at all wavelengths. Moreover, as a consequence of performing AOD measurements
572 at different heights, the aerosol extinction vertical profiles have been also obtained during every
573 landing/taking off and during pre-scheduled vertical profiles (Torres et al., this special issue). Finally, upward
574 and downward radiative fluxes (SW & LW) have been measured onboard the ATR-42 by means of CMP22
575 and CGR4 radiometers calibrated before the campaign.

576 **3.3 Remote-sensing observations on board the F-20**

577 **3.3.1 LNG observations**

578 The LEANDRE Nouvelle Generation (LNG) was used in its backscatter configuration during the ChArMEx-
579 ADRIMED field operation onboard the SAFIRE F-20 aircraft. In the present campaign, the LNG system
580 involved three elastic channels at 1064, 532 and 355 nm. Depolarization was also measured in a fourth
581 channel operating at 355 nm. The profiles of atmospheric particulate extinction and backscatter coefficients
582 are then retrieved. Zenith pointing lidar measurements were taken before most of the flights from the
583 ground at the Cagliari airport (39.25 N, 9.06 E) in Italy. Lidar observations allow the detection of biomass
584 burning plumes (BBP) (see part 4.3) arriving at the Cagliari airport on 28 June as described by Ancellet et al.
585 (submitted).

586 **3.3.2 OSIRIS observations**

587 OSIRIS (Observing System Including Polarisation in the Solar Infrared Spectrum) is an instrument devoted to
588 observation of the polarization and directionality of the solar radiation reflected by the surface-atmosphere
589 system. OSIRIS is based on the same imaging radiometer concept as the POLDER instrument (Deschamps et
590 al, 1994). It includes two optical systems: one for the visible and near infrared range (VIS-NIR, from 440 to
591 940 nm) and the other for the shortwave infrared (SWIR, from 940 to 2200 nm). OSIRIS has eight spectral
592 bands in the VIS-NIR and six in the SWIR. During the SOP-1a campaign, OSIRIS was flown aboard the French
593 F-20 aircraft and looked at nadir. The quantities used to derive the aerosol and cloud properties from OSIRIS
594 are the normalized total and polarized (unitless) radiances. The aerosol algorithm used for OSIRIS over

595 ocean is an optimal estimation method (OEM), similar to the one described in Waquet et al. (2013). For
596 ocean targets, we use all the available angular and polarized information acquired in three spectral bands
597 (490, 670 and 865 nm) to derive the aerosol parameters and some properties of the surface. A combination
598 of two log normal size distribution functions is assumed (i.e. a fine mode and a coarse mode) as well as a
599 mixture of spherical and non-spherical particles (Dubovik et al., 2006). The main retrieved parameters are
600 the aerosol AOD, SSA, the fraction of spherical particles within the coarse mode and the complex refractive
601 index.

602 **3.4 Balloons operations**

603 Instrumented balloons were launched by the French Space Agency (CNES) from the airfield of Sant Lluís
604 (39°51'55"N, 04°15'15", 55 m asl) on Minorca Island, less than 6 km NE of the Cap d'en Font station
605 described above. Two types of balloons were launched to document dust transport events: (i) ascending
606 dilatable rubber balloons, and (ii) quasi-Lagrangian spherical pressurized drifting balloons, called BPCL
607 (Ballon Pressurisé de Couche Limite, or boundary-layer pressurized balloons).

608 A total of 15 sounding balloons were launched during the campaign between 12 June and 02 July (Table 4)
609 and most balloons reached more than 30 km in altitude. Except for the first test balloon on June 12, the
610 payload of sounding balloons included a pair of meteorological sondes with temperature, humidity and GPS
611 sensors allowing the retrieval of the position (± 10 m), derived pressure (± 1 hPa) and wind (± 0.15 m s⁻¹),
612 respectively coupled, for certain flights (see Tables 4 and 5), to an ozone electrochemical sonde (Gheusi et
613 al., in prep.) and a LOAC OPC (Renard et al., 2015a, 2015b). Balloon trajectories were confined within the
614 area 39-41.2°N in latitude and 3-5°E in longitude.

615 BPCLs are designed to drift and make observations with a payload of a few kg in the lower troposphere for
616 durations of up to several weeks (Vialard et al., 2009). Two versions were used, the standard one of 2.5 m in
617 diameter, launched pressurized, which is limited to a maximum float altitude of about 2.5 km (Ducrocq et
618 al., 2014), and one developed for ChArMEx of 2.6 m in diameter, launched unpressurized to reach a float
619 altitude of more than 3 km in altitude. The payload was composed of a GPS system, PTU instruments on the
620 upper pole of the balloon, a LOAC instrument on the lower pole of the balloon and two solar radiation
621 sensors for upward and downward solar flux measurements. In addition a BPCL equipped with a modified

622 ozone electrochemical sonde (Gheusi et al., in prep.) instead of a LOAC was launched in parallel of a LOAC
623 balloon on 4 occasions on 16 and 17 June (BPCL B53 and B54, respectively), and on 02 July (BPCL B55 and
624 B57). 14 BPCL balloons were launched in total between 16 June and 02 July 2013 (Table 5). Trajectories are
625 plotted in Figure 4 with a visualization of daytime vs. night-time conditions. The longest flight in terms of
626 distance (1053 km) and time duration (32.6 h) was the ozone BPCL B57, which passed the Sicily strait and
627 reached the southern limit of the authorized flight domain south-south-west of Malta. Communication
628 failure occurred with the two balloons B53 and B70. Flights were automatically terminated by drilling the
629 envelope at a distance of 30 km from southeastern French coasts, western Sicily coast, or North Tunisian
630 coast. BPCL float altitudes ranged between about 1850 and 3350 m amsl (balloon B54 with an ozone sonde
631 and B71 with a LOAC, respectively). Pairs of balloons with LOAC measurements were launched at different
632 float altitudes to document Saharan dust transport on June 16 (2100 and ~3100 m amsl) and June 19 (2550
633 and ~3500 m amsl).

634 **4. Overview of Meteorological Conditions**

635 **4.1 Synoptic Situation**

636 As mentioned below, the SOP-1a experiment was mostly characterized by moderate aerosol loading mainly
637 controlled by the contribution of mineral dust particles. This situation is well observed through the AOD
638 derived by MODIS (Tanré et al., 1997), MISR (Kahn et al., 2010), PARASOL (Tanré et al., 2011) or SEVERI
639 (Thieuleux et al., 2005) sensors and averaged for the June-July 2013 period (Figure 5), which show an
640 average AOD ranging between 0.2 and 0.4 (at 550 nm) over the western and central Mediterranean basins.
641 During the SOP-1a, distinct meteorological conditions have led to the transport of mineral dust over the
642 basin as shown in the Figures 5 and 6. Figure 7 shows the dust mass concentration together with the
643 geopotential and wind at 700 hPa for the 16 June, 19 June, 22 June, 29 June and 02 July. In the following
644 sections, we discuss the meteorological conditions (surface wind, sea level pressure, 700 hPa geopotential
645 and wind direction) for these different days in order to understand the transport of mineral dust aerosols
646 over the Mediterranean.

647 Wind direction and intensity vertical profiles as simulated by the ALADIN regional model (outputs every 3
648 hours) as a function of time, for the 11 June to 06 July period and for the whole SOP-1a period at three

649 different sites: Ersa, Minorca and Lampedusa islands are shown in Figure 8. At the beginning of the SOP-1a,
650 the northwestern Mediterranean area was under the influence of a large pressure ridge at 700 hPa,
651 generating a westerly to south-westerly flow over Spain and southern France. Over Minorca, the near
652 surface (1000 - 850 hPa) winds were generally from the easterly to north-easterly direction (indicated by the
653 blue color in the Figure 8) while the wind direction estimated between 700 and 500 hPa was clearly from
654 the south, southwest direction (brown color), which is a favourable condition for the transport of mineral
655 dust above South-Spain and then Balearic islands (Figure 6). This point is well observed in figure 7, showing
656 the geopotential at 700 hPa for the 16th of June. The general circulation at 700 hPa during this dust event
657 indicates a reinforcement of the southwesterly winds in southern Spain advecting air masses with large
658 concentrations of dust aerosols as shown by SEVIRI AOD (AOD of 0.4-0.5) for that day (Figure 6). A low
659 pressure system moved from the British Isles towards the Gulf of Biscay and then the Iberian Peninsula
660 between the 17th and 20th June, leading to veering winds that became southerly over the northwestern
661 Mediterranean. Thus in Minorca, the direction of the wind changed from easterly to southerly direction
662 between 1000 and 850 hPa. A more pronounced southerly-southwesterly flow was also observed at 700
663 hPa in Minorca (19th-21st of June) as shown by the geopotential at 700 hPa. This circulation characterized by
664 the presence of the low geopotential over the Gulf of Biscay induced a strong southerly flow at 700 hPa
665 between the Balearic and Corsica islands associated with large dust optical depth concentrated in this zone
666 as shown by SEVIRI AOD (AOD of 0.3-0.4) for 19th June (Figure 6). This period of the SOP-1a corresponds to
667 the two ATR-42 flights 33 and 34 (Figure 3). After 20th June, this low pressure system moved eastward,
668 generating a trough located between France and Italy, and inducing a waving westerly flow over the north-
669 western Mediterranean. As a result, the aerosol loading over the western basin decreased between 21st and
670 24th June, but the westerly (resp. northerly) winds observed at 700 hPa in Minorca (resp. Ersa) (Figure 8)
671 reinforced the transport of dust aerosols over the central basin and the Lampedusa station (where winds
672 were from the north westerly direction at 3 km height). These meteorological conditions lead to an increase
673 of the dust optical depth over the central Mediterranean as shown by the SEVERI instrument and
674 AERONET/PHOTONS data. Between 25th and 29th June, a northwesterly flow set up between the Gulf of
675 Lions and Sicily. The vertical profiles of the wind direction reveal a remarkable transition on 29th June with

676 significant changes in direction from westerlies to north, north-westerlies, notably over the Minorca and
677 Ersa stations above 850 hPa. The 700 hPa geopotential field on 29 June at 1200 UTC from the ALADIN
678 atmospheric model analysis shows a maximum over the Atlantic Ocean whereas a deep low pressure
679 system was located over southern Algeria. This strong geopotential gradient lead to intense northerly to
680 north-westerly winds at 700 hPa over the western basin leading to significant AOD over Libya (AOD of 0.4-
681 0.5) and the Alboran sea (AOD of 0.5-0.6) as shown in Figure 6. These meteorological conditions lead to low
682 dust optical thickness over the central Mediterranean as observed by AERONET/PHOTONS data. Finally,
683 during the last period of the SOP-1a experiment, (30 June - 05 July), weather conditions became more
684 anticyclonic over the region while low systems were confined to northern Europe. Figure 8 shows north-
685 westerly winds in the whole troposphere in Lampedusa and Minorca, limiting the presence of dust aerosols
686 to the southern part of the north-western Mediterranean.

687 **4.2 Surface temperature, cloud cover and precipitation**

688 In terms of surface temperature, which is one of the most important meteorological variables that control
689 biogenic or biomass burning aerosol emissions over the Euro-Mediterranean region, the summer 2013 was
690 mostly characterized by moderate values as shown in Figure 9. Indeed, during the SOP-1a period, surface
691 temperatures (in °C and at 12:00 UTC) derived from NCEP reanalysis (Kalnay et al., 1996) for different days
692 reveal moderate values especially over the western Mediterranean region (South-West France and Spain).
693 One can observe temperatures of about 15-20°C (at 12:00 UTC) over Spain and Portugal, which are one of
694 the main regions of the Mediterranean where large fire events occur. In addition, part of France was also
695 characterized by moderate surface temperature but slightly higher than over Spain especially over
696 northeastern regions. A strong west to east gradient is observed over Europe with strongest values over the
697 eastern regions (around 30°C over Greece and the Balkans) compared to the western basin. A similar
698 conclusion is obtained over the Mediterranean Sea with differences of about 5°C between the eastern
699 (around 25°C for the SOP-1a period) and the western (around 20°C) basin. Among other factors (such as
700 cloud fraction and shortwave radiations), such moderate surface temperatures do not create favourable
701 meteorological conditions to produce intense Mediterranean biomass burning events and/or significant
702 production of secondary organic and inorganic aerosols. Concerning smoke aerosols, GAFS-V1 emission

703 data, analysed for the SOP-1a period, do not reveal important primary BC and OC fluxes emissions (not
704 shown). This is consistent with the APIFLAME biomass burning emission estimates (Turquety et al., 2014)
705 data as reported by Menut et al. (2015).

706 During the SOP-1a, the cloud cover retrieved over the Euro-Mediterranean region (excluding the
707 Mediterranean Sea) from CRU (Climate Research Unit) data (Harris et al., 2013) (Figure 10) indicates the
708 largest values (between 75 and 95%) over France, Benelux and Eastern Europe regions. In parallel, southern
709 France, as well as western Spain and the Balkans are characterized by moderate cloud cover with values
710 around 50-60 % for June 2013. Over the Mediterranean coast, the cloud cover strongly decreases for most
711 of countries, with values lower than 40 %. Such spatial cloud cover (observed during the SOP-1a) over the
712 Euro-Mediterranean could limit the photochemical processes over the main anthropogenic sources (such as
713 the Benelux and Po Valley) and the associated production of secondary aerosols. This could explain for a
714 part the low to moderate contribution of fine anthropogenic particles to the total atmospheric loading
715 during the SOP-1a. In parallel, the mean precipitation (averaged for June 2013), obtained from the TRMM
716 (Tropical Rainfall Measuring Mission) instrument over land and sea (CRU observations are only available
717 over land, see Figure 10), are found to be very heterogeneous over the Euro-Mediterranean continental
718 region, with some important values over the Balkans, Alps and eastern Europe (from 100 to 250 mm for the
719 month of June 2013) and moderate values over Italy, Croatia, western France and Benelux (80 to 100 mm,
720 as shown in the Figure 11). Over the Mediterranean Sea, southern Spain and northern Africa, the
721 precipitation was smaller, with most of values lower than 20 mm during the SOP-1a.

722 To summarize, this global view of the synoptic situation, cloud cover and regional precipitation patterns
723 indicate that the meteorological conditions during the experimental campaign were favourable to moderate
724 mineral dust emissions, associated with a weak contribution of anthropogenic aerosols over the western
725 basin. This important characteristic of the SOP-1a is well observed in Figure 12, which indicates the AOD
726 anomalies (calculated for the period 2000-2013) of summer 2013 compared to all AOD summer derived
727 from MODIS and MISR data. Indeed, negative AOD anomalies of about -0.05 are found over the western
728 Mediterranean basin for the summer 2013, both from MODIS and MISR observations. To conclude, it
729 appears that the period of observations during the SOP-1a was characterized by aerosol concentration

730 slightly lower but in the same range of magnitude that usually observed during summer over the western
731 Mediterranean. The level of aerosol concentration was found to be moderate but allows investigating
732 several dust and sea-spray events as well as an interesting intense biomass burning plume advected from
733 North America.

734 **4.3 An aged smoke plume advected over Europe**

735 During the SOP-1a, several large forest fires occurred in North America (Colorado, Alaska, Canada) from
736 June 17th to 24th, 2013, as identified by the MODIS instrument. Absorbing aerosol index produced from
737 GOME-2 by KNMI (<http://www.temis.nl/aviation/aai-pmd-gome2b.php?year=2013>) shows that a large
738 smoke plume crossed the north Atlantic and reached Western Europe coasts on June 25. Main fire areas,
739 with fire radiative power higher than 50 MW (Shroeder et al., 2010), have been detected over Canada
740 (Ancellet et al., submitted). Average MODIS AOD during the same period (23 to 28 June 2013) indicate
741 values as high as 1 over the Atlantic Ocean, suggesting that a significant fraction of the aerosol produced by
742 the fires was transported to Western Europe during the ChArMEx/ADRIMED field campaign. To investigate if
743 the western Mediterranean has been impacted by these fires, a forward simulation of the Lagrangian plume
744 dispersion model FLEXPART (Ancellet et al., submitted) has been conducted to quantify the spatial extent of
745 the fire plume transport for 11 days. Fires emissions areas were identified by MODIS observations over
746 several locations in Canada and Colorado. The aerosol mass is emitted in the transport model from June
747 17th to 28th in a 3 km layer as suggested by the CALIOP lidar observations over Canada. The biomass
748 burning plume reaches much lower latitudes over Europe, down to the Western Mediterranean 4-10 days
749 after the emission in Canada. During the SOP-1a, the plume was mainly present in the altitude range of 2.5 -
750 4.5 km and has been sampled by many remote sensing and in-situ instruments on June 27th and 28th; at
751 Minorca and Cagliari surface stations, and between Sardinia and Lampedusa onboard the ATR-42 aircraft.

752 **5. Overview of aerosol physical-chemical-optical properties, vertical profiles and local direct** 753 **radiative forcing**

754 **5.1 Aerosol physical and chemical properties**

755 **5.1.1 Aerosol mass and number concentration at the two super-sites**

756 First, PM concentrations between the two different stations are reported in the Figure 13, which reports the

757 daily time-series of PM1 and PM10 at Ersa, as well as PM10 and PM40 at Lampedusa. The results indicate a
758 significantly higher mass concentration at Lampedusa compared to Ersa. Indeed, the mass concentration
759 observed at Lampedusa is comprised between 10 and 30 $\mu\text{g m}^{-3}$, with a mean of 21 $\mu\text{g m}^{-3}$, which is two
760 times higher than the averaged PM10 ($\sim 9 \mu\text{g m}^{-3}$) measured at Ersa. One can note the significant peak of
761 PM40 (maxima of 75 $\mu\text{g m}^{-3}$) at Lampedusa during the 24 to 26 June period that corresponds to a significant
762 production of primary marine aerosols. Finally, the PM1 concentration at Ersa is found to be almost
763 constant during the period of the campaign, with a mean value of 6 $\mu\text{g m}^{-3}$. In order to take into account the
764 difference of altitudes between the two sites of Lampedusa and Ersa, we have applied a correction factor to
765 PM10 observed at Ersa (530 m) for estimating a new PM10 concentration corresponding to the altitude of
766 Lampedusa. In that sense, we have applied the logarithmic law reported by Piazzola et al. (2015) using a
767 value of 0.75 for the factor s to correct the mass concentration of sea spray aerosols only. The calculated
768 mean value of PM10 is about 12 $\mu\text{g m}^{-3}$ (Figure 13), closer to the mean value observed at Lampedusa (21 μg
769 m^{-3}). In addition, the background aerosol number concentrations (for $D_p > 0.01 \mu\text{m}$) observed within the
770 boundary layer in Corsica averaged $\sim 2000 \text{ cm}^{-3}$ (not shown). The lowest concentrations ($\sim 200 \text{ cm}^{-3}$) resulted
771 from aerosol activation to cloud droplets, and scavenging from cloud droplets and rain drops, while high
772 concentrations as high as 10000 cm^{-3} were observed during pollution events from continental European air
773 masses. The number concentrations showed a diurnal cycle suggesting that the site was situated within the
774 marine boundary layer during daytime and within the free troposphere during night-time. The analysis of
775 the diurnal variation of the particle number size distribution is further indicating that nucleation events also
776 increased the particle number concentration during daytime, about one third of the time (Sellegrì et al., in
777 prep.). The periods of high aerosol number concentrations detected between the 12th and 25nd of June were
778 also dominated by a single mode with diameters between 30 and 150 nm. The small Aitken mode ($d_g < 50$
779 nm) associated with pollution events suggests a relatively fresh aerosol that has been formed during
780 transport from the European continent. The largest mode ($d_g \sim 150 \text{ nm}$) occurred during the dust event on
781 18 June.

782 **5.1.2 Columnar particle volume size distribution**

783 We have used the column-integrated particle size volume distributions derived from AERONET/PHOTONS

784 sky radiance measurements (Dubovik et al., 2000). These size distributions allow investigating the changes
785 in aerosol size distribution between different stations during the SOP-1a and over the western basin. Four
786 different stations have been studied, which include the two super-sites of Lampedusa and Ersa, as well as
787 the aircraft and balloon base stations; Cagliari and Cap d'En Font, respectively. Daily volume size
788 distributions for both sites are represented in the Figure 14, as well as the averaged (red curve) size
789 distribution for the whole period (1 June to 5 July) and the number of observations. In addition, the mean
790 values of the volume radius, concentration of fine and coarse mode and the standard deviations of the
791 volume size distribution are reported in the Table 6. It should be noted that the scales of the y-axis are
792 different for each figure. One can note the bimodal size distribution for both stations with large spread of
793 radius values, especially for the coarse mode. The most important concentrations are obviously observed in
794 Lampedusa, near the mineral dust sources, with maxima of $\sim 0.12 \mu\text{m}^3 \mu\text{m}^{-2}$ for the coarse mode. In parallel,
795 the lowest concentrations are observed at the Ersa station due to the absence of intense polluted-
796 photochemical or smoke aerosol events over southern France and Italy during the SOP-1a. In that sense, the
797 mean contribution (red curve) of the coarse mode to the aerosol volume size distribution appears to be
798 predominant at most sites, except at the Ersa station. However, the inclusion of the corrected factor
799 (Piazzola et al., 2015) for taking into account the altitude of the Ersa site reduces slightly the differences in
800 the concentration of the coarse mode with the Lampedusa station (see Table 6). This point is well noted for
801 the Cap d'En Font station, where the concentration of each modes appear as equivalent, due to the absence
802 of pollution from the Iberian Peninsula during the period of observations. For this site, it is interesting to
803 note the intense peak of concentration ($0.08 \mu\text{m}^3 \mu\text{m}^{-2}$) for the 27th June, which is due to the transport of an
804 important smoke plume over the Mediterranean (see Ancellet et al., submitted; and Chazette et al.,
805 submitted). Finally, the contribution of the coarse mode clearly increases for the two other, more southern
806 Italian sites of Cagliari and Lampedusa, which are more affected by the mineral dust compared to Ersa and
807 Cap d'En Font. The variability of AERONET products collected over a period of four years at Ersa and Palma
808 de Mallorca, near Cap d'En Font, is reported in Sicard et al. (2015b, this special issue). It is interesting to
809 note the variability (± 0.05) in the derived size of the coarse mode at Lampedusa (see Table 6), which will be
810 analysed in regards to dust sources in a future study. The derived volume concentrations over these two

811 stations highlight the moderate dust activity occurring during the SOP-1a experiment, when compared to
812 stations under high dust conditions. As an example of comparisons, Dubovik et al. (2002) reported a large
813 range of concentration for the coarse mode for dusty sites (such as Cape Verde or Solar Village), which are
814 characterized by larger concentrations, close to $0.30 \mu\text{m}^3 \mu\text{m}^{-2}$. In parallel, the Bahrain (Persian Gulf)
815 AERONET station is characterized by a concentration of $0.14\text{-}0.15 \mu\text{m}^3 \mu\text{m}^{-2}$.

816 **5.1.3 Particle size distribution during transport**

817 Figure 15 presents an example of the evolution of the aerosol particle number concentrations in the 19
818 particle size classes of the LOAC instrument as measured along the northward trajectory of the BPCL balloon
819 B74 from Minorca Island to the French coast (see Figure 4). The balloon was launched at 09:46 UTC on 16
820 June 2013 during a moderate desert dust event shown on top of Figure 6 (AERONET-derived AOD at 500 nm
821 of 0.15). It drifted at a constant altitude of ~ 2.1 km at the bottom of the African dust layer observed with
822 the WALI lidar at Minorca (not shown; see Chazette et al., 2015), and was automatically forced to land on
823 the sea before reaching the coast South of Marseille, after a 12-h flight of 368 km. The dominant mineral
824 dust nature of the particles was confirmed by the LOAC particle typology measurements (Renard et al.,
825 2015b). The figure illustrates that LOAC has detected large particles of up to $50 \mu\text{m}$ in diameter, although
826 the plume originated from North-Africa a few days before (Renard et al., 2015b). The concentrations of
827 particles remained relatively constant during the flight, suggesting either no significant sedimentation of the
828 largest particles during the flight or compensation by particles coming from above. The BPCL balloon B70
829 launched a few minutes later drifted at an upper altitude of ~ 3.1 km and followed a different trajectory
830 towards East (Figure 4) but showed a quite similar extended particle size range with larger concentrations in
831 almost all channels except the extremes (not shown). The 4 other drifting balloons launched in the dust
832 layer during this event on June 17 and 19 (Table 5) did confirm the presence of very large particles ($>20 \mu\text{m}$),
833 which cannot be reported by AERONET particle size distribution retrieval algorithm (Hashimoto et al., 2012).
834 In addition, observations of large particles ($>15 \mu\text{m}$) was systematically found during all other LOAC balloon
835 flights drifting in African dust layers, which will need further analysis to better understand the process that
836 can maintain such large particles in suspension during several days.

837 Concerning the aerosol microphysical properties, aircraft observations have allowed to investigate the

838 vertical structure of aerosol size distribution showing particles characterized by large size (>10 μm in
839 diameter) within dust plumes. In addition, in most of cases, a coarse mode of mineral dust particles,
840 characterized by an effective diameter $D_{\text{eff},c}$ ranged between 5 and 10 μm , has been detected within the dust
841 layer located above the MBL. Such values are found to be larger than those referenced in dust source region
842 during FENNEC, SAMUM1 and AMMA, as well as measurements in the Atlantic Ocean at Cape-Verde region
843 during SAMUM-2 and at Puerto-Rico during PRIDE. The complete analysis of aerosol size distribution is
844 detailed in Denjean et al. (2015).

845 **5.1.4 Aerosol chemical composition**

846 In terms of aerosol chemical properties, an example of averaged mass-size distributions for carbonaceous
847 (Elemental and Organic Carbon, EC and OC) species (mass size distribution of inorganic and mineral dust
848 aerosols are not shown) obtained at Ersa from a 12-stage cascade impactor (DEKATI system, see Table 1) is
849 reported in Figure 16. The aerosol chemical properties obtained from PILS instrument at Ersa are detailed in
850 Claeys et al. (2015). As mentioned in Table 1, the measurements were obtained by using a 2-day collection
851 period in order to obtain a sufficient aerosol mass on filters for chemical analyses. This system provides the
852 speciation of the mass size distribution, including fine and coarse fractions. Such information is very useful
853 to derive optical properties using Mie calculations (Mallet et al., 2011) for the main particle types (sulfates,
854 ammonium, nitrates, sea-spray, dust, black and organic carbon). This provides crucial information's on key
855 radiative properties which are classically used in regional climate models (mass extinction efficiencies, SSA
856 and asymmetry parameter). Furthermore, it allows one to assess the spectral dependence of radiative
857 properties, which cannot always be estimated from in-situ instrumentation.

858 Concerning OC (blue curves), observations clearly report a bi-modal mass size distribution with two
859 different peaks for the majority of cases. The first (almost constant) peak is found in the 0.4-0.5 μm size
860 range in diameter and more occasionally a second one occurs in the coarse fraction around 3 μm .
861 Compared to the few available data over the Western Mediterranean, these mass size distributions are
862 found to be different from those obtained over Southern France, especially for the accumulation mode.
863 Indeed, during the ESCOMPTE experiment in southern France, Mallet et al. (2003) also observed a bi-modal
864 size distribution for OC aerosols but with a finer accumulation mode observed in the 0.1-0.2 μm size range.

865 Differences between the two observations is likely due to the proximity of anthropogenic sources during the
866 ESCOMPTE experiment compared to the Ersa station, where the possible ageing of carbonaceous particles
867 could affect the size of aerosols. On the contrary, the coarse mode of OC appears in the same range of size,
868 around 3 μm , for both experiments. Compared to data obtained in the eastern Mediterranean basin, the OC
869 mass size distributions are in good agreement with those estimated by Sciare et al. (2003) in Crete during
870 the MINOS campaign, with two modes around 0.4 μm and 3 μm . The BC (green curves in Figure 16) mass
871 size distribution is also characterized by a bi-modal size distribution, with two modes well correlated with
872 the mass size distribution of OC, except for the 16-19 June period (dust episode), where the size of EC fine
873 mode is higher ($\sim 0.5\text{-}0.6 \mu\text{m}$) than OC aerosols, the EC coarse mode remaining similar at $\sim 3 \mu\text{m}$. This reveals
874 a possible external mixing of carbonaceous aerosols for this event.

875 It should be also noted that the EC concentrations observed at the Ersa station are logically (due at least to
876 the altitude of the station and the absence of intense pollution during the SOP-1a, see section 4) lower
877 ($0.39 \mu\text{g}\cdot\text{m}^{-3}$) than EC concentrations (PM_{2.1}) reported by Eleftheriadis et al. (2006) from the eastern
878 Mediterranean during the summer season ($0.6 \mu\text{g}\cdot\text{m}^{-3}$) in July 2000. The same ascertainment is obtained on
879 OC concentrations with higher values ($4.2 \mu\text{g}\cdot\text{m}^{-3}$) reported by Eleftheriadis et al. (2006) compared to
880 observations at Ersa ($1.5 \mu\text{g}\cdot\text{m}^{-3}$). Concerning the modes of the OC and EC particle mass size distributions,
881 the two identified modes detected in Ersa are consistent with those reported by Mallet et al. (2011) at the
882 Porquerolles coastal island (southeastern France), who also detected two (fine and coarse) different modes
883 of the mass size distributions for EC (0.3-0.4 μm and 4-6 μm) and OC (0.3 μm and 5-6 μm) aerosol particles.
884 In most cases, we observed at Ersa lower concentrations of EC particles for both modes compared to OC
885 aerosols. The mass of OC and BC observed during the SOP-1a, for both modes, are found to be equivalent
886 with those observed by Sciare et al. (2003) in Crete in summer 2001. They report mean values of 0.30 and
887 $0.15 \mu\text{g m}^{-3}$ for fine OC and BC, respectively. During the MINOS experiment, the mean concentrations for OC
888 and BC coarse modes were about 0.1 and $0.02\text{-}0.03 \mu\text{g m}^{-3}$, what is also consistent with the observations at
889 Ersa. Finally, the mass concentrations obtained for each mode at Ersa are logically lower than those
890 obtained during the ESCOMPTE experiment, located much closer to pollution sources. For example, EC and
891 OC fine mode concentrations were respectively between 0.8 and $2.8 \mu\text{g m}^{-3}$ and between 3.1 and $6.9 \mu\text{g m}^{-3}$

892 during ESCOMPTE (Mallet et al., 2003). In addition and as discussed in the parts 4.1 and 4.2, the
893 meteorological conditions (surface temperature, meteorological synoptic situations) observed during the
894 SOP-1a campaign were not favourable to produce large concentration of polluted or smoke aerosols,
895 compared to the ESCOMPTE campaign, where AOD as large as 0.3-0.5 (in the visible range) has been
896 observed due to important concentration of anthropogenic-polluted particles. It should be noted that, in
897 parallel to filter analyses, higher time resolved observations from the PILS systems have been deployed at
898 the two stations of Lampedusa and Erba (Claeys et al., in prep.) during the SOP-1a.

899 In parallel to filters chemical analysis, over 700,000 single particle mass spectra were generated by the A-
900 TOFMS instrument during the sampling period (not shown). A *K*-means algorithm ($K = 80$), as described in
901 detail by Healy et al. (2010) and Gross et al. (2010) was used to classify aerosol mass spectra into different
902 particle classes. More than 40 distinct ATOFMS particle classes were identified and subsequently grouped
903 into 8 general categories for clarity. Elemental carbon containing particles dominated the dataset (55% of
904 total spectra), followed by K-rich particles (30%) and sea-spray (7%). The remaining particle categories
905 include organic carbon (OC)-containing (3%), trimethylamine (TMA)-containing (3%), shipping (2%), Fe-
906 containing (0.5%) and Ca-containing (0.3%). EC particles dominated the first third of the sampling period,
907 decreased noticeably for approx. 6 days and then dominated the rest of the sampling period again. In
908 contrast, K-rich particle (associated with biomass burning and dust) numbers were high only for the latter
909 half of the campaign, with a peak on 27-28 June. The profiles of these two particle categories suggest
910 transport from regional sources. Sea-spray particle numbers were at their highest during the period where
911 EC particles were at their lowest, and were generally low when EC particle numbers were high. OC-
912 containing particles were present during the same period K-rich numbers peaked, suggesting an association
913 with the transport of biomass burning particles. TMA particles were present in low numbers throughout the
914 sampling period, suggesting a less regional source, independent of the air masses influencing EC and sea-
915 spray particle occurrence. The same can be said of Fe and Ca-containing particles, likely to be local dust,
916 while shipping particle numbers were slightly higher during the first half of the sampling period.

917 Finally and concerning the aerosol chemical properties, an interesting aspect of the observations deployed
918 during the SOP-1a concerns the rBC concentrations obtained from the SP2 instrument onboard the ATR-42.

919 Despite its importance, studies on rBC were until now limited to surface-based measurements in the
920 Mediterranean region. Measurements of vertical distribution of rBC concentrations provide crucial
921 information for assessing the rBC radiative effects in the region. Figure 17 shows the vertical distributions of
922 rBC mass concentrations measured by the SP2 in the five areas (Granda, Minorca, Lampedusa, South-France
923 and Ersa). For the different vertical soundings, rBC mass concentrations ranged between 20 and 690 ng m⁻³
924 close to the surface. The surface rBC concentrations were generally less than 200 ng m⁻³, typical for
925 continental and regional background sites in the western Mediterranean basin (Ripoll et al., 2015). The
926 lowest surface concentration of rBC (~ 20 ng m⁻³) were found in south-France over the open sea with
927 almost no local contribution of anthropogenic aerosols. Maxima surface concentrations (~ 690 ng m⁻³)
928 were recorded over Granada where frequently heavy traffic emissions are occurring. These observations
929 were obtained between 07:15 and 07:45 UTC when the convection was not fully developed, which probably
930 did not favour the vertical transport of local emissions over Granada. A prominent feature in vertical profiles
931 is the presence of significant concentrations of rBC up to 5-6 km altitude. Therefore the regional transport
932 of rBC particles was not only limited to the MBL but occurred also at higher altitude. In most of the
933 observed cases, the rBC vertical distribution in the free troposphere reveals a strongly stratified structure
934 characterized by either single isolated plumes or more uniform layers. It is worth noting the presence of rBC
935 layers above the MBL in the open sea that could be attributed to convective transport from distant sources.
936 Only in few observed cases, rBC mass concentration decreased monotonically with increasing altitude, most
937 likely due to vertical transport of air masses from surface to higher heights.

938 **5.2 Aerosol optical properties**

939 **5.2.1 In-situ optical properties at the surface**

940 Figure 17 reports the (daily mean) time-series of nephelometer observations obtained at the surface for the
941 Ersa and Lampedusa stations. Daily scattering coefficients (at the three nephelometer wavelengths of 450,
942 550 and 700 nm) are reported, as well as the scattering Angström exponent (AE) calculated between 450
943 and 700 nm. At 550 nm and at Ersa, the scattering coefficient presents a significant variability during the
944 SOP-1a with peaks of about 35-40 Mm⁻¹ during the dust event (19-20th June) transported over the Corsica
945 island, associated to low values (15 Mm⁻¹) for certain periods of time, as for 21-22 June. The mean

946 scattering coefficient (at 550 nm) is 24 Mm^{-1} . Such scattering coefficient values are comparable to
947 observations reported by Vaishya et al. (2012) at the Mace Head station for Atlantic marine air, with
948 scattering coefficient (at 550 nm) ranged between 10 and 25 Mm^{-1} during the summer period. In terms of
949 scattering spectral dependence, the calculated scattering AE is found to be almost constant, with $AE \sim 1.5-2$
950 and a mean value of 1.71 (indicating that scattering is mostly dominated by fine aerosols) during the SOP-
951 1a, except for the 23rd-24th of June. The lowest values ($AE \sim 0.3-0.5$) observed during this period are the
952 result of a large contribution of coarse sea-spray aerosols (Claeys et al., in prep.) due to moderate (5 m s^{-1})
953 westerly winds (see Figure 8) at the Ersa station, which is also observed from the filter chemical size-
954 resolved analyses and detected on the A-TOFMS and VHTDMA data. In parallel, we observe that the dust
955 event occurring in Ersa on 18-20 June is not correlated to low scattering AE, revealing a possible
956 contribution of fine dust particles only to scattering, result of a possible deposition of the coarse dust
957 fraction during transport. The AERONET-derived AE between 440 and 870 nm shows values <1 in the
958 afternoon of 19 June and early morning of June 20 suggesting that coarse dust is present in the column. At
959 Lampedusa, the daily scattering coefficient (at 550 nm and from PM40 inlet) is between 20 to 90 Mm^{-1}
960 (mean value of 50 Mm^{-1}), which is twice higher than at Ersa (Figure 17). The scattering AE was also highly
961 variable, with values ranging between 0.5 and 2.5 (mean value of 1.1). The range of variability of these
962 values is due to the observed switch from clean air masses strongly impacted by marine emissions to
963 polluted air masses of various ages, including very aged/processed air masses from Northern Europe. A
964 single intrusion of mineral dust at the site was recorded on June 9 as a result of a cyclone-type of transport
965 from Tunisia (Formenti et al., in prep.).

966 **5.2.2 Remote-sensing observations from the surface**

967 The optical properties obtained from sun-photometer observations for different AERONET/PHOTONS sites
968 are shown in Figure 18. The AERONET/PHOTONS stations have been chosen as located in a domain
969 encompassing most of the SOP-1a in-situ and remote sensing observations (Figure 3) and they are
970 characterized by different aerosol regimes (see Table 2). The total AOD, Absorbing Aerosol Optical Depth
971 (AAOD), AOD for the fine (AODf) and coarse (AODc) modes of the volume size distribution, are indicated (at
972 440 nm) for 11 AERONET/PHOTONS stations (Table 2). As mentioned previously, the AOD time-series reveal

973 moderate values, never reaching values as large as reported during the summer 2012 ChArMEx/TRAQA
974 SOP-0 experiment (Rea et al., 2015). During summer 2013, the AOD was generally comprised between 0.1
975 and 0.7 (at 440 nm) for most of the AERONET/PHOTONS sites. Over the western basin, the Granada,
976 Minorca and Barcelona sites display the largest values during the transport of dust aerosols as detected by
977 satellite remote-sensing observations (Figure 6) for the 16 to 20th of June. During this dust event, the
978 contribution of fine and coarse modes to the total extinction AOD is equivalent. Over the central basin,
979 Lampedusa data reveal various peaks. The largest AOD was measured on June 6 (about 0.84 at 440 nm) and
980 8 (about 0.63 at 440 nm). Other peaks occurred around June 22 and July 01-02, with corresponding AOD of
981 about 0.30-0.40 (at 440 nm), with again an equivalent contribution of each mode of the volume size
982 distribution to the AOD. On June 27-28, an AOD peak was also observed over most of the sites and
983 corresponded to the transport of an aged smoke plume from the Canadian continent. In this specific case,
984 AOD was comprised between 0.25 and 0.50 (at 440 nm). Contrarily to the dust events, the contribution of
985 the different modes to AOD was significantly different during this episode. Indeed, as shown in Figure 18,
986 AOD was mostly controlled by the fine mode of the volume size distribution. This specific biomass burning
987 case is more deeply analysed by Ancellet et al. (submitted) and Chazette et al. (submitted).

988 We have also used the SSA dataset for making comparisons of its optical parameters between different
989 stations. As for the size distributions, we have analysed dataset in four stations, which are Ersa, Lampedusa,
990 Cap d'En Font and Cagliari, which represents, respectively, three of the different surface stations affected by
991 different aerosol regimes and the aircrafts locations (Cagliari). All (daily) SSA retrievals, associated with the
992 mean values (at the four wavelengths), are included in the Figure 19. Due to the moderate AOD over the
993 period, we used Level 1.5 AERONET/PHOTONS products. In that sense, it should be reminded that
994 uncertainties associated to SSA retrievals are important, about ± 0.07 as reported by Dubovik et al. (2000).
995 The results indicate an important variability of SSA and its spectral dependence over the different stations.
996 At 440 nm, the mean SSA is comprised between 0.91 and 0.98, with the lowest (resp. highest) value
997 observed in Lampedusa (resp. Ersa). Hence, aerosols appear as mainly scattering at Ersa and moderately
998 absorbing at Lampedusa. The contribution of the coarse mode to the total size distribution could explain
999 the lower values observed in Lampedusa at this wavelength. Indeed, the radiative effects and optical

1000 properties of dust are strongly dependent on the coarse mode size distribution as the larger particles
1001 appreciably decrease the SSA (McConnell et al., 2010; Otto et al., 2009). More recently and during the
1002 FENNEC experiment, Ryder et al. (2013) have calculated SSA (at 550 nm) for dust aerosols using the full
1003 range of sizes measured, indicating that dust SSA was highly sensitive to effective diameter: size
1004 distributions with the largest effective diameters produced the lowest SSA values. The presence of a coarse
1005 mode could also be due to the presence of marine aerosols within the MBL in Lampedusa. Observations for
1006 the Cap d'En Font and Cagliari stations reveal an intermediate value (0.93 at 440 nm) in Cagliari, which is
1007 also more affected by mineral dust aerosols (Figure 14). We can also observe very low values in Cagliari (for
1008 the period of 14 to 17 June) that could be due to local pollution. Anyway, it should be remained that those
1009 retrievals have been performed under low AOD (~ 0.10 at 440 nm) conditions and are associated to large
1010 uncertainties. One important point concerns the changes in the SSA spectral signature between Ersa
1011 (negative tendency between 440 nm to 1020 nm) and Lampedusa (positive) stations. This observation is
1012 consistent with AERONET/PHOTONS data analysed for a long-time period over the Mediterranean by Mallet
1013 et al. (2013), who report different spectral variations in SSA, following the aerosol regime (dusty and/or
1014 polluted particles). One of the main conclusions here is that aerosols are found to be moderately absorbing
1015 during the SOP-1a period, what is consistent with in-situ observations performed onboard the ATR-42
1016 aircraft and summarized by Denjean et al. (2015).

1017 **5.2.3 ATR-42 and F-20 aircraft observations**

1018 In parallel to surface observations, an example of the vertical profiles of aerosol optical properties obtained
1019 from ATR-42 measurements is shown Figure 20 that corresponds to the flight 35-36 over the station of
1020 Lampedusa for the 22nd of June (see also Denjean et al., 2015 and Nicolas et al., in prep.). Scattering
1021 coefficients (in Mm^{-1}) are plotted at 450, 550 and 700 nm (left) versus altitude (in meter). Completely
1022 different behaviours in the scattering spectral dependence as a function of altitude were observed. Two
1023 different aerosol plumes characterized by a significant spectral dependence (typically of submicronic
1024 polluted, smoke or fine marine aerosols) are observed around 1000 and 2000-2500 m. Above 3000 m, the
1025 spectral dependence is clearly reduced, corresponding to air masses with high mineral dust concentrations.
1026 For this upper aerosol layer, the scattering coefficient increases up to 60 Mm^{-1} . The analysis of the extinction

1027 (at 530 nm) vertical profiles obtained from the CAPS system (Table 3) reveals an excellent agreement with
1028 nephelometer data showing the peaks of extinction at similar altitudes (see Denjean et al., 2015), with
1029 maxima ($\sim 90 \text{ Mm}^{-1}$) logically observed within the dust plumes (4000-5000 m). Number concentrations, as
1030 well as volume size distributions, highlight the significant atmospheric loading by particles with diameter
1031 higher than $1 \mu\text{m}$ above 3000 m (maxima of $5000 \# \text{ cm}^{-3}$). For this atmospheric layer, the volume size
1032 distribution is characterized by a coarse mode, around 6-8 μm . As previously mentioned, vertical profiles of
1033 optical properties in terms of AE, SSA, asymmetry parameters as well as their spectral dependence are
1034 presented and discussed in details by Denjean et al. (2015) and Nicolas et al. (in prep.). The airborne SW
1035 and LW radiation measurements and the comparison with radiative transfer model simulations at
1036 Lampedusa are presented by Meloni et al. (in prep.).

1037 **5.3 Aerosol vertical structure**

1038 **5.3.1 Lidar surface observations**

1039 Although deeply analysed in other dedicated papers, some examples of the aerosol vertical profiles are
1040 presented here. First and over the Minorca station, surface lidar observations in Figure 21a were obtained
1041 during June 16 and 17, that corresponds to the first event of transported mineral dust over the western
1042 basin. They show a dust aerosol layer located between 1.5 and 5 km, with a maximum of aerosol extinction
1043 (at 355 nm) around 0.10 km^{-1} on 16th of June between 12:00 and 14:00 Local Time (LT). Comparisons of
1044 retrieved AOD with the lidar system is shown to be very consistent with sun-photometer observations for
1045 these two days (Figure 21a, top), with moderate AOD (at 355 nm) ranging between 0.2 and 0.4 at
1046 maximum. During 17 June, the dust layer is less intense and the aerosol extinction above 1.5 km decreases.
1047 After 14:00 LT, Figure 21a clearly shows that most of the contribution to AOD is due to the MBL over the
1048 Minorca station. At Ersa (Figure 21b), the dust event reached the northern tip of Corsica on 19 June. A deep
1049 depolarizing aerosol layer was observed at altitudes between 3 and 6 km. In the night of the 20th, the
1050 particulate depolarization ratio is close to 18% and the lidar ratio within the dust layer was estimated at 46
1051 sr. The extinction coefficient remains moderate within the dust layer $\sim 0.05 \text{ km}^{-1}$ (Figure 21b) between 4 and
1052 6 km. It should be noted that a complete analysis of lidar observations series obtained over the cape Corsica
1053 site is reported in Leon et al. (2015). The dust event vertical distribution is further analysed by means of the

1054 EARLINET lidar stations in Sicard et al. (2015) and by means of the EARLINET and ChArMEx lidar stations in
1055 Barragan et al. (in prep.).

1056 In addition to Minorca and Ersa, two lidars were also operated at Lampedusa during the SOP-1a and
1057 provided vertical profiles of aerosol backscattering and depolarization. The ENEA/University of Rome lidar
1058 measures the aerosol backscattering at 532 and 1064 nm, plus the depolarization at 532 nm. This system
1059 was operated throughout the campaign, although not continuously. The lidar data retrieval is described by
1060 Di Iorio et al. (2009), and uses sun-photometer AOD observations to constrain the determination of the
1061 aerosol backscattering profile. Figure 22a shows the evolution of the vertical profile of the aerosol
1062 backscattering coefficient at 1064 nm on 3 July 2013 at Lampedusa. At low altitudes the air masses reaching
1063 Lampedusa originated from the North. Air masses above 2 km conversely came from a southwesterly
1064 direction crossing North Algeria and Tunisia, and carried desert dust. Elevated backscattering attributed to
1065 dust was observed up to 5 km altitude, and a steep transition in the backscattering coefficient occurred at
1066 this altitude throughout the day. Figure 22b shows the backscattering coefficient profile at 532 and 1064
1067 nm, and the depolarization ratio measured at 15:45 UT by the ENEA/University of Rome and the LISA lidars.
1068 Evidently, the backscattering coefficient above 2 km shows small wavelength dependence, and elevated
1069 values of the depolarization ratio, as expected from large irregular desert dust particles (Sassen, 1999). The
1070 influence of large particles is smaller below 2 km, where the backscattering coefficient shows some
1071 dependency on wavelength, and the depolarization ratio decreases. The significant role played by the large
1072 particles on 3 July is also confirmed by the aerosol size distribution and optical properties (i.e., values and
1073 spectral dependency of the refractive index and single scattering albedo) retrieved from the AERONET
1074 observations at Lampedusa. The average AOD (at 500 nm) was 0.28, and the AE (calculated between 440
1075 and 870 nm) was 0.39, as expected for cases with a large contribution of desert dust. The retrieved
1076 columnar volume size distributions on the two days show that the mode with a median radius around 2 μm
1077 is 2-3 times more intense on 3 July than on 17 June.

1078 Finally, nighttime measurements at Potenza (Italy) on 21 June starting at 23:40 UT, which coincides with the
1079 arrival of the Saharan dust event over southern Italy, indicate a clear signature of Saharan dust in the
1080 tropospheric layer between 1.8 and 3.9 km, an extinction-related AE value of approximately 0 is measured

1081 between roughly 2 and 3 km and a quite constant LR around 50 sr at both 355 and 532 nm (not shown, see
1082 Sicard et al., 2015a; Barragan et al., in prep.).

1083 **5.3.2 LNG observations**

1084 An example of LNG (Lidar Nouvelle Génération) observations onboard the F-20 aircraft is presented in the
1085 Figure 23 for the 19th of June that corresponds to a flight (12:46 to 13:26 TU) from Sardinia to the Gulf of
1086 Genoa. The aerosol extinction (in km^{-1} and at 532 nm) is represented in function of latitude during this flight
1087 as well as the associated AOD with a high temporal and spatial frequency. One can observe the significant
1088 North-South gradient during this dust event with low-values of AOD (around 0.1 at 532 nm) for latitude of
1089 44°N and moderate-high AOD (0.40 to 0.55) for latitudes lower than 42-43°N. In terms of vertical structure,
1090 this increase of AOD is due to an upper dust layer (around 5 to 6 km) characterized by an aerosol extinction
1091 of about 0.1 km^{-1} . This intense dust layer transported over most of the investigated region (40.5°N-43.5°N) is
1092 associated with a second more diluted aerosol layer observed between 3 and 4 km with LNG. Another
1093 interesting aspect is the variability of aerosol extinction detected in the marine boundary layer showing
1094 large differences throughout the F-20 transect. The aerosol extinction is found to be significant around 41°N
1095 to 41.5°N that could be due to sea-spray particles generated in south Corsica Island due to the local
1096 acceleration of the wind occurring between the Corsica and Sardinia islands (not shown). This increase of
1097 the aerosol loading in the MBL associated with dust aerosol transported to higher altitudes results in an
1098 increase of total AOD at these latitudes. Such aircraft lidar data will be useful for testing the different
1099 modeling systems used for the SOP-1a experiment and more specifically their ability to reproduce complex
1100 vertical aerosol structures over the western Mediterranean. Additional observations of the aerosol
1101 extinction vertical profile obtained over different surface-stations from the passive remote-sensing PLASMA
1102 instrument onboard the ATR-42 aircraft are presented in Torres et al. (in prep.).

1103 **5.3.3 Sounding balloon observations**

1104 Figure 24 shows an example of the vertical profile of the aerosol particle size distribution obtained on June
1105 19 near the end of the dust episode that started on 16 June over Minorca. The daytime average AOD
1106 geographical distribution derived from MSG/SEVIRI is shown in Figure 6. The vertical profile clearly shows
1107 the presence of the dust layer between about 2.5 and 4.5 km in altitude, in agreement with coincident lidar

1108 continuous observations at Minorca that show the more limited vertical extent of dust compared to
1109 previous days and the end of the episode on June 19 in this area (Chazette et al., submitted). It should be
1110 noted that sounding balloons appear to under-detect very large particles within dust layers compared to the
1111 drifting balloons. This can be due isokinetic sampling differences between sounding systems that have a
1112 vertical velocity of several m s^{-1} and systems drifting at a constant air density that are quasi-Lagrangian.
1113 However coincident AERONET and LOAC vertically integrated particle size distribution in the range 0.1-
1114 $30 \mu\text{m}$ in diameter performed on June 16 and 17 were found quite comparable. In the marine atmospheric
1115 boundary layer, the LOAC speciation index (Renard et al., 2015a) indicates hydrated particles. In the free
1116 troposphere above dust, the concentration of particles rapidly decreased by one order of magnitude and
1117 particles were mainly of submicronic size with sometimes a significant number of particles in the 1.1-3 μm
1118 channel.

1119 **5.4 Local Direct Radiative Forcing**

1120 **5.4.1 Estimates using in-situ aircraft data and radiative transfer codes over the two super-sites**

1121 Before investigating the possible climatic effect of aerosols on the Mediterranean climate, an important
1122 preliminary step is the calculation of the direct radiative forcing (DRF) exerted by aerosols. This can be
1123 addressed by using in-situ (physical-optical properties) and remote-sensing (vertical profiles) observations
1124 of aerosols as input to radiative transfer models. Simulated SW and LW radiative fluxes can be evaluated
1125 using observed radiative fluxes both at the surface and onboard the two aircraft. The combination of in-situ
1126 and remote sensing measurements provide a complete and unique dataset for conducting such 1-D
1127 radiative transfer simulations. To this end, vertical profiles from the ATR-42 were combined with surface
1128 observations from the two (Ersa and Lampedusa) stations to calculate the SW DRF of different aerosol
1129 events (Nicolas et al., in prep.; Meloni et al., in prep.). Over the western basin and for the first period of the
1130 campaign (16 to 20 June), different calculations, with the GAME radiative transfer model (Dubuisson et al.,
1131 2004), of the downward and upward SW cloud-free irradiances have been performed by Nicolas et al. (in
1132 prep.) for 6 vertical profiles over Granada, Minorca and Corsica islands. Briefly, the methodology is based on
1133 extinction, SSA and phase function vertical profiles (and their spectral dependence), obtained from
1134 observations and Mie calculations, and associated with atmospheric thermodynamic properties. They

1135 clearly show a significant change in surface radiative fluxes with a well-known decrease (dimming effect) of
1136 downward radiations due to scattering and absorption of solar radiation by dust aerosols. Inter-comparisons
1137 between observed/simulated downward and upward clear-sky SW fluxes show a good agreement during
1138 the ascent and descent profiles. At TOA, Nicolas et al. (in prep.) reported a direct (instantaneous at noon)
1139 SW DRF ranged between -4 and -33 W m⁻², revealing a cooling effect due to dust particles. These
1140 simulations also indicate that the decrease in surface radiation is not completely compensated by the TOA
1141 cooling, meaning that aerosols exerted a positive atmospheric forcing due to their ability to absorb solar
1142 radiations.

1143 Similar calculations (not shown) have been done over the Lampedusa reference-site by Meloni et al. (in
1144 prep.) by using a similar method based on lidar, sun-photometer, in-situ surface, ATR-42 and F-20
1145 observations and the MODTRAN 5.3 radiative transfer code. Meloni et al. (in prep.) estimate both the SW
1146 and the LW aerosol radiative forcing profiles and the balance between the two spectral components (SW
1147 and LW). During the descent towards Lampedusa airport on 22 June, the instantaneous (12.5° solar zenith
1148 angle and aerosol optical depth at 500 nm of 0.32) SW cooling at the surface (-44 W m⁻²) is reduced by
1149 about 10% due to infrared emission. The dust SW radiative forcing at TOA is -6 W m⁻². These values are
1150 obtained using the AERONET aerosol size distribution and different aerosol refractive indices in the SW and
1151 in the LW spectral regions. The LW contribution at the surface is lower than the values reported in previous
1152 studies (di Sarra et al., 2011; Meloni et al., 2015), partially due to the different solar zenith angle and to the
1153 presence of mixed aerosol below the dust layer down to the surface.

1154 **5.4.2 Estimates of instantaneous clear-sky SW DRF using AERONET/PHOTONS observations**

1155 As reported previously, AERONET/PHOTONS network provides, in addition to microphysical and optical
1156 aerosol properties, an estimate of the local (instantaneous) clear-sky direct radiative forcing at any
1157 AERONET/PHOTONS location as an operational product of the network. The method of derivation is
1158 described in Garcia et al. (2012). As mentioned above, the extremely good regional coverage of
1159 AERONET/PHOTONS sun-photometer instruments during the SOP-1a allow a complementary estimate of
1160 the local radiative (clear-sky) forcing to those derived by Meloni et al. (in prep.) and Nicolas et al. (in prep.).
1161 The Figure 25 indicated the averaged of all instantaneous (clear-sky) DRF (in W m⁻²) estimated during a day

1162 for both AERONET/PHOTONS station. Estimates are reported at the surface (bottom left), at TOA (bottom
1163 right) and within the total atmosphere (down). Averaged values of the DRF are also indicated in the Figure
1164 25. As mentioned above, sun-photometers retrievals demonstrate a significant DRF during the SOP-1a
1165 experiment. As an example and at the surface, the mean forcing is comprised between -15 W m^{-2}
1166 (Barcelona, not affected by dust transport) and -35 W m^{-2} in Burjassot. Such values are consistent with
1167 independent 1-D estimates reported by Nicolas et al. (in prep.) and Meloni et al. (in prep.).
1168 AERONET/PHOTONS data also reveal a negative DRF at TOA over most of sites, meaning that aerosols exert
1169 in majority a cooling effect at TOA, with values around ~ -6 to -12 W m^{-2} . These negative values are also due
1170 to the fact that most of AERONET/PHOTONS stations are located over islands, which are characterized by
1171 low surface albedo. Logically and due to the moderate values of aerosol absorption observed during the
1172 SOP-1a (Denjean et al., this special issue), a positive atmospheric forcing is observed with mean values from
1173 $+7$ to $+30 \text{ W m}^{-2}$ (with maxima in Burjassot), that could affect the vertical profiles of temperature and
1174 relative humidity as shown recently by Nabat et al. (2015a).

1175 **5.4.3 Estimates using in-situ radiative flux observations**

1176 As shown by di Sarra et al. (2011), an estimate of the aerosol radiative forcing can be obtained by comparing
1177 irradiance measurements made during days characterized by different aerosol loads. In particular, the
1178 identification of a cloud-free day with low aerosol amounts is important to provide a reference for pristine
1179 conditions. During the SOP-1a, 17 June at Lampedusa displayed a very low aerosol optical depth (daily
1180 average of 0.064 at 500 nm) and cloud-free conditions throughout the day, and was identified as the
1181 reference day for pristine conditions. July 3, conversely, was one of the days characterized by the presence
1182 of desert dust, with moderate values of the AOD (0.28). As shown in figure 22a, dust was present above 2
1183 km altitude and there were no major changes in the aerosol vertical distribution during the day, as it also
1184 appears from the limited daily variability of the AOD (daily standard deviation of the AOD at 500 nm of
1185 0.015). Cloud-free conditions were present throughout the day.

1186 Figure 27 displays the downward solar irradiance measured on 3 July, compared with the one measured on
1187 the pristine reference day (17 June). The irradiance measurements were corrected for the radiometer
1188 thermal offset as discussed by Di Biagio et al. (2009). The sharp narrow peak occurring on 17 June around

1189 6:30 was related to a small isolated cloud, and these data were discarded from the analysis. The differences
1190 between the downward irradiances measured on these two days were calculated as a function of the solar
1191 zenith angle; these differences are due to the effect of aerosol and, to a smaller extent, column water
1192 vapour. The effect of water vapour was estimated by means of a radiative transfer model (see e.g., di Sarra
1193 et al., 2011), and the remaining difference was integrated over 24 hours to obtain the daily average effect,
1194 ΔI , on the downward solar irradiance. The daily aerosol radiative forcing RF can be derived as:

$$1195 \text{ RF} = \Delta I(1-A)$$

1196 where ΔI is the difference between the two curves of Figure 27 integrated over 24 hours, and A is the
1197 surface albedo. For a surface albedo of 0.07 (di Sarra et al., 2011), the estimated surface RF is -14.8 W m^{-2} .

1198 The radiative forcing efficiency (RFE), which is the radiative forcing produced by a unit AOD, was calculated
1199 as:

$$1200 \text{ RFE} = \text{RF} / (\text{AOD}_2 - \text{AOD}_1)$$

1201 where AOD_1 and AOD_2 are the measured daily average aerosol optical depth on 17 June and 3 July,
1202 respectively. The estimated RFE is -67.4 W m^{-2} . Di Biagio et al. (2010), based on a multi-year dataset at
1203 Lampedusa, derived a similar value for desert dust (-68.9 W m^{-2}) at the equinox; di Sarra et al. (2010), for an
1204 intense desert dust event occurring in March 2010 found values between -70 and -85 W m^{-2} . For a desert
1205 dust event associated with the propagation of a gravity wave, with values of AOD similar to those of 3 July,
1206 di Sarra et al. (2013) derived an RFE equal to -79 W m^{-2} . Valenzuela et al. (2012) determined REF for
1207 Saharan dust episodes over the western Mediterranean with different origins, showing values in the range
1208 from -74 W m^{-2} (for air masses coming from North Morocco) to -65 W m^{-2} (for air masses coming from
1209 Algeria and Tunisia). Values of the dust RFE at the surface in the same range were obtained by Derimian et
1210 al. (2006), although they were derived in different conditions for which the influence of surface albedo
1211 should be taken into account.

1212 The downward LW irradiance measured on 3 July was higher than on 17 June by 23 W m^{-2} . Most of this
1213 effect is due to differences in the water vapour column amount (about 1 cm difference between the two
1214 days, with larger values on 3 July). Once the water vapour contribution was subtracted by means of
1215 radiative transfer calculations, we found a net positive effect induced by the aerosol of about $+5.5 \text{ W m}^{-2}$.

1216 This is, on the daily timescale, about 35% of the SW effect. The resulting aerosol RFE in the LW spectral
1217 range is $+25.5 \text{ W m}^{-2}$, in agreement with previous results by di Sarra et al. (2011) who found values between
1218 $+25.9$ and $+27.9 \text{ W m}^{-2}$, or Anton et al. (2014) who reported RFE values around $+20 \text{ W m}^{-2}$ (in reference to
1219 AOD at 675 nm).

1220 **5.4.4 Estimations of the SW and LW radiative heating rate along the vertical**

1221 One important original aspects of this study concerns the estimates of the vertical profiles of SW and LW
1222 radiative heating rate. To our knowledge, all the referenced estimates of this important parameter, which
1223 controls for a part the semi-direct radiative effect of aerosols, have been conducted using remote-sensing
1224 techniques or in-situ observations of aerosol optical properties, coupled with radiative transfer modeling.
1225 Here, we propose a first estimate of the SW and LW heating rate derived directly from upward and
1226 downward (SW and LW) radiative fluxes obtained on-board the ATR-42 aircraft. Because of the nature
1227 mainly diffuse of longwave upward and downward irradiances (irradiances in thermal infrared), and of the
1228 upward shortwave irradiance (irradiance in solar domain), in first approximation, no correction due to the
1229 altitude of the aircraft will be applied to these measurements. Only shortwave downward irradiances will
1230 be corrected. Three kinds of corrections are applied:

- 1231 - Correction of the aircraft attitude (unavoidable movements due to the aircraft pitch and roll)
- 1232 - Correction of cosine response of the pyranometer
- 1233 - Correction due to the non-horizontal position of the sensor when a stabilized leg (ie. determination
1234 of offsets on roll and pitch)

1235 Let θ_m the angle between the sun direction and the normal to the pyranometer sensor (depending on pitch,
1236 roll and aircraft heading given by the inertial navigation system), and θ_s the solar zenith angle, the attitude
1237 correction coefficient is:

$$1238 \quad X_d^n = \frac{\cos \theta_m}{\cos \theta_s}$$

1239 Finally, we obtain the global (direct plus diffuse) downward irradiance, for the solar zenith angle θ_s :

$$1240 \quad E_{SW}^\downarrow(\theta_s) = \frac{E_{SW}^{m\downarrow}(\theta_m)}{(X_d^n [1 - c(\theta_s)] - D) f(\theta_s) + D}.$$

1241 In this equation, $E_{SW}^{m\downarrow}(\theta_m)$ is the measured global irradiance, $c(\theta_s)$ is the cosine response of the
1242 pyranometer, $D = 2 \int_0^1 [1 - C(\theta_m)] \mu d\mu$ and $f(\theta_s)$ is the part of direct downward irradiance in the global
1243 (estimation obtained from radiative transfer code). Taking into account these corrections, Figure 28a shows
1244 downward (E_{SW}^{Dwn}), upward (E_{SW}^{Up}), and net (E_{SW}^{Net}) shortwave irradiances obtained from measurements
1245 performed onboard ATR-42 aircraft on 22 June between 10.35 and 11.30 TU. Irradiances are reduced to the
1246 mean solar zenith angle $\theta_s = 29.7^\circ$. Similarly, Figure 28b shows corresponding measurements of
1247 downward (E_{LW}^{Dwn}), upward (E_{LW}^{Up}), and net (E_{LW}^{Net}) longwave irradiances. Total net irradiances are then
1248 determined versus the aircraft altitude for the mean air mass factor of the considered studied flight phase.
1249 Radiative cooling/heating rate is finally derived and shown in the figure 28c, in which the longwave (LW)
1250 and shortwave (SW) parts are distinguished.

1251 Concerning the SW heating rate vertical profiles (Figure 28c), one can observe the significant increase of
1252 the calculated instantaneous SW heating rate in the two different aerosol layers detected for this case
1253 (Figure 21), especially above 4 km, that corresponds to the maximum of extinction coefficient (up to 100
1254 Mm^{-1}) due to the presence of mineral dust. For this specific layer, the values of SW heating rate peak at 4-5
1255 $^\circ K$ per day for a solar angle of 29.7° . We can also observe a similar tendency in the second aerosol layer,
1256 located between 1.5 and 3 km (see Figure 21). Concerning the LW heating rate, the figure 28c indicates
1257 instantaneous values ranging between -2 to -4 $^\circ K$ per day, which is also consistent with the well known
1258 cooling effect of mineral dust in the longwave spectrum (Mallet et al., 2006, Zhu et al., 2007). As shown in
1259 Figure 28c, the net heating rate is dominated by the SW heating (the maximum LW cooling is less than 60%
1260 of the SW heating), which leads to net SW radiative heating ranging between +0.5 and +2 K per day inside
1261 the dust layer above the MBL. Such unique and original database of SW and LW radiative heating obtained
1262 over the western Mediterranean should be now used to evaluate the ability of the different models
1263 involved in the ChArMEx/ADRIMED project (see the following section 6) to simulate this important radiative
1264 property for the different identified dust cases.

1265 **6. Overview of Modeling Activities**

1266 Several models are used to analyze the SOP-1a period: the meso-scale meteorological COSMO-MUSCAT
1267 model, the chemistry transport model (CTM) CHIMERE model, and two regional climate (RegCM and CNRM-
1268 RCSM) models. These models differ in terms of horizontal and vertical resolutions, physical
1269 parameterizations, aerosol-chemical schemes and are able to deliver complementary information to
1270 address key scientific questions of the ChArMEx/ADRIMED experiment. Their main characteristics are
1271 summarized in Table 8.

1272 **6.1 COSMO-MUSCAT model**

1273 The parallelized multi-scale regional model system COSMO-MUSCAT (Wolke et al., 2012) consists of the non-
1274 hydrostatic atmosphere model COSMO (Consortium for Small-scale Modelling) that is on-line coupled to the
1275 3-D chemistry tracer transport model MUSCAT (MULTiScale Chemistry Aerosol Transport Model). The
1276 atmospheric dust cycle consisting of the emission, transport and deposition of dust particles is simulated
1277 within MUSCAT using meteorological and hydrological fields from COSMO. Dust emission is calculated using
1278 the emission scheme by Tegen et al. (2002) and depends on local surface wind friction velocities, surface
1279 roughness length, soil texture and soil moisture. Calculated dust emission fluxes depend on particle
1280 diameter for individual size classes that are assumed to be log-normally distributed. Following Marticorena
1281 and Bergametti (1995), dust emission is considered as threshold function of local friction velocities and thus
1282 initial dust emission is computed as a function of soil particle size distribution. Dust emission is limited to
1283 regions where active dust sources have been identified during 2006-2009 from MSG SEVIRI observations
1284 (Schepanski et al., 2007). The advection of dust particles is described by a third order upstream scheme;
1285 dust particles are transported as passive tracer in five independent size classes with limiting radius at
1286 $0.1\mu\text{m}$, $0.3\mu\text{m}$, $0.9\mu\text{m}$, $2.6\mu\text{m}$, $8\mu\text{m}$, and $24\mu\text{m}$. The removal of dust particles from the atmosphere is
1287 described by dry and wet deposition taking particle size, particle density, and atmospheric conditions into
1288 account. Here, the simulations of the atmospheric dust cycle are performed at a 28 km horizontal grid and
1289 40 vertical layers, covering North African dust sources, the eastern North Atlantic, the Mediterranean basin
1290 and Europe.

1291 **6.2 The CHIMERE chemistry-transport model**

1292 CHIMERE is a chemistry-transport model able to simulate concentrations fields of gaseous and aerosols

1293 species at a regional scale. The model is off-line and thus needs pre-calculated meteorological fields to run.
1294 In this study, we used the version fully described in Menut et al. (2013), forced by the WRF meso-scale
1295 model. The horizontal domain is the same as the one of WRF, and, for the vertical grid, the 28 vertical levels
1296 of WRF are projected on the 20 levels of the CHIMERE mesh. The gaseous species are calculated using the
1297 MELCHIOR 2 scheme and the aerosols using the scheme developed by Bessagnet et al. (2004). This module
1298 takes into account species such as sulfate, nitrate, ammonium, primary organic (OC) and black carbon (BC),
1299 secondary organic aerosols (SOA), sea-spray, mineral dust, and water. These aerosols are represented using
1300 ten bins, from 40 nm to 20 μm , in diameter. The life cycle of these aerosols is completely represented with
1301 nucleation of sulfuric acid, coagulation, adsorption/desorption, wet and dry deposition and scavenging. This
1302 scavenging is both represented by coagulation with cloud droplets and precipitation. The formation of SOA
1303 is also taken into account. The anthropogenic emissions are estimated using the same methodology as the
1304 one described in Menut et al. (2013) but with the HTAP masses as input data. These masses were prepared
1305 by the EDGAR Team, using inventories based on MICS-Asia, EPA-US/Canada and TNO databases
1306 (http://edgar.jrc.ec.europa.eu/htap_v2). Biogenic emissions are calculated using the MEGAN emissions
1307 scheme (Guenther et al., 2006), which provides fluxes of isoprene, terpene and pinenes. In addition to this
1308 2013 version, several processes were improved and added in the framework of this study. First, mineral dust
1309 emissions are now calculated using new soil and surface databases, as described in Menut et al. (2013).
1310 Second, chemical species emissions fluxes produced by vegetation fires are estimated using the new high
1311 resolution fire model presented in Turquety et al. (2014). Finally, the photolysis rates are explicitly
1312 calculated using the FastJ radiation module (Mailler et al., 2015).

1313 **6.3 The RegCM Regional Climate model**

1314 The RegCM system is a community model designed for use by a varied community composed of scientists in
1315 industrialized countries as well as developing nations. It is supported through the Regional Climate Network,
1316 or RegCNET, a widespread network of scientists coordinated by the Earth System Physics section of the
1317 Abdus Salam International Centre for the Theoretical Physics (ICTP, Giorgi et al., 2012). RegCM is a
1318 hydrostatic, compressible, sigma-p vertical coordinate model. As a limited area model, RegCM requires
1319 initial and boundary conditions that can be provided both by NCEP or ECMWF analyses. The horizontal

1320 resolution used need to be higher than 10 km, due to the hydrostatic dynamic core of the model, associated
1321 with 23 vertical levels. A simplified aerosol scheme specifically designed for application to long-term climate
1322 simulations has been incrementally developed within the RegCM system. Solmon et al. (2006, 2008) first
1323 implemented a first-generation aerosol model including sulfates, organic carbon, and black carbon. Zakey et
1324 al. (2006) then added a 4-bin desert dust module, and Zakey et al. (2008) implemented a 2-bin sea-spray
1325 scheme. In RegCM, the dust emission scheme accounts for sub-grid emissions by different types of soil. The
1326 dust emission size distribution can now also be treated according to Kok (2011). When all aerosols are
1327 simulated, 12 additional prognostic equations are solved in RegCM, including transport by resolvable scale
1328 winds, turbulence and deep convection, sources, and wet and dry removal processes. In RegCM, the
1329 natural/anthropogenic aerosols are radiatively interactive both in the solar and infrared regions and so are
1330 able to feedback on the meteorological fields.

1331 **6.4 The CNRM-RCSM Regional Climate model**

1332 The fully coupled RCSM (Regional Climate System Model), which is developed at CNRM has been also used
1333 within the ChArMEx/ADRIMED project. This model includes the regional climate atmospheric model
1334 ALADIN-Climate (Déqué and Somot 2008), the regional ocean model NEMOMED8 (Beuvier et al., 2010) and
1335 the land-surface model ISBA (Noilhan and Mahfouf, 1996). We used here the version described in Nabat et
1336 al. (2015b) with a 50 km horizontal resolution. ALADIN-Climate includes the Fouquart and Morcrette
1337 radiation scheme based on the ECMWF model incorporating effects of greenhouse gases as well as direct
1338 effects of aerosols. The ocean model NEMOMED8 is the regional eddy-permitting version of the NEMOV2.3
1339 ocean model that covers the Mediterranean Sea. Concerning the aerosol phase, the model ALADIN-Climate
1340 incorporates a radiative scheme to take into account the direct and semi-direct effects of five aerosol types
1341 (sea-spray, desert dust, sulfates, black and organic carbon aerosols) through either AOD climatologies or a
1342 prognostic aerosol scheme (Nabat et al., 2013, 2015b). On the one hand, Nabat et al. (2013) have proposed
1343 a new AOD monthly climatology over the period 2003-2009, based on a combination of satellite-derived
1344 and model-simulated products. The objective is having the best estimation of the atmospheric aerosol
1345 content for these five most relevant aerosol species. On the other hand, a prognostic aerosol scheme has
1346 been recently implemented in ALADIN-Climate, and has shown its ability to reproduce the main patterns of

1347 the aerosol variability over the Mediterranean (Nabat et al., 2015b).
1348 Using CNRM-RCSM with the new AOD monthly climatology over the period 2003-2009 (Nabat et al., 2013),
1349 Nabat et al. (2015a) have notably highlighted the response of the Mediterranean Sea Surface Temperature
1350 (SST) to the aerosol direct and semi-direct radiative forcing. Figure 29a presents the annual average
1351 difference in SST over the period 2003-2009 between a simulation ensemble including aerosols and a
1352 second one without any aerosol. Aerosols are found to induce an average decrease in SST by 0.5°C, because
1353 of the scattering and absorption of incident radiation. As a consequence, the latent heat loss is also reduced
1354 by aerosols (Figure 29b), as well as precipitation (Figure 29c). This result also underlines the importance of
1355 taking into account the ocean-atmosphere coupling in regional aerosol-climate studies over the
1356 Mediterranean.

1357 **6.5 SOP-1a multi-model aerosol simulations**

1358 **6.5.1 Aerosol Optical Depth**

1359 Figure 30 reports the AOD (in the visible range) simulated for the SOP-1a period and for the COSMO-M (550
1360 nm), RegCM (between 440 and 670 nm), CNRM-RCSM (550 nm) and CHIMERE (500 nm) models. Except the
1361 CTM-CHIMERE model which includes all the secondary species (SOA and inorganic), the others have
1362 different aerosols schemes and take into account both natural (COSMO-M) or natural plus a part of
1363 anthropogenic aerosols as described in Table 7. The configurations used for each models are listed in Table
1364 7. One can observe the large variability of AOD simulated by models over the Mediterranean region with
1365 highest values clearly simulated by the COSMO-M (AOD ~1-1.5 in the visible wavelengths) over the
1366 Northern Africa region. The CHIMERE model indicates two different regions where AOD peaks around 1,
1367 over Algeria-Tunisia and southern of Morocco. For COSMO-M and CHIMERE, no intense dust AOD are
1368 simulated over the northeast Africa (Lybia and Egypt) and values are below 0.25, contrary to RegCM and
1369 CNRM-RCSM that simulate moderate AOD over this region with more intense peaks (~0.7 for CNRM-RCSM
1370 simulations). Some identified regions with important AOD over Tunisia, Algeria, and South Morocco are well
1371 captured by all models except COSMO-M which show more intense AOD south of Algeria. It should be noted
1372 that this regional pattern of AOD is found to be consistent with MODIS observations as shown by Menut et
1373 al. (2015) for the CHIMERE model. Averaged over the SOP-1a period, all models simulate low to moderate

1374 AOD over the EURO-Mediterranean region which is consistent with AERONET/PHOTONS observations
1375 (Figure 14). Once again and as noted by Menut et al. (2015), this modeling exercise clearly shows that the
1376 summer 2013 was not characterized by intense dust plumes or intense anthropogenic or forest fire
1377 emissions. However, modeling results indicate regular dust intrusions during the SOP-1a characterized by
1378 moderate atmospheric loads. Over Europe, the CTM CHIMERE model obviously simulates anthropogenic
1379 aerosol AOD (AOD ~ 0.3), especially over the Benelux and Pô Valley that are not simulated by the two other
1380 regional models. Indeed, CNRM-RCSM simulations reveal a more diffuse AOD about 0.2 over Europe with
1381 maximum over Western France certainly due to the advection of primary marine particles generated over
1382 the Atlantic Ocean. RegCM simulations indicate a plume of anthropogenic aerosols over the Balkan region
1383 mainly due to secondary inorganic species. As RegCM does not use the spectral nudging technique in this
1384 simulation and are only forced at the boundaries during the period of simulation, some biases in
1385 meteorological fields could appear (as for the precipitation location and intensity), which need to be
1386 evaluated. Finally and in addition to analysis of the AOD regional pattern, a specific comparison with in-situ
1387 observations and remote-sensing (AERONET/PHOTONS and satellite) data has been made for the CTM-
1388 CHIMERE model (Menut et al., 2015) and is planned in accompanied studies for the COSMO-M, RegCM and
1389 CNRM-RCSM models, associated with an inter-comparison exercise for evaluating the dust emissions,
1390 vertical distribution, size distribution and dry/wet deposition using all data collected in the framework of
1391 the SOP-1a.

1392 In parallel to time averaged AOD simulated at the regional scale, we report comparisons of simulated AOD
1393 with AERONET/PHOTONS data for the two reference stations (Lampedusa and Ersa). As reported in Table 7,
1394 it should be reminded here that all models did not take into account aerosol species in a similar way. As an
1395 example, COSMO-MUSCAT includes mineral dust only in this simulation, while CNRM-RCSM and RegCM
1396 model include natural (sea-spray and dust) and sulfates as well as secondary ammonium and nitrate
1397 particles (treated as bulk aerosols) but for RegCM only. The most complete regional model is the CTM-
1398 CHIMERE, which takes into account natural and all anthropogenic particles (including secondary organics
1399 and inorganic) resolved in size by using a number of bins (Menut et al., 2013) higher than used in RegCM,
1400 CNRM-RCSM or COSMO-MUSCAT (number of dust bins between 3 to 4 bins) models. Figure 31 reports the

1401 time evolution of simulated and observed AOD at 550 nm for the two sites (Ersa and Lampedusa) during the
1402 SOP-1a. Time correlation, as well as bias, is calculated after removing AERONET/PHOTONS data for the 27th
1403 of June, strongly affected by smoke aerosols transported from Northern America biomass burning sources
1404 that are not included in the different domains. Figure 31 indicates that all models are able to simulate AOD
1405 in the range of magnitude of observations. For the dusty Lampedusa site, CNRM-RCSM and CHIMERE reveal
1406 high temporal correlations (0.82, 0.85, respectively), with standard deviations close to AERONET/PHOTONS
1407 data, especially for CHIMERE. For this station, COSMO-M and RegCM display moderate temporal correlation
1408 (0.55 and 0.49, respectively) compared to CNRM-RCSM and CHIMERE. As already mentioned, one reason of
1409 lowest time-correlation for these models is related to the fact that they are only forced at the boundaries
1410 and the synoptic conditions inside the domain can derive during the simulation. This effect is limited for
1411 CNRM-RCSM that used the spectral nudging technique and for CHIMERE forced by WRF meteorological field
1412 (Menut et al., 2015). For each models, biases are shown to be low, both positive (for CNRM-RCSM and
1413 CHIMERE) and negative (for COSMO-M and RegCM).

1414 For the Ersa station, less influenced by long-range transport of mineral dust during this period, temporal
1415 correlations are lowest and found to be moderate (0.40) for CHIMERE and COSMO-M and low for RegCM
1416 and CNRM-RCSM. In terms of bias, values are positive and low (0.02 to 0.04) for all models, except for
1417 COSMO-M (-0.07) that does not include anthropogenic aerosols nor sea-spray in the present simulation
1418 (Table 7). For each model, calculated standard deviations are in the same range of magnitude but slightly
1419 higher than observations, especially for RegCM (bias of 0.08) that simulated a large AOD for 19-20 of June
1420 period. By comparison with the values obtained in Lampedusa, these low correlations at Ersa reveal the
1421 limitations of these models in terms of horizontal resolution with respect to the representativeness of the
1422 site. Lampedusa being isolated in the middle of the Mediterranean and under the main pathways of African
1423 mineral dust, AOD is mostly related to long-ranged transport. On the other hand, the site of Ersa in Corsica
1424 may be under several types of aerosols contributions (anthropogenic, biogenic) more intense and more
1425 spatially variables than in Lampedusa. Ersa being closer to large industrial areas, the models with a
1426 horizontal resolution of tens of kilometers are probably not highly enough resolved to catch small scales
1427 aerosols plumes from the continent.

1428 **6.5.2 Regional SW 3-D direct radiative forcing**

1429 The SW (clear-sky) DRF, averaged for the SOP-1a period, has been estimated from the RegCM and CNRM-
1430 RCSM models, both at the surface and TOA, as shown in the Figure 32. For this discussion, we only consider
1431 these two models as they estimate the clear-sky SW DRF by taking into account natural and anthropogenic
1432 aerosols, contrary to the COSMO-MUSCAT model in this study. At the surface first, one can observe the
1433 large regional dimming due to anthropogenic (especially over Europe) and natural (Northern Africa and
1434 Mediterranean) particles over the Euro-Mediterranean. Concerning the North African region, both models
1435 simulate large surface forcing $\sim -20 \text{ W m}^{-2}$ (with local maxima of -50 W m^{-2} associated with higher AOD).
1436 CNRM-RCSM is shown to simulate higher surface radiative forcing for the whole domain, especially over
1437 Algeria. Although such RCM climate models are not designed to simulate finely the size distribution and the
1438 chemical composition of aerosols as an A-Q system (Menut et al., 2013), a first estimate of the radiative
1439 effect of polluted particles over Europe is provided. Figure 32 displays a negative forcing, obviously lower
1440 than for mineral dust, of about -10 to -15 W m^{-2} for RegCM, especially over Balkans and no significant
1441 radiative effect over the Benelux region for this period. Over the continental region, CNRM-RCSM simulated
1442 a more diffuse surface forcing with values around -10 W m^{-2} , including a large part of Europe (France,
1443 Benelux and Eastern Europe). As shown recently by Nabat et al. (2015a), this decrease in SW radiations due
1444 to aerosols could perturb the surface continental temperature, SST and latent heat fluxes over the
1445 Mediterranean Sea and more largely on meteorological fields.

1446 At TOA, the dipole of the direct forcing between the North and the South of the domain is well reproduced
1447 by the two RCM systems with more intense values for CNRM-RCSM. One can clearly observe positive forcing
1448 at TOA (heating) over Northern Africa and negative forcing (cooling) over the Mediterranean and Europe.
1449 This represents one of the characteristics of the Euro-Mediterranean region with a large variability of
1450 surface albedo from the South (with higher values) to the North (low to moderate albedo). Due to this
1451 gradient in the surface albedo, moderate absorbing dust aerosols emitted over Northern Africa
1452 (characterized by high surface albedo) decrease the shortwave radiations reflected at TOA, compared to a
1453 non-turbid atmosphere. When advected above low surface reflectance as marine or dense forest over
1454 Europe, dust aerosols increase the upward SW radiations at TOA, leading to a cooling effect. One can see

1455 the transition between positive to negative TOA forcing that occurs over Northern Algeria and Morocco as
1456 soon as dust particles are transported over darker surfaces. This TOA radiative forcing gradient is well
1457 captured by such RCM models which use a finer resolution than GCM. Over Europe and Mediterranean, the
1458 TOA forcing is simulated to be negative for both RCM with lower values around -5 to -10 W m^{-2} . Such results
1459 are consistent with the study of Nicolas et al. (in prep.), who performed two different simulations using
1460 different surface albedo (from marine to continental), based on the ATR-42 observations above the Balearic
1461 Islands and the Granada station. The inclusion of high surface albedo (0.27 at 870 nm) in the 1-D radiative
1462 transfer model compared to low sea-surface albedo (0.02 at 870 nm) contributes to decrease the TOA
1463 radiative effect at Granada.

1464 The last important point to mention here concerns the fact that most of SW radiations losses at the surface
1465 are not completely compensated by fluxes reflected back to space. Hence, this gain of solar energy within
1466 dusty layers (due to moderate dust SW absorption, see Denjean et al., this special issue) has been shown to
1467 result in significant feedbacks on the temperature and relative humidity profiles over the Mediterranean
1468 region with some important implications on its climate (Nabat et al., 2015a).

1469 **7. Conclusions**

1470
1471 The special observing period (SOP-1a) performed during the Mediterranean dry season (11 June to 05 July
1472 2013) over the western and central Mediterranean basins has been described in detail, as well as the 1D to
1473 3D modeling effort, involved in the ChArMEx/ADRIMED project focused on aerosol-radiation-climate
1474 interactions. Details of the in-situ and remote-sensing instrumentation deployed at the different sites and
1475 the main meteorological conditions that occurred during the campaign have been provided. Some results
1476 from the in-situ and remote-sensing observations, vertical profiles, 1-D and 3-D aerosols direct radiative
1477 forcing (DRF) computations have also been presented. Concerning the aerosol loading during the SOP-1a,
1478 our results indicate that numerous but moderate mineral dust plumes were observed during the campaign
1479 with main sources located in Morocco, Algeria and Tunisia, leading to AOD between 0.1 to 0.6 (at 440 nm)
1480 over the western and central Mediterranean. Analysis of synoptic situations demonstrates unfavorable
1481 conditions to produce large concentrations of polluted-smoke particles during the SOP-1a but interesting
1482 sea-spray events have been observed.

1483 Aerosol extinctions measured on-board the ATR-42 show local maxima reaching up to 150 Mm^{-1} within the
1484 dust plume, associated to extinctions of about 50 Mm^{-1} within the Marine Boundary Layer (MBL) possibly
1485 due to the presence of sea-spray aerosols. By combining ATR-42 extinction, absorption and scattering
1486 measurements, complete optical closures have been made revealing an excellent agreement in estimated
1487 optical properties. This additional information on extinction properties has allowed calculating the dust
1488 single scattering albedo (SSA) with a high level of confidence over the Western Mediterranean. Our results
1489 show a surprising moderate variability from 0.90 to 1.00 (at 530 nm) for all flights studied, corroborated by
1490 AERONET/PHOTONS SSA retrievals. The SSA derived during the ChArMEx/ADRIMED project has been also
1491 compared with referenced values obtained near dust sources, showing a relatively low difference in this
1492 optical parameter at 530 nm.

1493 Concerning the aerosol vertical structure, active remote-sensing observations, at the surface and onboard
1494 the F-20, indicate complex vertical profiles of particles with sea-spray and pollution located in the MBL, and
1495 mineral dust and/or even aged North American smoke particles located above (up to 6-7 km in altitude).
1496 Microphysical properties of aerosols measured onboard the ATR-42 and balloon-borne observations for
1497 transported/aged mineral dust reveal particle volume size distributions with diameters greater than $10 \mu\text{m}$.
1498 In most of cases, a coarse mode of mineral dust particles, characterized by an effective diameter $D_{\text{eff},c}$
1499 ranging between 5 and $10 \mu\text{m}$, has been detected within the dust layer located above the MBL. Such values
1500 are found to be larger than those referenced in dust source regions during FENNEC, SAMUM1 and AMMA,
1501 as well as measurements in the Atlantic Ocean at Cape-Verde region during SAMUM-2 and at Puerto-Rico
1502 during PRIDE.

1503 In terms of shortwave (SW) and longwave (LW) DRF, in-situ surface and aircraft observations have been
1504 merged and used as inputs in different radiative transfer codes for calculating the 1-D DRF. Modeling results
1505 show significant surface (instantaneous) SW radiative forcing down to as much as -90 W m^{-2} over super-
1506 sites. In parallel, AOD together with surface radiative fluxes observations have also been used to directly
1507 estimate the local daily surface forcing in SW (and LW) spectral regions, showing a significant effect with
1508 values of -15 W m^{-2} ($+5.5 \text{ W m}^{-2}$) over Lampedusa. Such DRF are consistent with those previously referenced
1509 over the Mediterranean basin. In parallel, aircraft observations provide also original and new estimates of

1510 SW and LW radiative heating vertical profiles with significant values of SW heating of about 5°K per day
1511 within the dust layer (for a solar angle of 30°).

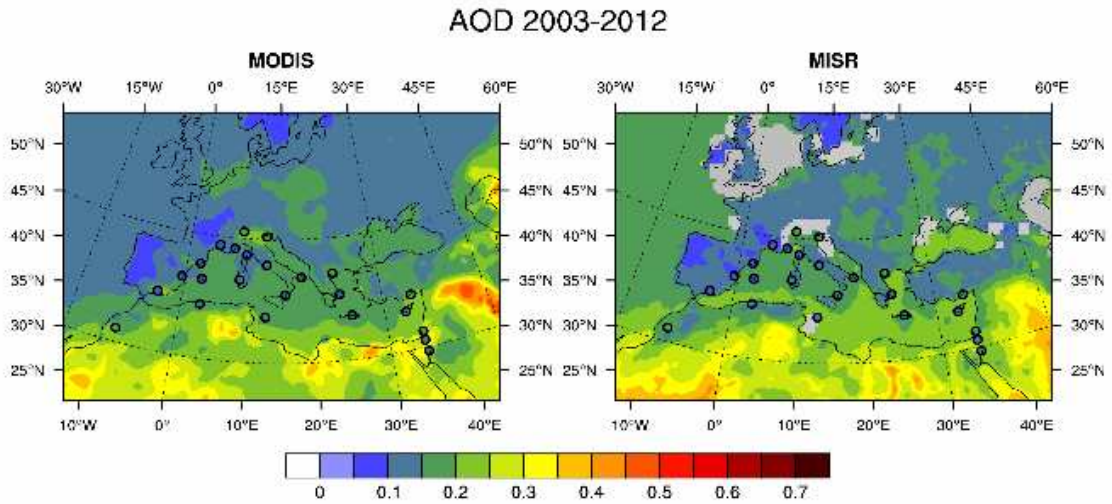
1512 Associated 3-D modeling studies, using regional climate (RCM) and chemistry transport (CTM) models,
1513 indicate a relatively good agreement between simulated AOD and that determined from
1514 AERONET/PHOTONS data. Such models allow 3-D calculations of the daily SW DRF revealing a regional DRF
1515 of -10 to -20 Wm⁻² (at the surface and in clear-sky conditions), when averaged over the SOP-1a period. At
1516 TOA, a significant dipole in the DRF is estimated between the North and the South of the domain, with
1517 positive (heating) over Northern Africa and negative (cooling) DRF over the Mediterranean basin and
1518 Europe, reflecting changes in surface albedo associated to moderately absorbing aerosols. A first multi-year
1519 simulation (conducted for the 2003 to 2009 period) that takes into account the ocean-atmosphere coupling
1520 has demonstrated that the significant aerosol radiative forcing is responsible for a decrease in sea surface
1521 temperature (on average -0.5 °C for the Mediterranean). In addition, the latent heat loss is shown to be
1522 weaker in the presence of aerosols, resulting in a decrease in specific humidity in the lower troposphere,
1523 and a reduction in cloud cover and precipitation.

1524 This unprecedented dataset of aerosol microphysical, chemical, optical properties and vertical profiles
1525 obtained over the western Mediterranean will now be used for evaluating regional models to reproduce
1526 such properties. In addition to classical model evaluations based generally on the AOD, new comparisons
1527 between models and in-situ observations on aerosol absorbing (SSA and AAOD) properties and SW and LW
1528 heating rates, which control the semi-direct effect of aerosols, should be conducted. Comparisons will also
1529 be performed on the aerosol size distribution for investigating the ability of regional models to simulate the
1530 observed large dust particle size during the transport over the Mediterranean, which could be helpful for
1531 improving the representation of deposition in such models. In parallel, in-situ observations of sea-spray
1532 particles obtained at the surface and from ATR-42 measurements will also be used to evaluate the different
1533 primary sea-spray generation schemes, in terms of concentration and size distribution. The objective is to
1534 improve the representation of microphysical and optical properties of aerosols in regional climate models
1535 which will be used in multi-year simulations to assess the impact of natural and anthropogenic aerosols on
1536 climate in this region.

1537 Acknowledgments

1538 This research has received funding from the French National Research Agency (ANR) projects ADRIMED
1539 (contract ANR-11-BS56-0006). This work is part of the ChArMEx project supported by ADEME, CEA, CNRS-
1540 INSU and Météo-France through the multidisciplinary programme MISTRALS (Mediterranean Integrated
1541 Studies at Regional And Local Scales). The station at Erba was partly supported by the CORSiCA project
1542 funded by the Collectivité Territoriale de Corse through the Fonds Européen de Développement Régional of
1543 the European Operational Program 2007-2013 and the Contrat de Plan Etat-Région. We acknowledge the
1544 AERONET/PHOTONS sun-photometer networks and the PIs of the selected stations and their staff for their
1545 work to produce the dataset used in this study. The financial support for EARLINET in the ACTRIS Research
1546 Infrastructure Project by the European Union's Horizon 2020 research and innovation programme under
1547 grant agreement n. 654169 and previously under grant agreement n. 262254 in the 7th Framework
1548 Programme (FP7/2007-2013) is gratefully acknowledged. In particular, the authors are thankful to the
1549 Italian EARLINET PIs (Maria Rita Perrone, Lecce; Nicola Spinelli, Naples; Gelsomina Pappalardo, Potenza;
1550 Simona Scollo, Serra La Nave) and their staff. Measurements at Lampedusa by ENEA were partly supported
1551 by the Italian Ministry for University and Research through the NextData and Ritmare Projects. This study,
1552 especially the balloon campaign and part of the aircraft operations has also been supported by the French
1553 space agency (CNES). The technical staff of SAFIRE, INSU Technical Division and the CNES Balloon sub-
1554 directorate (with special mention to Aurélien Bourdon and Gilles Dupouy) are warmly acknowledged for
1555 their contribution to the success of the experimental work. Contributions by Didier Bruneau (Latmos), Silvia
1556 Becagli (Univ. of Florence, Italy), Marco Cacciani (Univ. of Rome, Italy), Julian Groebner and Natalia
1557 Kouremeti (Physikalisch-Meteorologisches Observatorium Davos, World Radiation Center, Switzerland), and
1558 José Antonio Martínez Lozano (University of Valencia, Spain) are gratefully acknowledged. Barcelona station
1559 was partially supported by the Spanish Ministry of Economy and Competitiveness (project TEC2012-34575) and
1560 of Science and Innovation (project UNPC10-4E-442) and FEDER funds, and by the Department of Economy
1561 and Knowledge of the Catalan Autonomous Government (grant 2014 SGR 583). Granada station was
1562 partially supported by the Andalusian Regional Government through project P12-RNM-2409 and by the
1563 Spanish Ministry of Science and Technology through project CGL2013-45410-R. Sahar Hassazadeh,
1564 Constantino Muñoz-Porcar, Santi Bertolín and Diego Lange are also acknowledged for their kind assistance
1565 in operating the Menorca surface station, as well as François Gheusi, Brice Barret, Flore Tocquer, and Yves
1566 Meyerfeld for their contribution to the balloon campaign preparation and/or deployment. Claude
1567 Basdevant, Alexis Doerenbecher, and Fabien Bernard are acknowledged for their help and very useful tools
1568 in support of our drifting balloon experiment. The Granada station was partially supported by the
1569 Andalusian Regional Government through project P12-RNM-2409 and by the Spanish Ministry of Science
1570 and Technology through project CGL2013-45410-R.

1571
1572
1573
1574
1575
1576
1577
1578
1579
1580
1581
1582
1583
1584
1585
1586
1587
1588
1589



1592 **Figure 1.** Aerosol Optical Depth (at 550 nm) derived from MODIS and MISR satellites for the 2003 to 2012 period. The
1593 AERONET/PHOTONS AOD are also indicated.
1594
1595
1596
1597
1598
1599
1600
1601
1602
1603
1604
1605
1606
1607
1608
1609
1610
1611
1612
1613
1614
1615
1616
1617
1618
1619

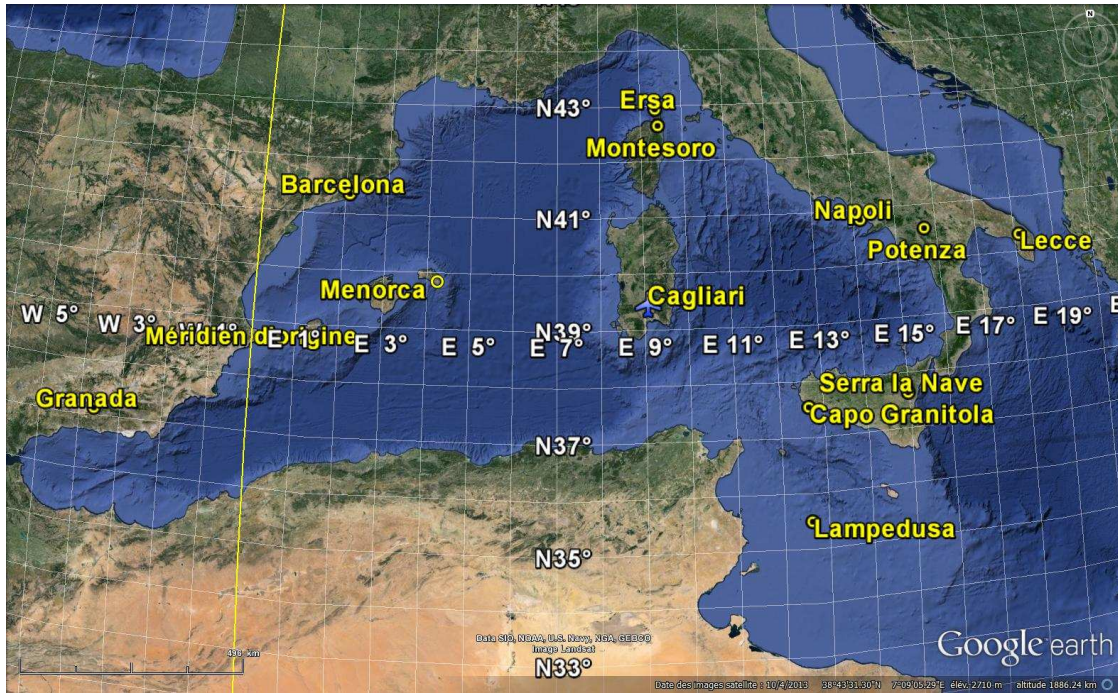


Figure 2. The regional experimental set-up deployed in the western and central Mediterranean during the campaign ChArMEx SOP-1a. The two aircrafts were based at Cagliari.

1620
 1621
 1622
 1623
 1624
 1625
 1626
 1627
 1628
 1629
 1630
 1631
 1632
 1633
 1634
 1635
 1636
 1637
 1638
 1639
 1640
 1641
 1642
 1643
 1644
 1645
 1646
 1647
 1648
 1649
 1650
 1651
 1652
 1653
 1654
 1655
 1656
 1657
 1658

ADRIDMED flights - ATR42 & Falcon20 - JUNE & JULY 2013

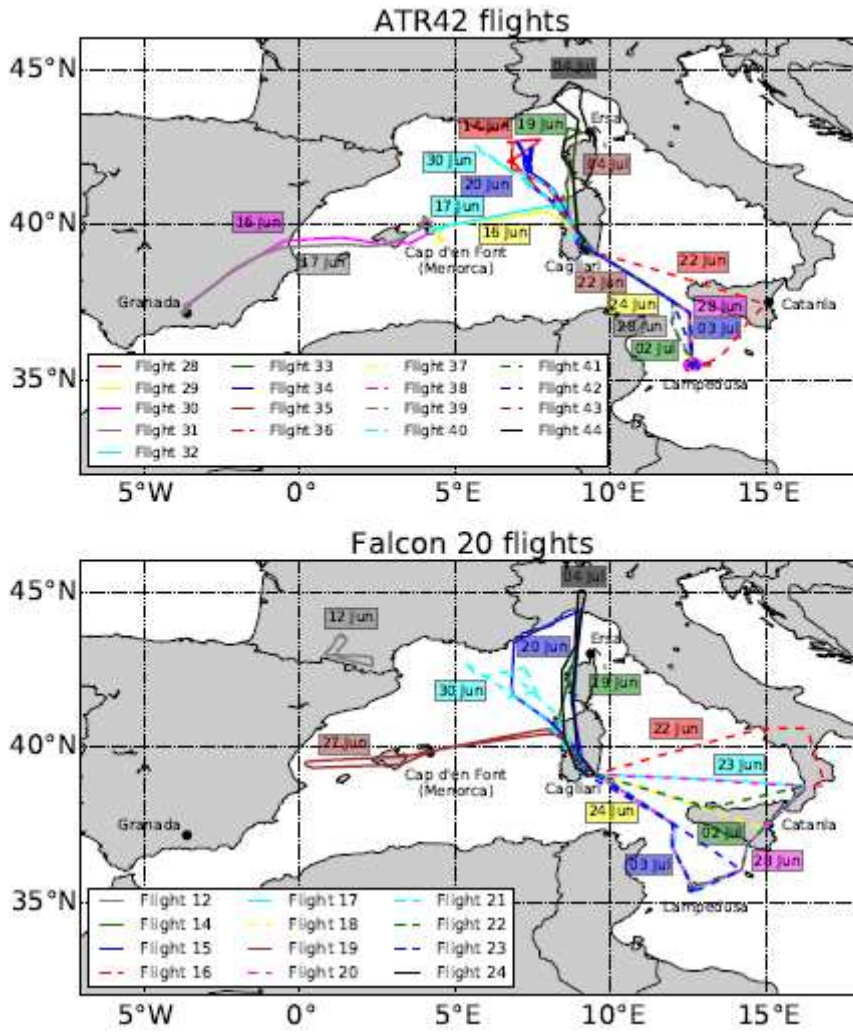


Figure 3. Overview of the different ATR-42 and F-20 flight trajectories performed during the SOP-1a experiment.

1659
1660
1661
1662
1663
1664
1665
1666
1667
1668
1669
1670
1671
1672
1673
1674
1675
1676
1677
1678
1679
1680
1681
1682
1683

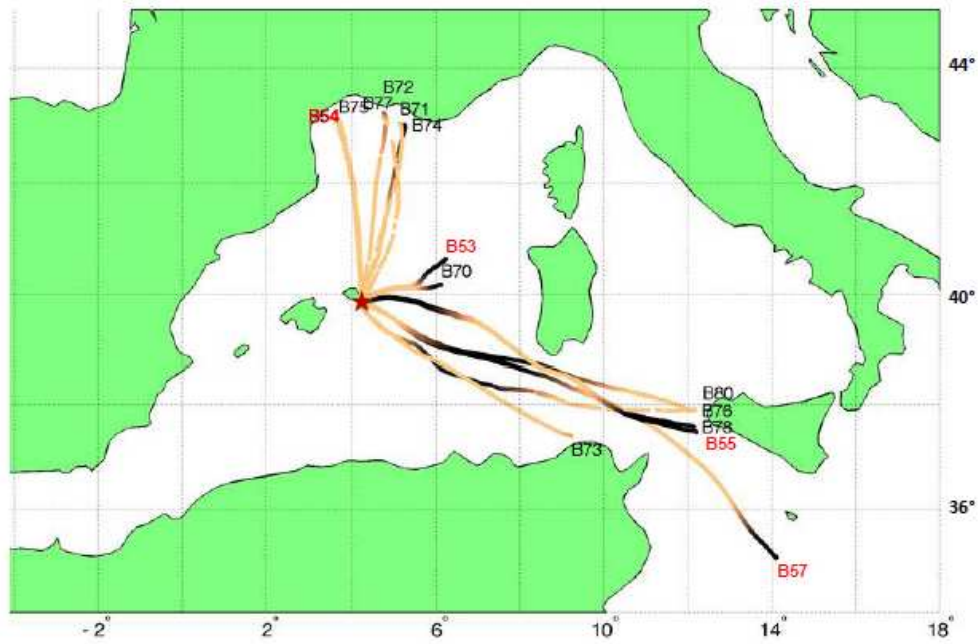


Figure 4. Trajectories of the 14 BPCL drifting balloons launched from Minorca Island during the campaign. Dark portion along trajectories correspond to night-time conditions. The four red labels from B54 to B57 indicate balloons with an ozone sonde and the 10 others carried a LOAC instrument.

1684
 1685
 1686
 1687
 1688
 1689
 1690
 1691
 1692
 1693
 1694
 1695
 1696
 1697
 1698
 1699
 1700
 1701
 1702
 1703
 1704
 1705
 1706
 1707
 1708
 1709
 1710
 1711
 1712
 1713
 1714
 1715
 1716
 1717
 1718
 1719
 1720

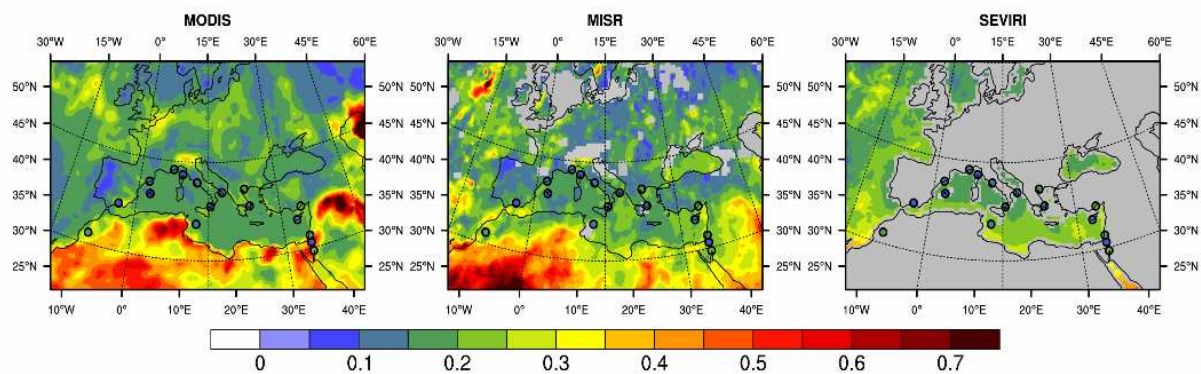
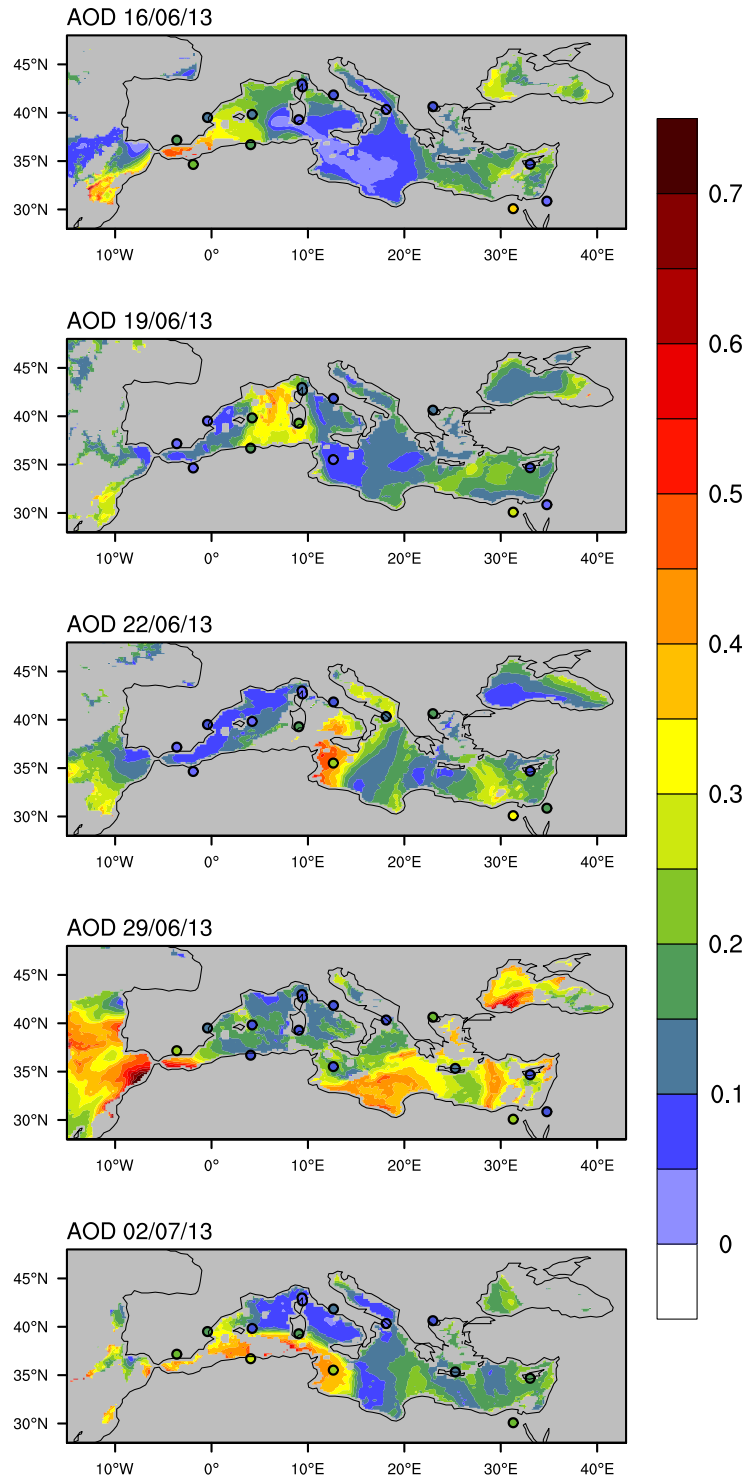


Figure 5. Total AOD (500 nm) obtained from the MODIS, MISR and SEVIRI (sea only) sensors for the June-July 2013 period. The AERONET/PHOTONS AOD are also indicated.

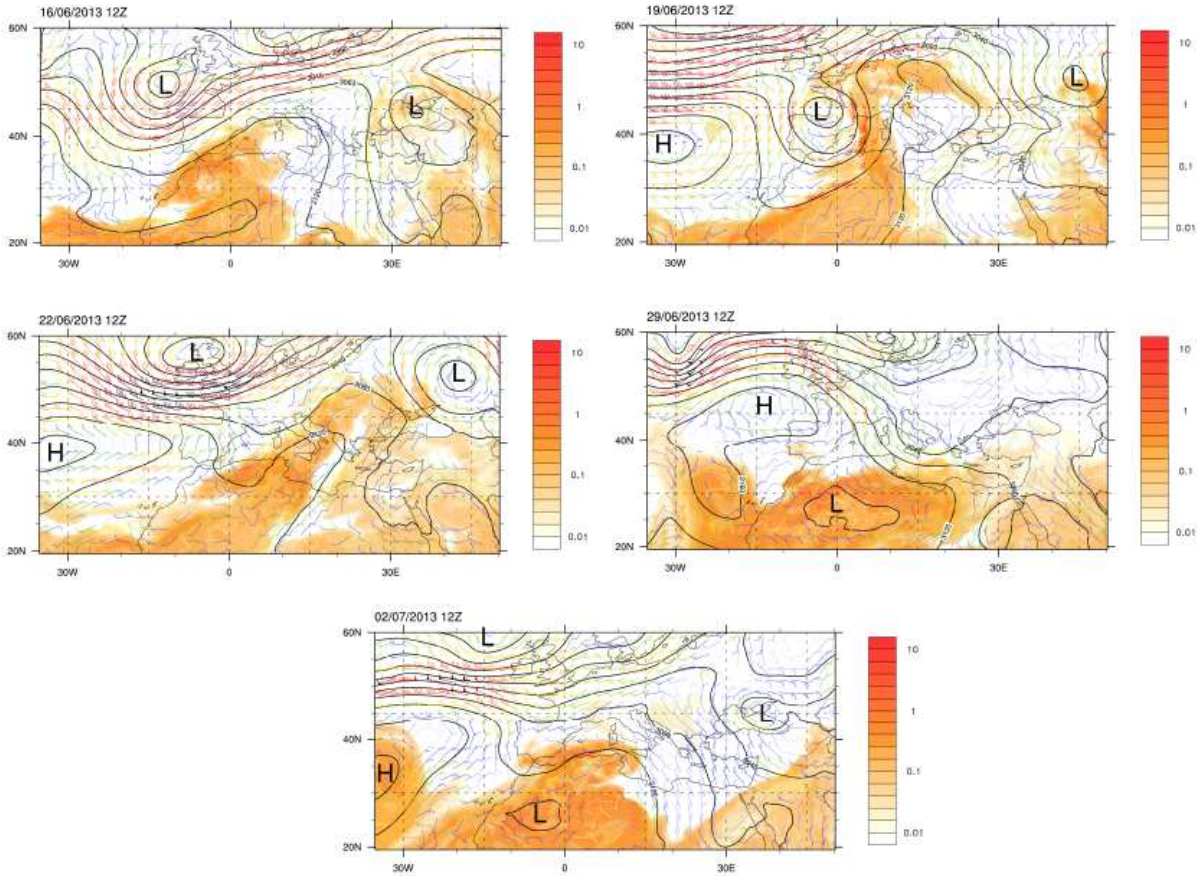
1721
 1722
 1723
 1724
 1725
 1726
 1727
 1728
 1729
 1730
 1731
 1732
 1733
 1734
 1735
 1736
 1737
 1738
 1739
 1740
 1741
 1742
 1743
 1744
 1745
 1746
 1747
 1748
 1749
 1750
 1751
 1752
 1753
 1754
 1755
 1756
 1757
 1758
 1759
 1760



1762
 1763
 1764
 1765
 1766
 1767
 1768
 1769
 1770
 1771
 1772
 1773
 1774

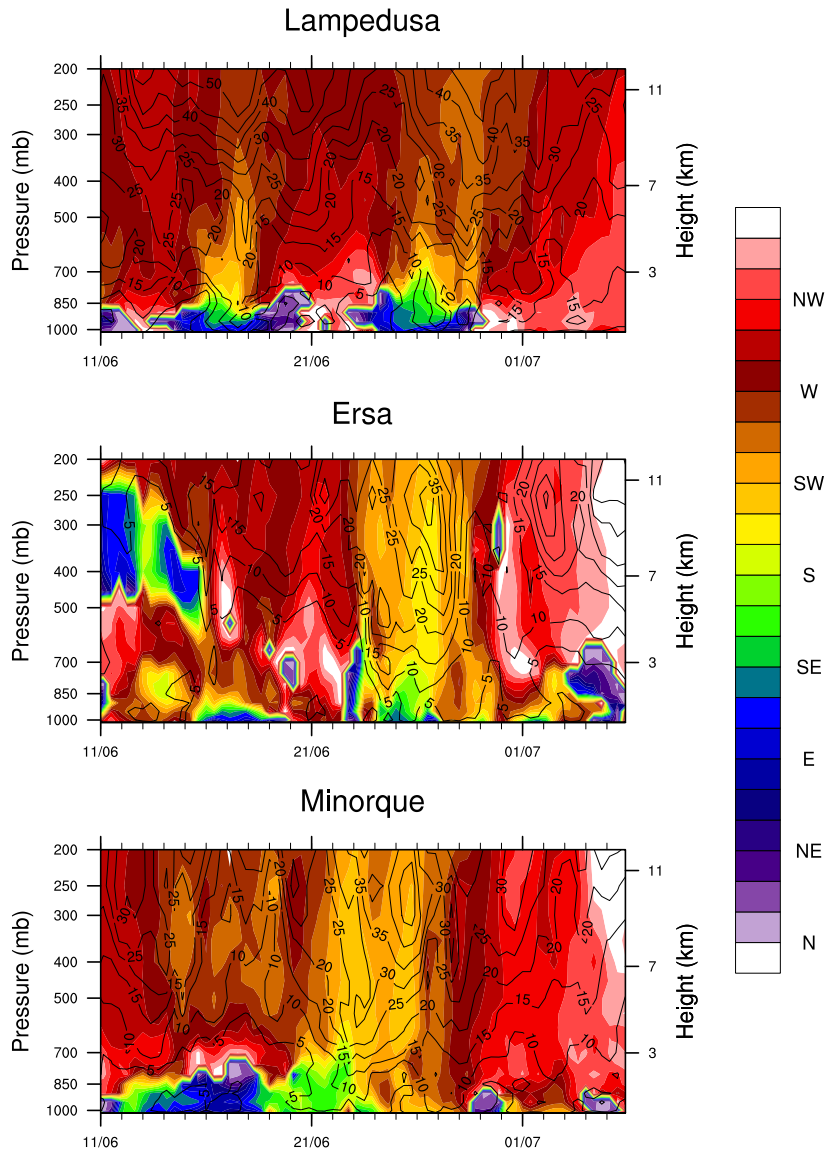
Figure 6. AOD MSG/SEVIRI observations for five different days during the SOP-1a experiment (16/06, 19/06, 22/06, 29/06 and 03/07). The AERONET/PHOTONS AOD are also indicated.

1775



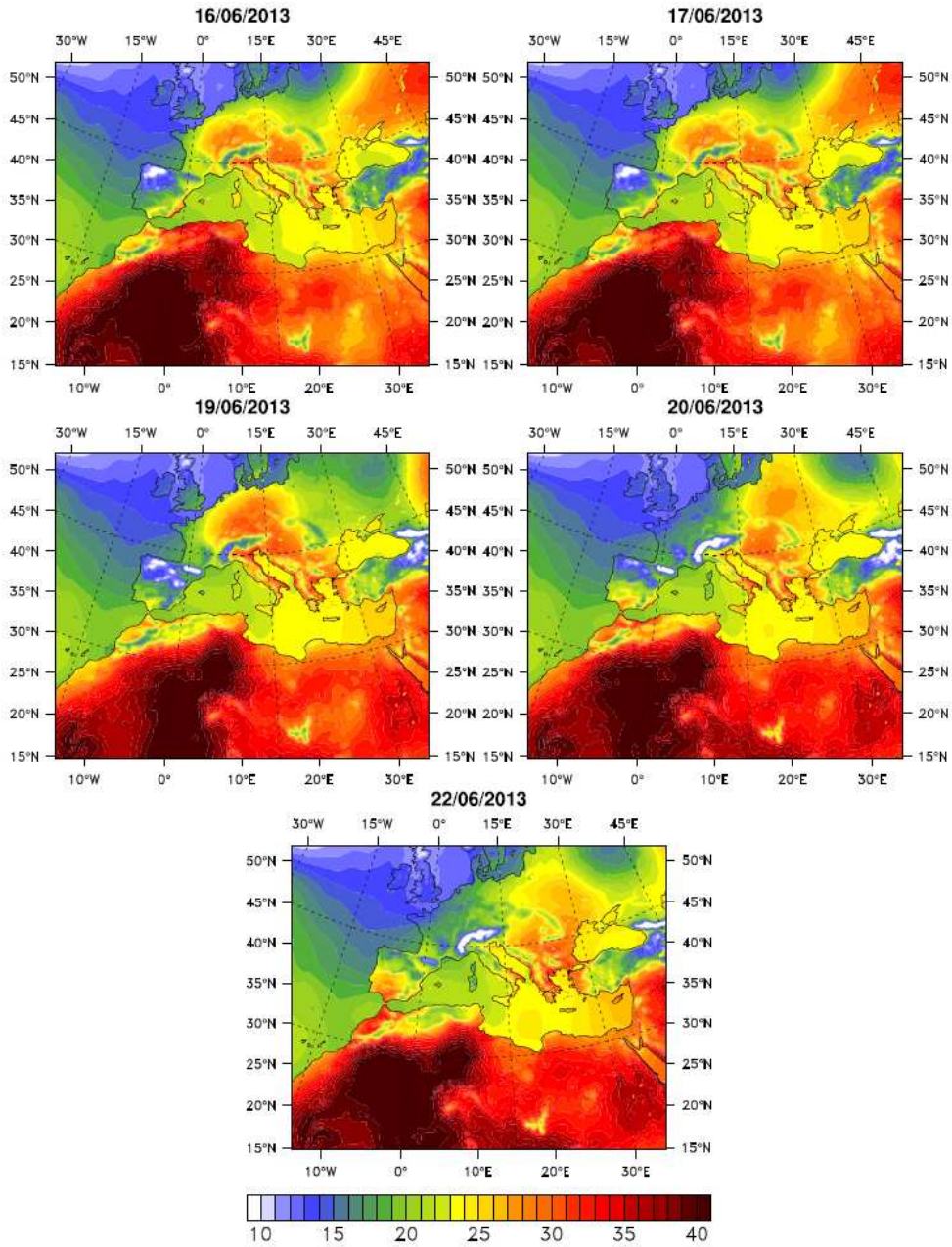
1776
1777
1778
1779
1780
1781
1782
1783
1784
1785
1786
1787
1788
1789
1790
1791
1792
1793
1794
1795
1796
1797
1798
1799
1800
1801
1802
1803
1804
1805
1806
1807

Figure 7. Geopotential at 700 hPa, mass dust concentration (in mg.m⁻³), and wind intensity at 700 hPa for the 06, 19, 22, 29 of June and 02 of July at 12:00 UTC, simulated from the ALADIN model.



1809
 1810
 1811
 1812
 1813
 1814
 1815
 1816
 1817
 1818
 1819
 1820
 1821
 1822
 1823
 1824
 1825
 1826
 1827
 1828
 1829
 1830
 1831

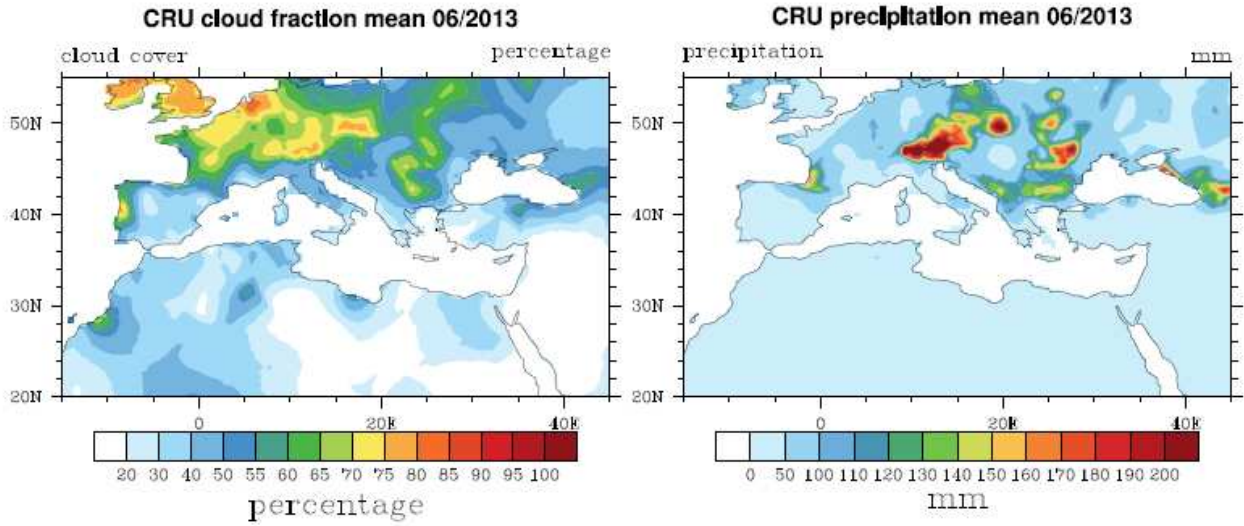
Figure 8. Wind profiles between 1000 and 200 hPa during the SOP-1a experiment for three different sites (Ersa, Lampedusa and Minorca) simulated from the ALADIN model. The wind intensity (in $m s^{-1}$) is also reported at the differents stations.



1833
1834
1835
1836
1837
1838
1839
1840
1841
1842
1843
1844
1845
1846
1847
1848
1849
1850
1851

Figure 9. Surface Temperature (at 12:00 UTC) obtained from NCEP re-analysis for the 16, 17, 19, 20 and 22 of June.

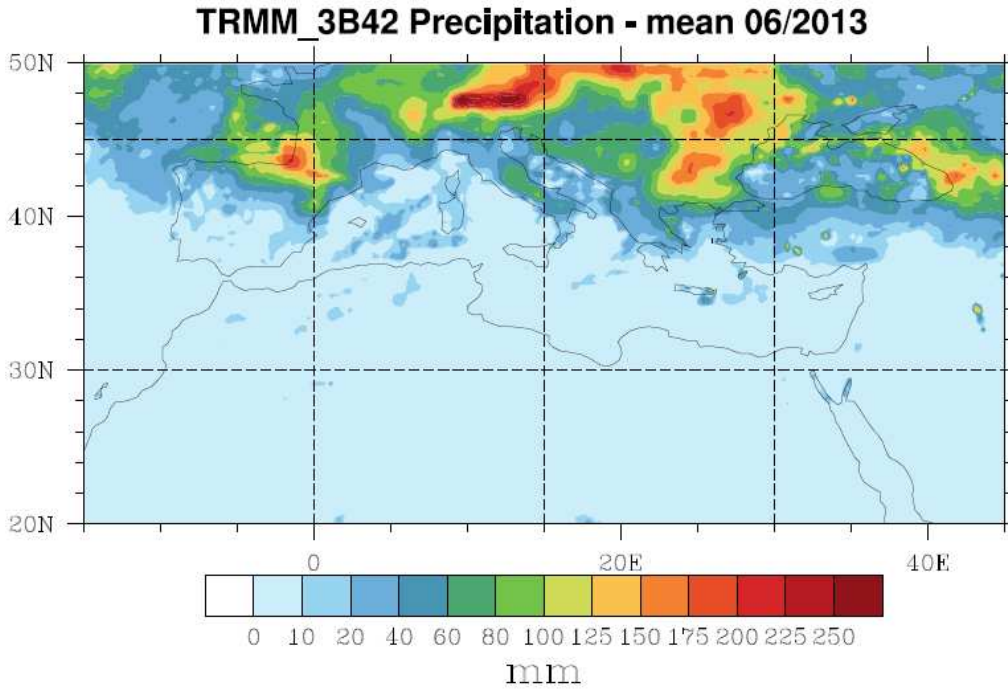
1852



1853
1854
1855
1856
1857
1858
1859
1860
1861
1862
1863
1864
1865
1866
1867
1868
1869
1870
1871
1872
1873
1874
1875
1876
1877
1878
1879
1880
1881
1882
1883
1884
1885
1886
1887
1888
1889
1890
1891
1892
1893

Figure 10. Monthly cloud cover and precipitation (over land only) derived from the Climate Research Unit (CRU) data for June 2013.

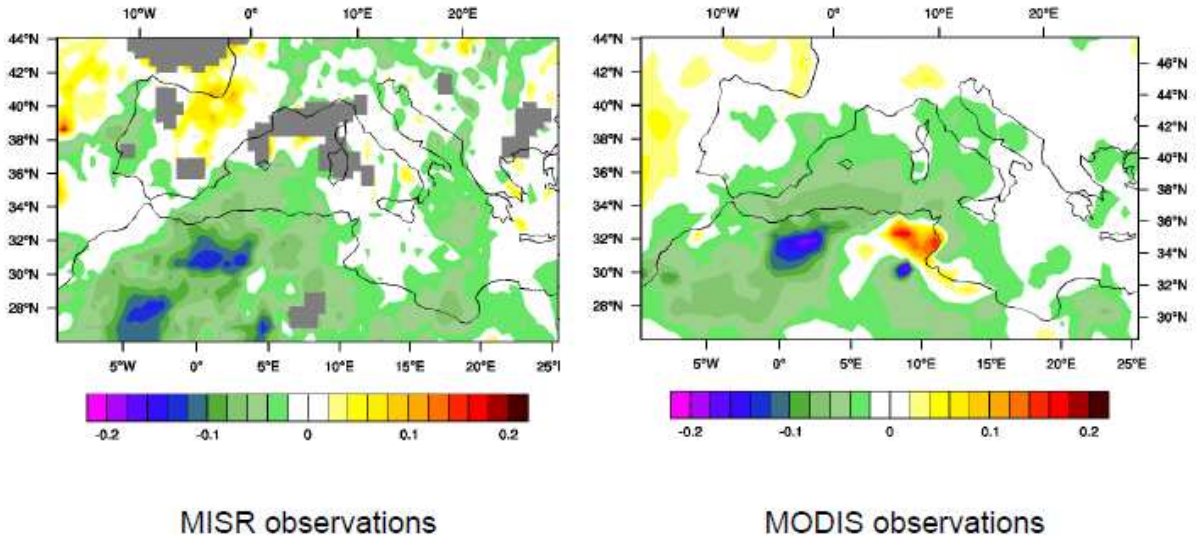
1894



1895
1896
1897
1898
1899
1900
1901
1902
1903
1904
1905
1906
1907
1908
1909
1910
1911
1912
1913
1914
1915
1916
1917
1918
1919
1920
1921
1922
1923
1924
1925
1926
1927
1928
1929
1930

Figure 11. Same figure as 10 but for the Tropical Rainfall Measuring Mission (TRMM) precipitation observations.

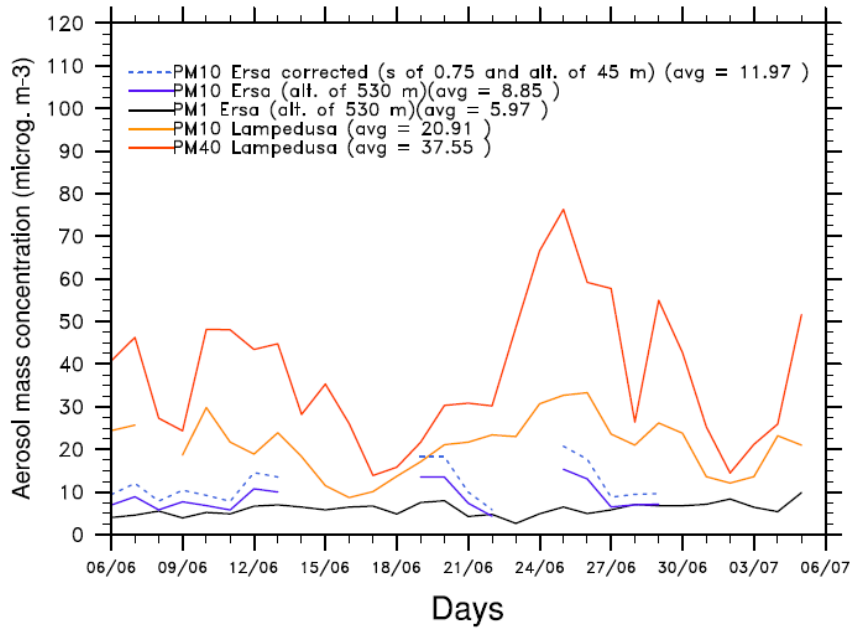
1931



1932
1933
1934
1935
1936
1937
1938
1939
1940
1941
1942
1943
1944
1945
1946
1947
1948
1949
1950
1951
1952
1953
1954
1955
1956
1957
1958
1959
1960
1961
1962
1963
1964
1965
1966
1967
1968
1969
1970
1971

Figure 12. AOD anomaly for summer 2013 estimated from the MODIS and MISR sensor data.

1972



1973
1974
1975
1976
1977
1978
1979
1980
1981
1982
1983
1984
1985
1986
1987
1988
1989
1990
1991
1992
1993
1994
1995
1996
1997
1998
1999
2000
2001
2002
2003
2004
2005
2006
2007
2008
2009

Figure 13. Time-series of daily PM mass concentrations estimated at the Lampedusa (PM40 and PM10) and Ersu (PM1 and PM10) super-stations. Problems in PM10 data acquisition that occurred at Ersu explain the gaps. “PM10 Ersu corrected” curve correspond to PM10 estimated at an altitude of 45m to be comparable with Lampedusa results, following the logarithmic law provided by Piazzola et al. (2015), (see text in section 5.1.1 for details).

SOP-1a AERONET/PHOTONS Volume size distribution

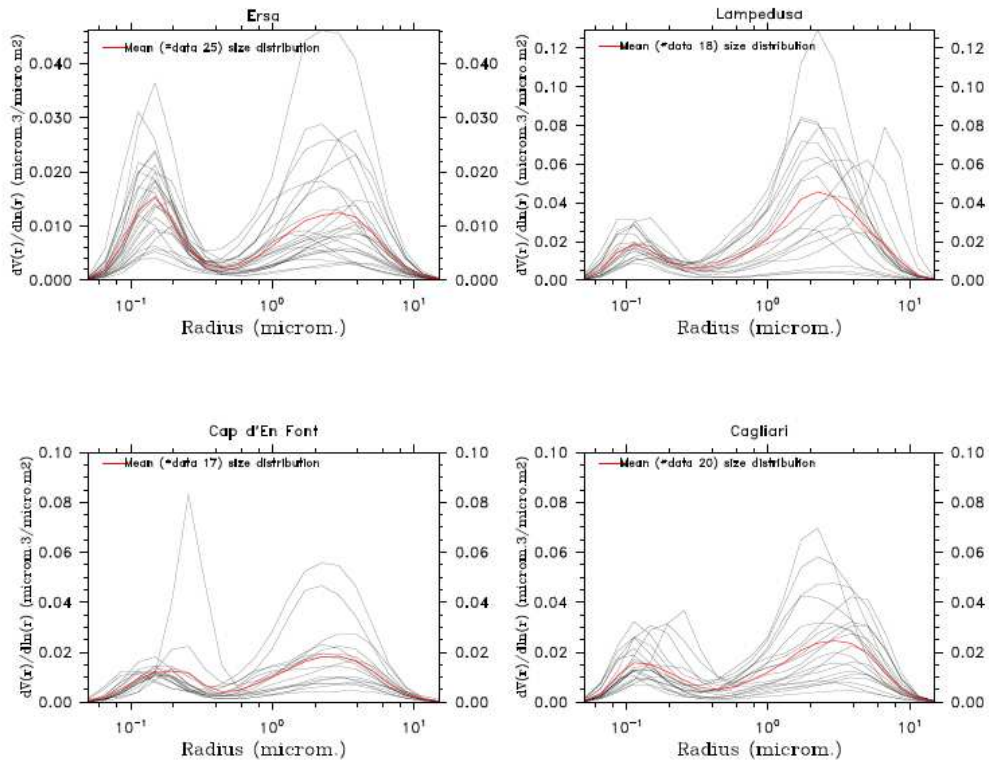
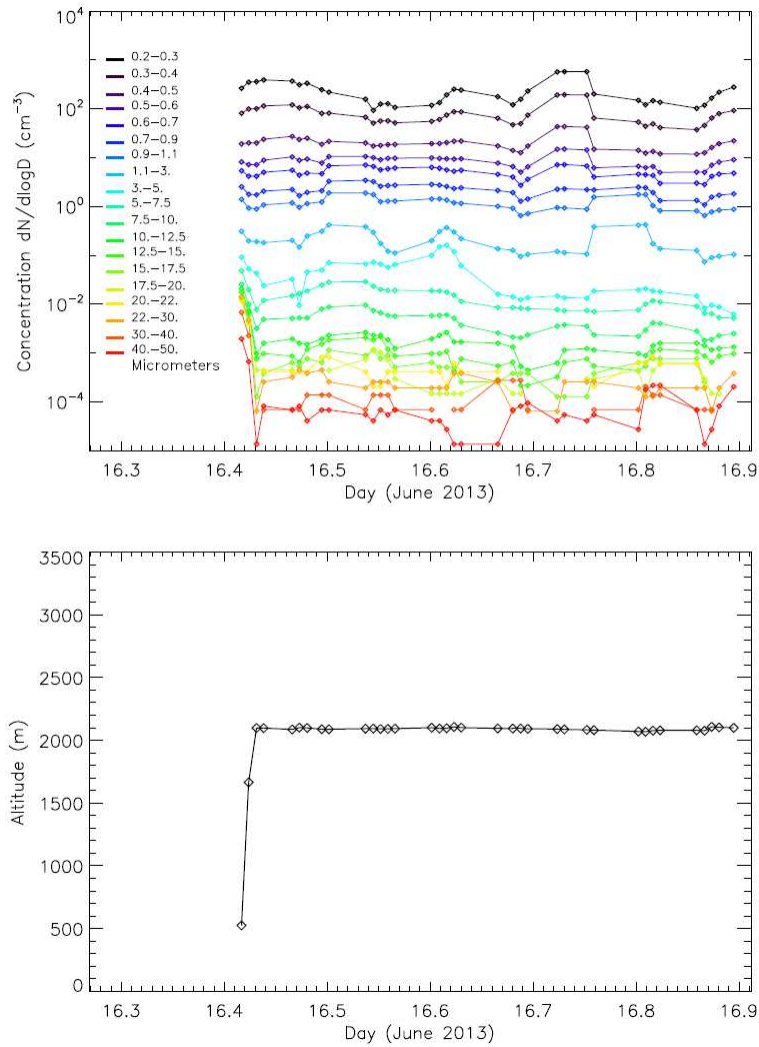


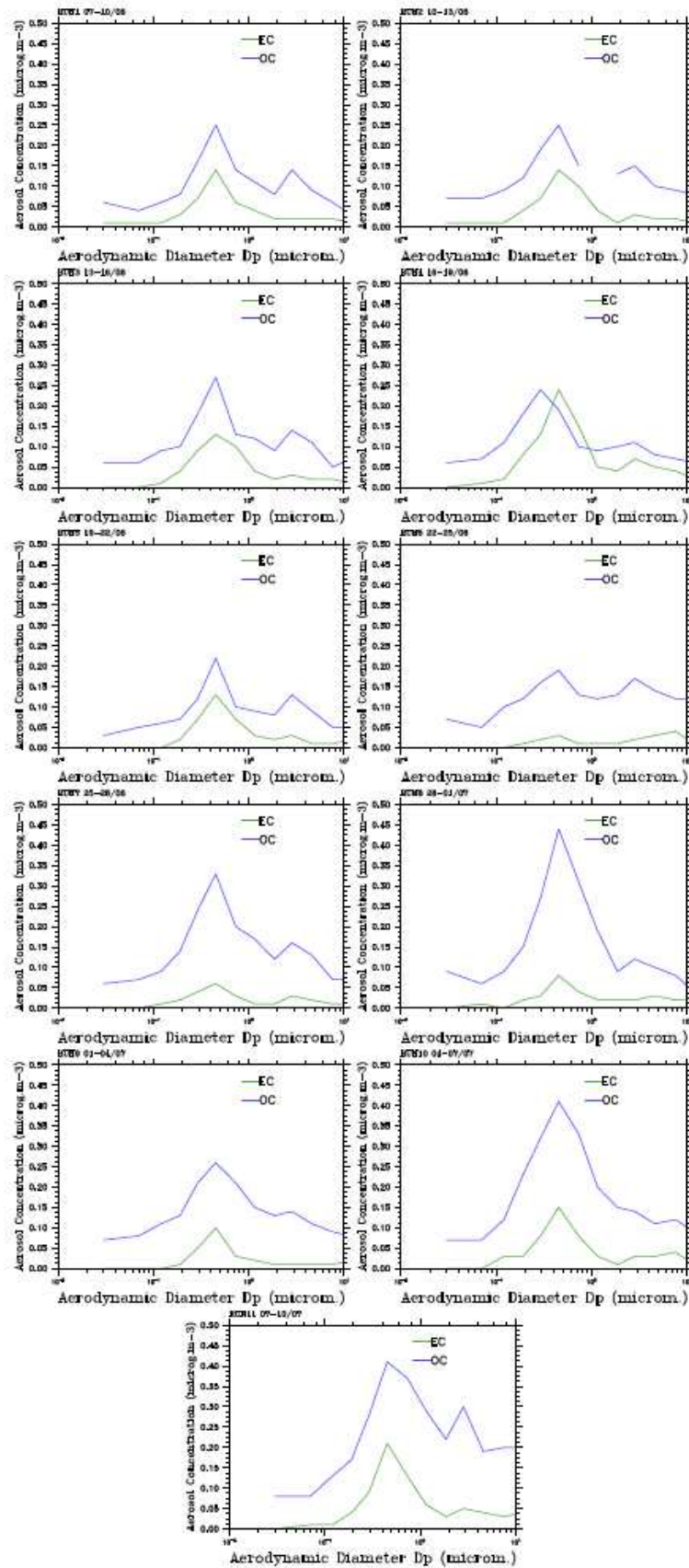
Figure 14. AERONET/PHOTONS volume size distribution derived at four different stations: Ersa, Lampedusa, Cagliari and Cap d'En Font (the red curve represents the mean of observations). The characteristics of the volume size distribution are provided in Table 6.

2010
2011
2012
2013
2014
2015
2016
2017
2018
2019
2020
2021
2022
2023
2024
2025
2026
2027
2028
2029
2030
2031
2032
2033
2034
2035
2036
2037



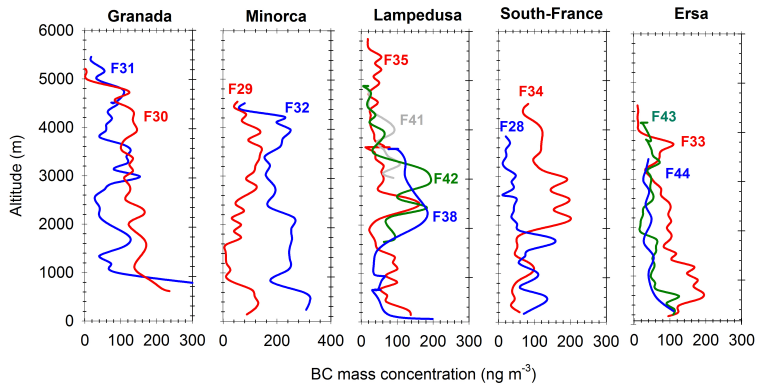
2038
 2039
 2040
 2041
 2042
 2043
 2044
 2045
 2046
 2047
 2048
 2049
 2050
 2051
 2052
 2053
 2054
 2055
 2056

Figure 15. Particle size distribution measured with a LOAC during the ~12-h flight of the BPCL balloon B74 drifting from Minorca Island towards Marseille (see trajectory in Figure 4). The first and last 20 min correspond to the ascending and descending phases of the quasi-Lagrangian flight which occurred at a constant altitude of 2091±10 m.



2057
 2058
 2059
 2060
 2061
 2062

Figure 16. EC and OC (48h-mean) aerosol mass size distributions obtained at Ersa from the impactor DEKATI instrument for all the SOP-1a period.



2063
2064
2065

Figure 17. Vertical profiles of rBC concentrations estimated from SP2 instrument for 5 different zones (Granada, Minorca, Lampedusa, South-France and Ersa).

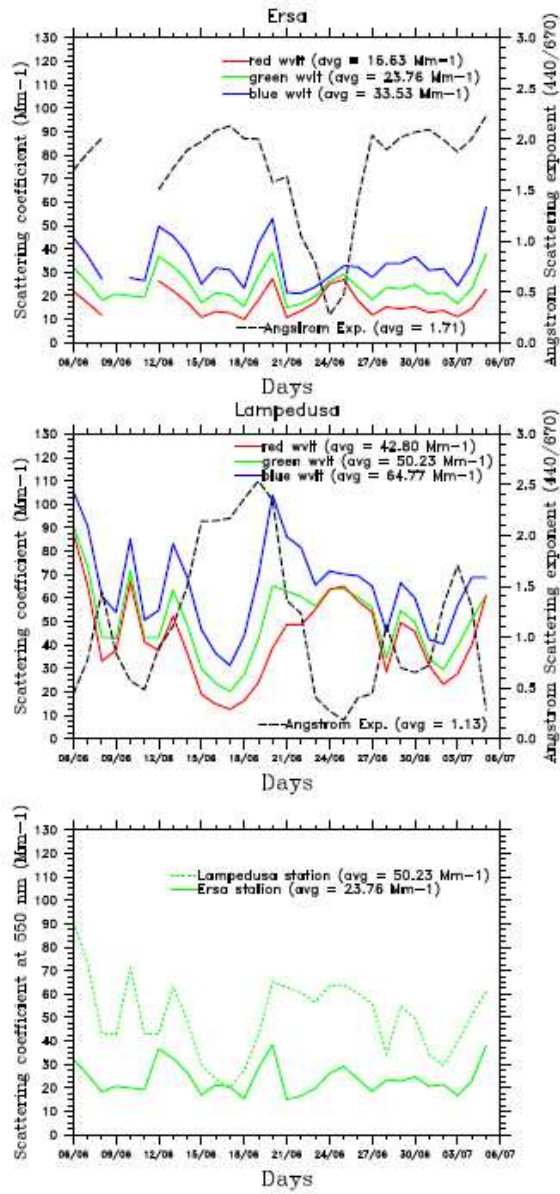


Figure 18. Time-series of daily scattering coefficient (in Mm^{-1}) estimated in the Ersa and Lampedusa stations. The daily Angström Exponent (AE), calculated between 440 and 670 nm, is also reported.

2066
 2067
 2068
 2069
 2070
 2071
 2072
 2073
 2074
 2075
 2076
 2077
 2078
 2079
 2080
 2081
 2082
 2083
 2084
 2085
 2086

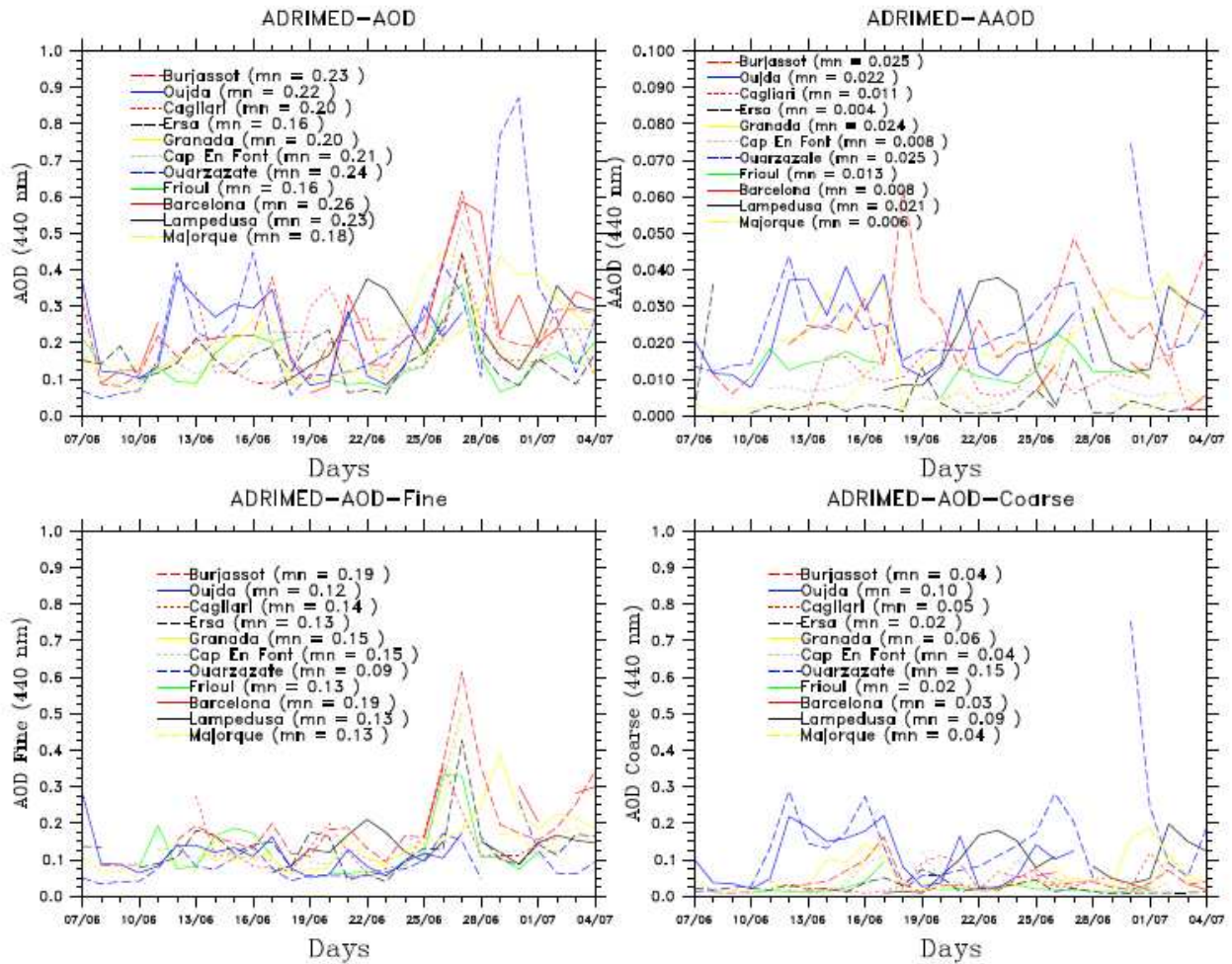
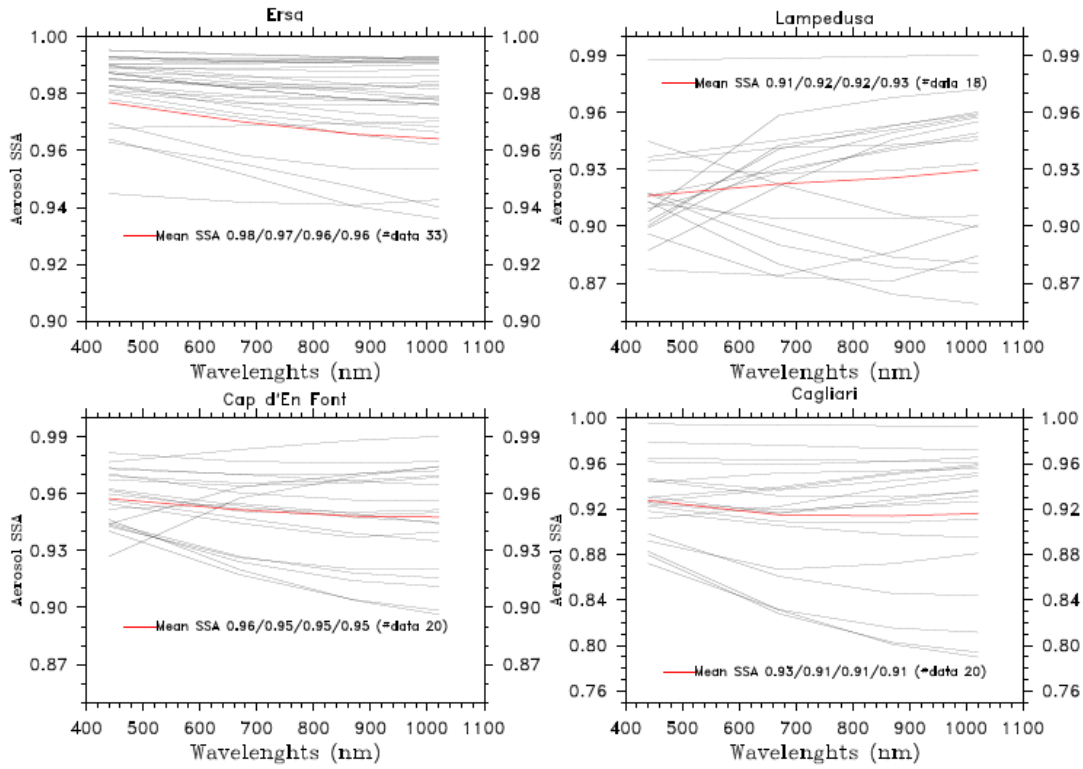


Figure 19. AERONET/PHOTONS observations of the total extinction AOD, AOD Fine (AODf), AOD Coarse (AODc) and Absorbing AOD (AAOD), at 440 nm obtained for the whole SOP-1a period.

2087
2088
2089
2090
2091
2092
2093
2094
2095
2096
2097
2098
2099
2100
2101
2102
2103
2104
2105
2106
2107
2108
2109
2110
2111
2112
2113
2114

SOP-1a AERONET/PHOTONS SSA



2115
 2116
 2117
 2118
 2119
 2120
 2121
 2122
 2123
 2124
 2125
 2126
 2127
 2128
 2129
 2130
 2131
 2132
 2133
 2134
 2135
 2136
 2137
 2138
 2139
 2140
 2141
 2142
 2143
 2144
 2145

Figure 20. AERONET/PHOTONS observations of the total single scattering albedo (SSA) at 440, 670, 880 and 1020 nm obtained for the whole SOP-1a period (the red curve represents the mean of observations).

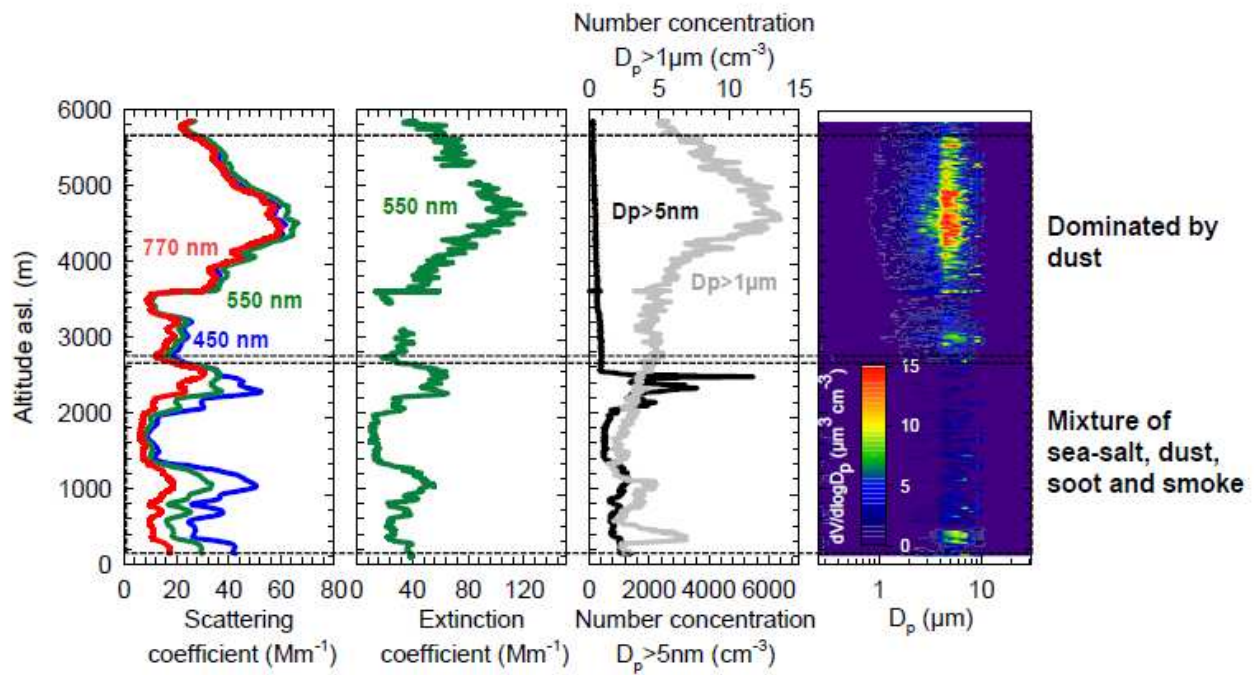


Figure 21. Optical (scattering and extinction coefficients) and physical (number concentration and volume size distribution) aerosol properties estimated along the vertical onboard the ATR-42 aircraft for the flights 35-36 on 22 June over the Lampedusa station.

2146
 2147
 2148
 2149
 2150
 2151
 2152
 2153
 2154
 2155
 2156
 2157
 2158
 2159
 2160
 2161
 2162
 2163
 2164
 2165
 2166
 2167
 2168
 2169
 2170
 2171
 2172
 2173
 2174
 2175
 2176
 2177
 2178
 2179
 2180
 2181

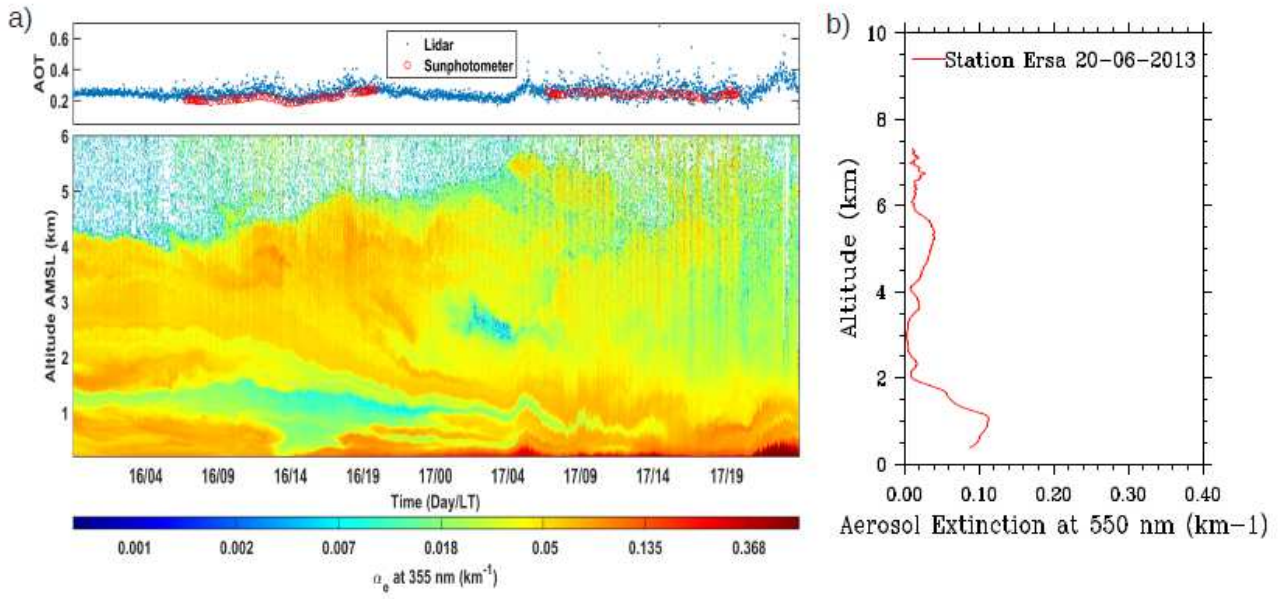


Figure 22. Minorca and Ersa lidar observations obtained during the dust plume of 16 to 17 June transported over the western Mediterranean basin.

2182
 2183
 2184
 2185
 2186
 2187
 2188
 2189
 2190
 2191
 2192
 2193
 2194
 2195
 2196
 2197
 2198
 2199
 2200
 2201
 2202
 2203
 2204
 2205
 2206
 2207
 2208
 2209
 2210
 2211
 2212
 2213
 2214
 2215
 2216
 2217
 2218
 2219
 2220
 2221

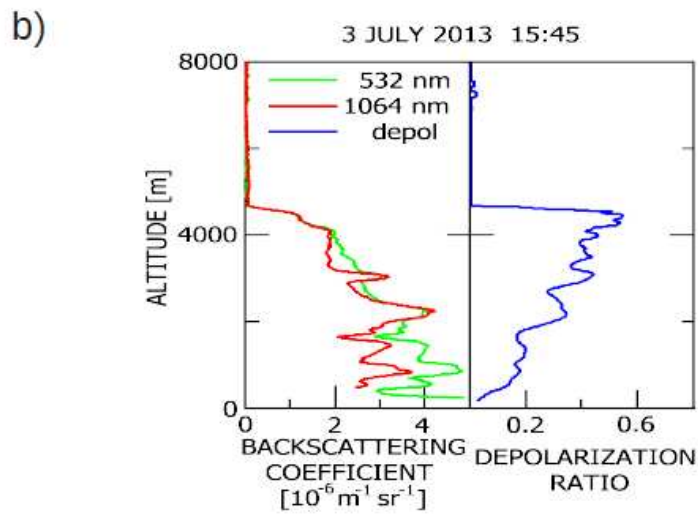
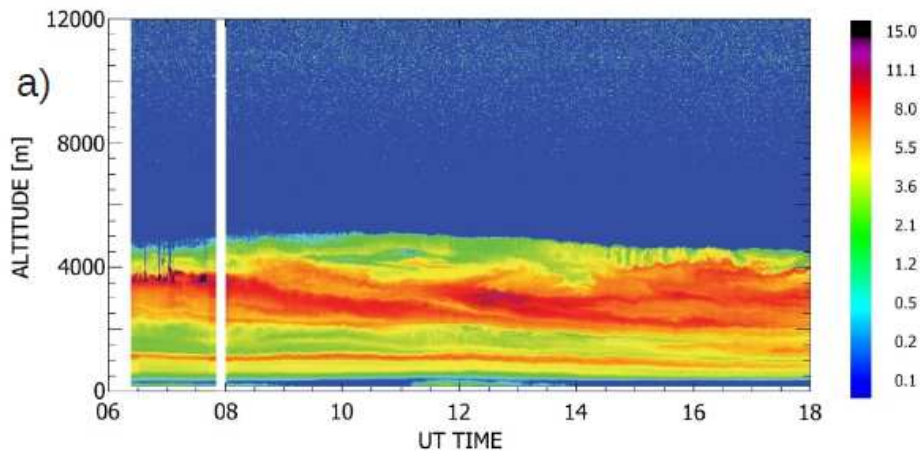
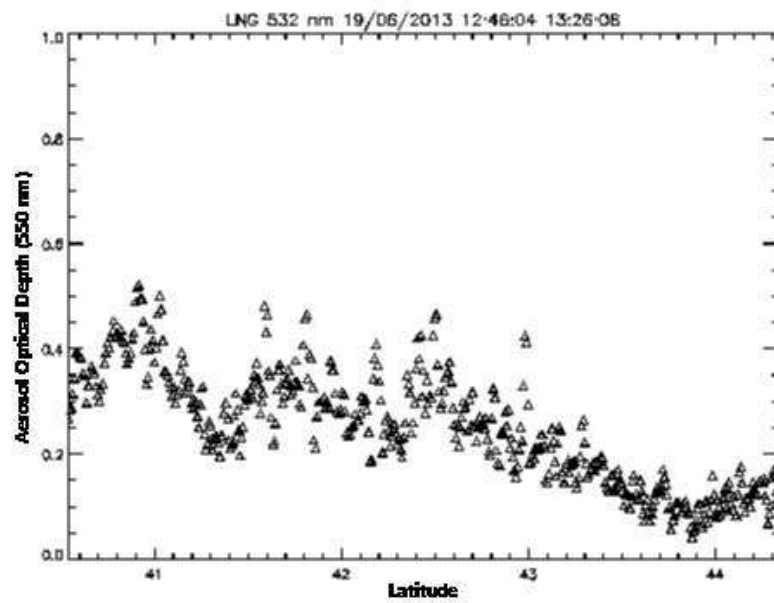
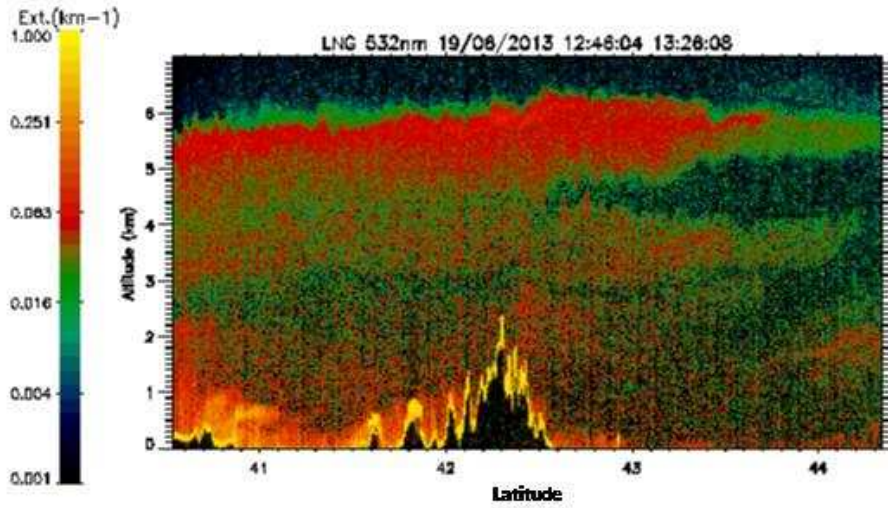


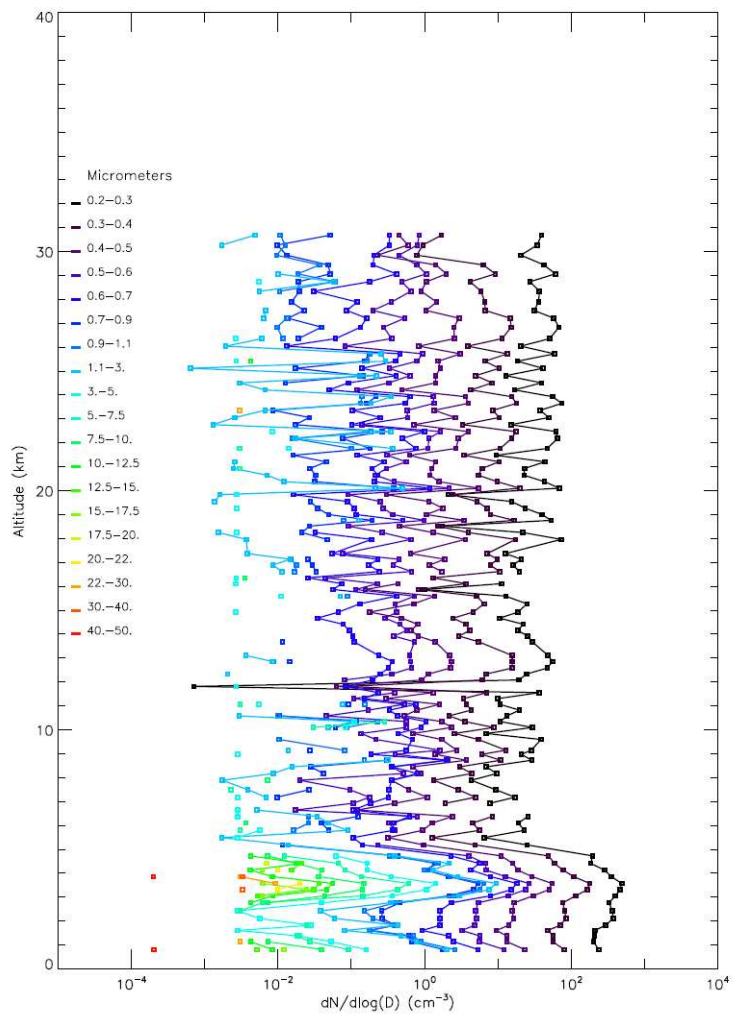
Figure 23. a) Time evolution of the vertical profile of the aerosol backscattering coefficient at 1064 nm at Lampedusa on 3 July 2013. The color scale is in units of $10^{-7} \text{ m}^{-1} \text{ sr}^{-1}$. b) Vertical profile of aerosol backscattering coefficient at two wavelengths and of aerosol depolarization ratio at 355 nm measured at Lampedusa on 3 July 2013 at 15:45 UT.

2222
 2223
 2224
 2225
 2226
 2227
 2228
 2229
 2230
 2231
 2232
 2233
 2234
 2235
 2236
 2237
 2238
 2239
 2240
 2241
 2242
 2243
 2244
 2245
 2246
 2247



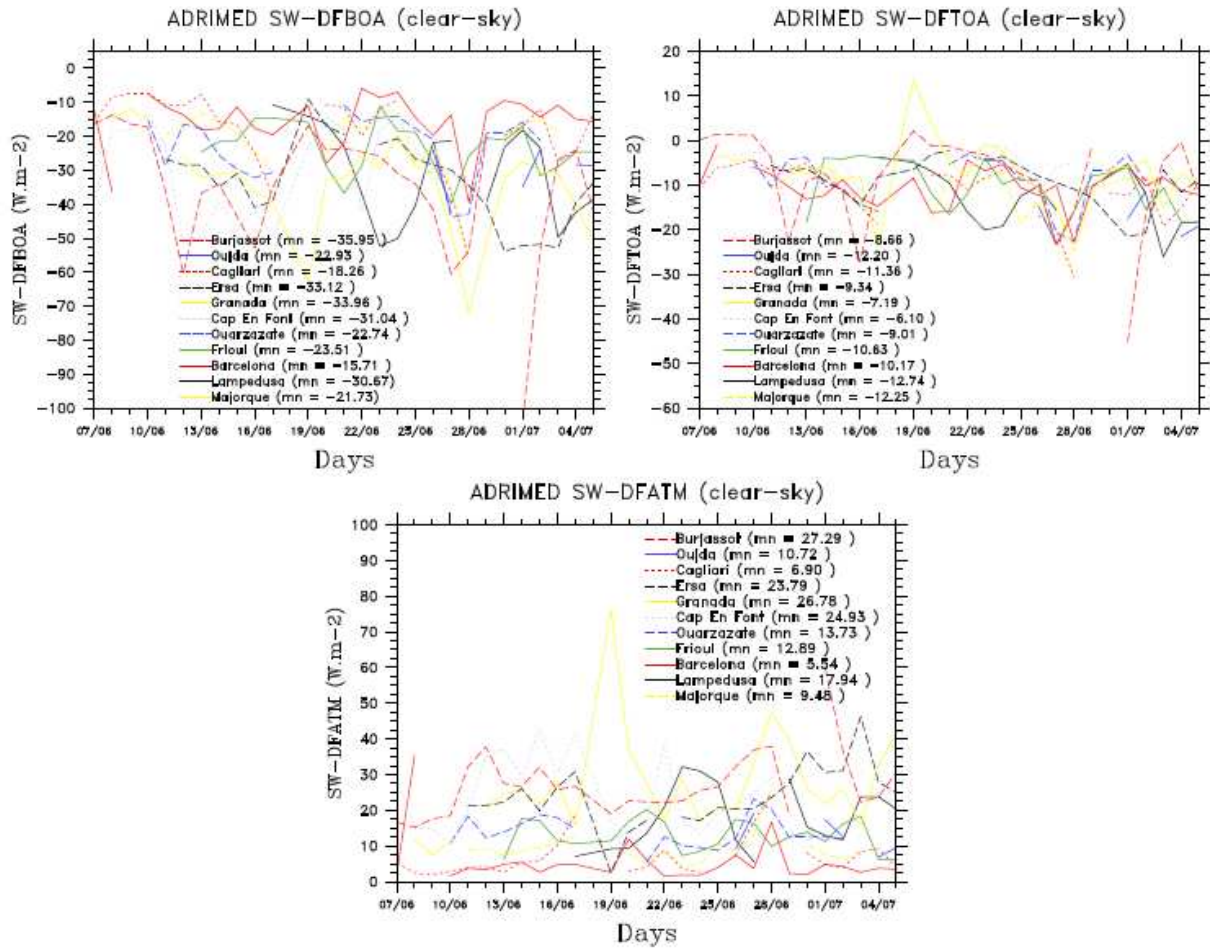
2248
 2249
 2250
 2251
 2252
 2253
 2254
 2255
 2256
 2257
 2258
 2259
 2260
 2261
 2262
 2263
 2264
 2265
 2266
 2267
 2268
 2269

Figure 24. Observations of aerosol extinction coefficient (top, in km^{-1} at 532 nm) and aerosol optical depth (bottom) obtained from the lidar LNG system onboard the F-20 aircraft during the 19th of June that corresponds to the flight (12:46 to 13:26) from Cagliari to the Gulf of Genoa.



2270
 2271
 2272
 2273
 2274
 2275
 2276
 2277
 2278
 2279
 2280
 2281
 2282
 2283
 2284
 2285
 2286
 2287
 2288

Figure 25: Particle concentrations as a function of size and altitude in the troposphere and lower stratosphere from the LOAC flight under the meteorological balloon BLD9 launched from Minorca at the end of a dust event on 19 June 2013, 10:12 UT (Table 4; see the daytime averaged aerosol optical depth over the sea in Figure 6).



2289
 2290
 2291
 2292
 2293
 2294
 2295
 2296
 2297
 2298
 2299
 2300
 2301
 2302
 2303
 2304
 2305
 2306
 2307
 2308
 2309
 2310
 2311
 2312
 2313
 2314

Figure 26. 1-D (clear-sky) instantaneous (shortwave only) DRF calculations (in $W m^{-2}$) based on AERONET/PHOTONS dataset for the different stations listed in Table 2 (BOA, TOA and ATM refer to bottom of the atmosphere, top of atmosphere and atmospheric forcings).

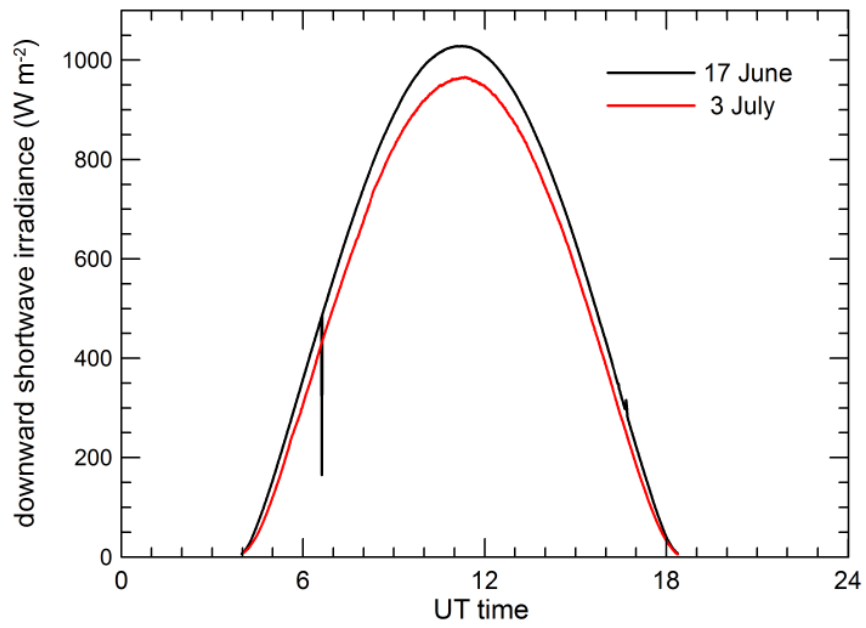


Figure 27. Time evolution of the downward solar irradiance observed at Lampedusa on 17 June and on 3 July, 2013.

2315
 2316
 2317
 2318
 2319
 2320
 2321
 2322
 2323
 2324
 2325
 2326
 2327
 2328
 2329
 2330
 2331
 2332
 2333
 2334
 2335
 2336
 2337
 2338
 2339
 2340
 2341
 2342
 2343
 2344
 2345
 2346
 2347
 2348
 2349
 2350
 2351
 2352

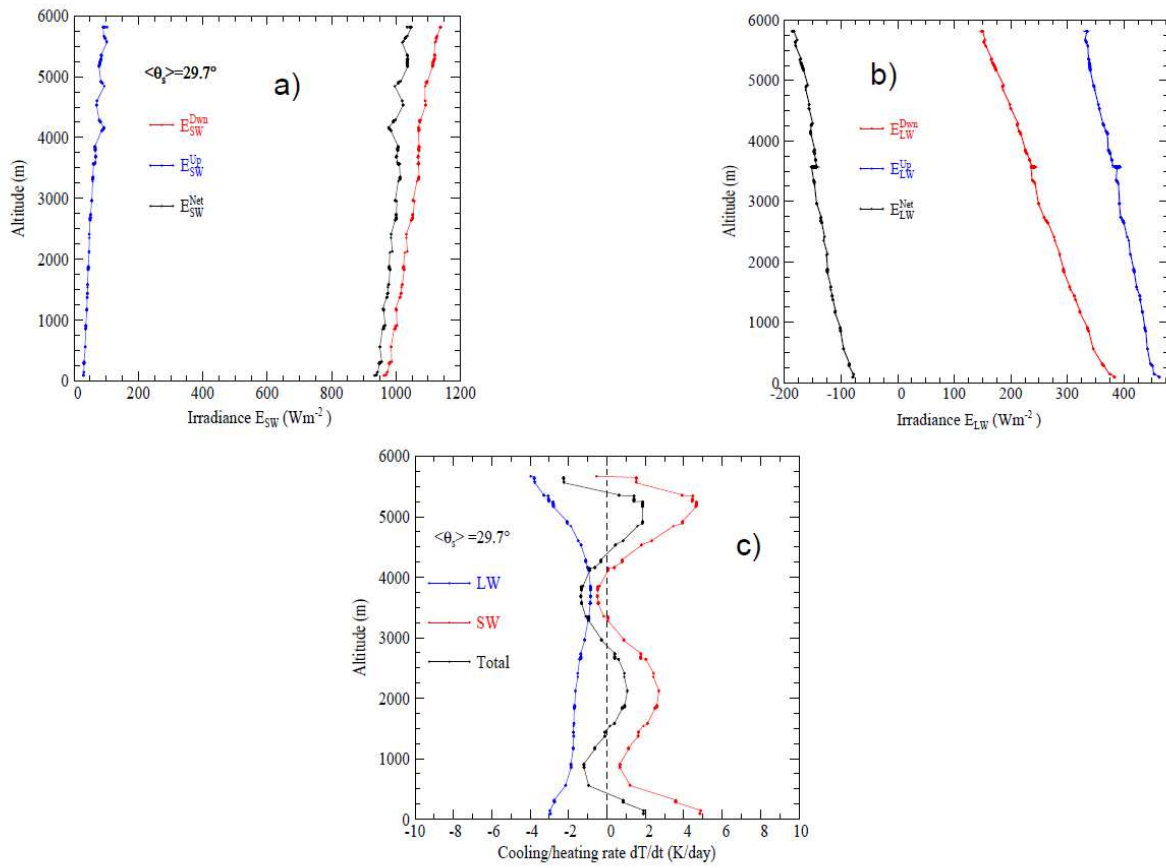
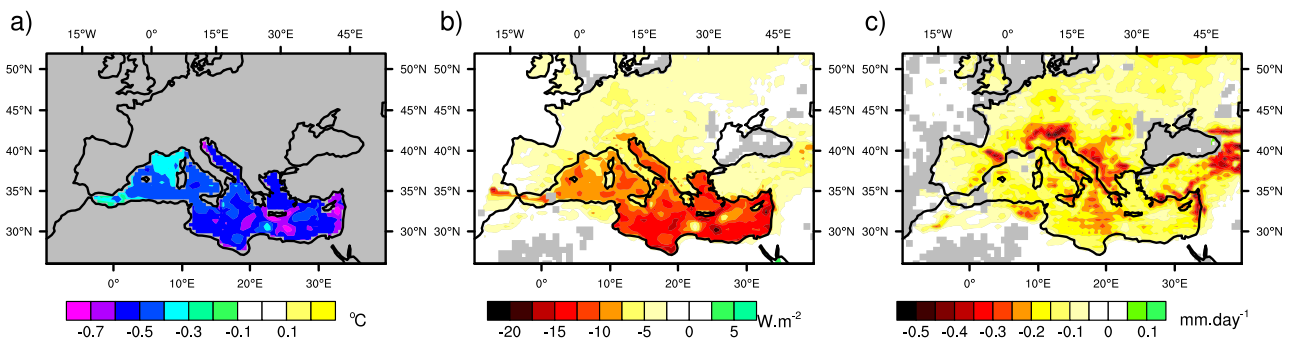


Figure 28. SW (a) and LW (b) upward and downward radiative fluxes observed over the Lampedusa station for the 22 June and estimated SW and LW heating rate (c) in the two spectral regions (see section 5.4.4 for details).

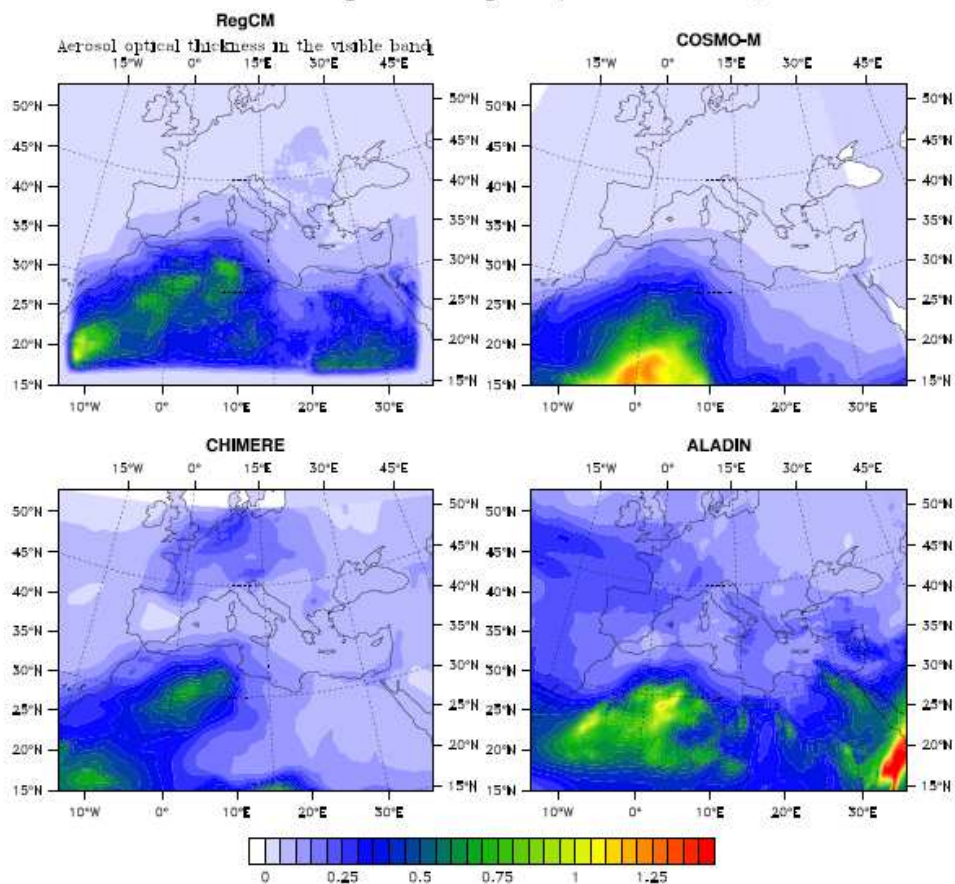
2353
 2354
 2355
 2356
 2357
 2358
 2359
 2360
 2361
 2362
 2362
 2363
 2364
 2365
 2366
 2367
 2368
 2369
 2370
 2371
 2372
 2373
 2374
 2375
 2376
 2377
 2378
 2379
 2380
 2381
 2382



2383
 2384
 2385
 2386
 2387

Figure 29. Annual average difference in (a) Sea Surface Temperature (SST), latent heat loss (b) and precipitation (c) over the period 2003-2009 between a simulation ensemble including aerosols and a second one without any aerosol.

Aerosol optical Depth (visible band)



2388
 2389
 2390
 2391
 2392
 2393
 2394
 2395
 2396
 2397
 2398
 2399
 2400
 2401
 2402
 2403
 2404
 2405
 2406
 2407
 2408
 2409
 2410
 2411
 2412
 2413
 2414
 2415
 2416
 2417

Figure 30. AOD averaged for the 15 to 25 June 2013 period from the meso-scale COSMO-MUSCAT (a), CTM-CHIMERE (b) models and the two regional climate models; CNRM-RCSM (c) and RegCM (d). Details about the model configurations are provided in Table 8.

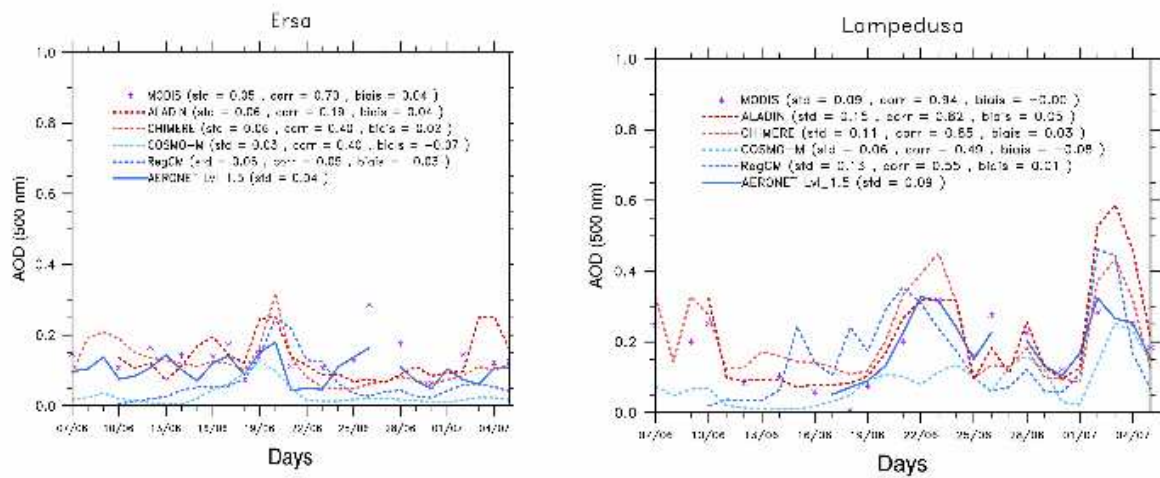
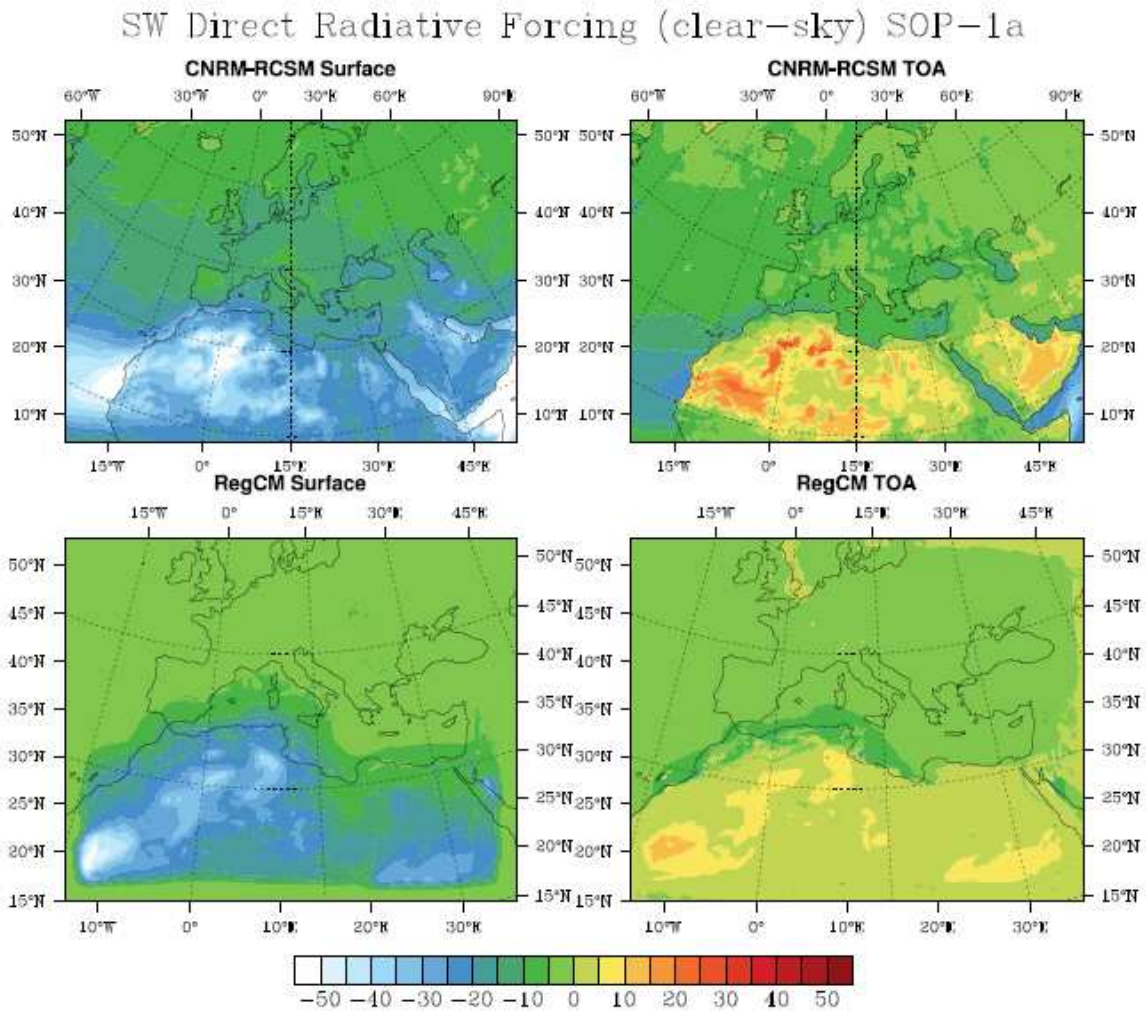


Figure 31. Times-series of AOD comparisons between AERONET/PHOTONS observations and COSMO-MUSCAT, CHIMERE, CNRM-RCSM and RegCM model outputs over the two stations of Ersa and Lampedusa. The MODIS retrievals are also indicated.

2418
 2419
 2420
 2421
 2422
 2423
 2424
 2425
 2426
 2427
 2428
 2429
 2430
 2431
 2432
 2433
 2434
 2435
 2436
 2437
 2438
 2439
 2440
 2441
 2442
 2443
 2444
 2445
 2446
 2447
 2448
 2449
 2450
 2451
 2452

2453
2454



2455
2456
2457
2458
2459
2460
2461
2462

Figure 32. Averaged surface and TOA SW DRF simulated in clear-sky conditions and over the SOP-1a period by the CNRM-RCSM and RegCM models.

	Ersa		Lampedusa	
	Instruments	Frequency	Instruments	Frequency
Number concentration	1 CPC (0.01 - 3 μm)	continuous (1')	1 W-CPC (0.01 - 3 μm)	continuous (2')
CCN concentration	1 CCN counter	continuous	1 CCN counter	continuous
Mass concentration	1 PM2.5	continuous	1 PM40 (TEOM)	continuous
	1 PM10	continuous		
Number size distribution	1 OPC (0.3 - 5 μm)	continuous	2 GRIMM (0.25 - 32 μm)	continuous
	1 APS (TSI)	continuous	1 APS (TSI) (0.5 - 20 μm)	continuous
	1 SMPS (3 - 300 nm)	continuous	2 (dry/ambient) SMPS	continuous
Mass size distribution	2 Impactor DEKATI (13 stages)	48h	2 Impactor DEKATI (13 stages)	48h
			1 Impactor Nano-MOUDI	24 h
PM1 composition	1 PILS	continuous	AMS (Aerodyne)	continuous
			1 PILS	continuous
PM10 composition			1 FAI Hydra Sampler	12h
Mass BC concentration	1 (7- λ) aethalometer	continuous	1 PSAP	continuous (1h)
			1 MAAP	continuous
Vertical Profiles	1 (1- λ 355 nm) Leosphere	continuous	1 (1- λ) Leosphere ALS 300	continuous (20')
			2 (3-l) ENEA/Univ. of Rome lidar	continuous (1')
			microwave radiometer (p, T, RH)	continuous (15')
			radiosondes	on event
Scattering coefficient	1 (3- λ) TSI nephelometer (450-550-700 nm)	continuous (1')	1 (3- λ) TSI nephelometer (450-550-700 nm)	continuous (1')
Absorbing coefficient	1 (7- λ) aethalometer (370-420-490-520-660-880-950 nm)	continuous	1 (7- λ) aethalometer (370-420-490-520-660-880-95 nm)	continuous
Extinction coefficient	1 (1- λ) (860 nm) PAX	continuous (1')		
Column optical properties	1 (9- λ) AERONET/PHOTONS	continuous (15' for AOD)	1 (9- λ) AERONET/PHOTONS	continuous (15' for AOD)
			2 (12-l) MFRSRs	continuous (15 s)
Mineral Aerosol Deposition	1 CARAGA	continuous (7-days)	1 CARAGA	continuous (7-days)
Downward shortwave irradiance	1 pyranometer	continuous (30 s)	1 (CMP 21) pyranometer	continuous (30 s)
Downward longwave irradiance	1 pyrgeometer	continuous (30 s)	1 (CGR4) pyrgeometer	continuous (30 s)
Downward window (8-14 μm) irradiance			1 modified CG3 pyrgeometer	continuous (60 s)
Direct Solar radiance			1 CHP1 Pyrheliometer	continuous (30 s)
Direct spectral solar radiation			1 PMOD Precision SpectroRad.	Continuous (30 s)
Spectral downward global solar irradiance			1 HyperOCR spectrometer	continuous (30 s)

Spectral downward diffuse solar irradiance	1 HyperOCR spectrometer	continuous (30 s)
Spectral direct solar irradiance	1 spectroradiometer	continuous (60 s)
Downward spectral actinic flux	1 Diode array spectrometer	continuous (60s)

Table 1. List of the Instrumentations deployed over the two super-sites (Ersa and Lampedusa) during the SOP-1a experiment for the characterization of physical, chemical and optical properties of aerosols, vertical profiles, columnar-averaged properties and radiation measurements. Meteorological parameters and gas concentrations are not included in this table.

AERONET/PHOTONS Site Name	Latitude (°N)	Longitude (°E)	Altitude (m)	# wavelengths	Site characteristics
Modena	44.63	10.94	56	7	Urban
Avignon	43.93	4.87	32	4	Rural
Villefranche-sur-Mer	43.68	7.33	130	4	Peri-urban coastal
Frioul	43.26	5.29	40	8	Peri-urban coastal
Toulon	43.13	6.00	50	4	Urban coastal
Ersa	43.00	9.35	80	8	Remote island
Rome Tor Vergata	41.84	12.65	130	7	Peri-urban
Barcelone	41.38	2.17	125	4	Urban coastal
IMAA-Potenza	40.60	15.72	820	8	Urban
Lecce University	40.33	18.11	30	7	Peri-urban coastal
Cap d'en Font	39.82	4.21	10	7	Remote Island
Oristano	39.91	8.5	10	4	Peri-urban coastal
Burjassot	39.50	-0.42	30	8	Urban coastal
Majorque	39.55	2.62	10	7	Peri-urban coastal
Cagliari	39.28	9.05	3	7	Urban coastal
Messina	38.20	15.57	15	4	Urban coastal
Granada	37.16	-3.6	680	7	Urban
Malaga	36.71	-4.47	40	7	Peri-urban
Blida	36.50	2.88	230	7	Rural coastal
Lampedusa	35.51	12.63	45	7	Remote Island
Ouijda	34.65	1.90	620	8	Urban coastal
Ouarzazate	30.93	6.91	1136	8	Remote desert

Table 2. List of the long-term AERONET/PHOTONS sun-photometer stations operated in the western Mediterranean during the ChArMEx/ADRIMED (SOP-1a) experiment.

Parameter measured	Instrument	Abreviation	Location in the aircraft	Wavelength (nm)	Nominal size range (μm)
Size distribution	Forward Scattering Spectrometer Probe, Model 300, Particle Measuring Systems	FSSP-300	wing-mounted	632.8	0.28-20
	Ultra High Sensitivity Aerosol Spectrometer, Droplet Measurement Technologies	UHSAS	wing-mounted	1054	0.04-1
	Sky-Optical Particle Counter, Model 1.129, Grimm Technik	GRIMM1	AVIRAD inlet	655	0.25-32
	Optical Particle Counter, Model 1.109, Grimm Technik	GRIMM2	Communautory aerosol inlet	655	0.25-32
	Optical Particle Counter, Model 1.109, Grimm Technik	GRIMM3	Communautory aerosol inlet	655	0.25-32
	Scanning mobility particle sizer, custom-built (Villani et al., 2007)	SMPS	Communautory aerosol inlet	n/a	0.03-0.4
Integrated number concentration	Condensation Particle Counters, Model 3075, TSI	CPC	AVIRAD inlet	n/a	> 0.005
Scattering coefficient	3λ Integrated Nephelometer, Model 3563, TSI	Nephelometer	AVIRAD inlet	450, 550, 700	n/a
Absorption coefficient	3λ Particle Soot Absorption Photometer, Radiance Research	PSAP	Communautory aerosol inlet	467, 530, 660	n/a
Extinction coefficient	Cavity Attenuated Phase Shift, Aerodyne Research Inc.	CAPS	Communautory Aerosol inlet	530	n/a
	Photomètre Léger Aéroporté pour la Surveillance des Masses d'Air	PLASMA	roof-mounted	340-2250	n/a
Chemical composition	Filter sampling	n/a	AVIRAD inlet	n/a	n/a
	Single particle soot photometer, Droplet Measurement Technologies	SP2	Communautory aerosol inlet	1064	0.08-0.5

Table 3. In-situ instrumentation deployed onboard the ATR-42 during the SOP-1a experiment.

No.	Date (2013)	Start time (UTC)	Ceiling altitude (m)	Latitude at ceiling	Longitude at ceiling	Sensors
BLD1	12 June	21:13	21178	39.5156°N	04.3010°E	T, U
BLD2	15 June	21:40	32119	39.9903°N	04.1801°E	T, U, LOAC, O ₃
BLD3	16 June	10:29	31880	40.0527°N	04.1524°E	T, U, LOAC, O ₃
BLD4	16 June	21:13	33390	40.0999°N	04.0118°E	T, U, LOAC, O ₃
BLD5	17 June	10:01	32744	40.2109°N	03.9672°E	T, U, LOAC, O ₃
BLD6	17 June	18:25	33411	40.2502°N	03.9402°E	T, U, LOAC, O ₃
BLD7	18 June	16:34	35635	40.5832°N	04.0515°E	T, U, LOAC
BLD8	18 June	21:17	21507	40.6372°N	04.4889°E	T, U, LOAC, O ₃
BLD9	19 June	10:12	30902	40.6794°N	04.3691°E	T, U, LOAC, O ₃
BLD10	19 June	13:48	36129	40.6553°N	04.1970°E	T,U, LOAC
BLD11	27 June	09:43	35832	39.7546°N	04.4746°E	T,U, LOAC
BLD12	28 June	05:36	36293	39.4505°N	04.1709°E	T,U, LOAC
BLD13	29/30 June	23:31	36310	39.6168°N	03.7383°E	T,U, LOAC
BLD14	30 June	14:03	36319	39.8937°N	03.9568°E	T,U, LOAC
BLD15	02 July	10:27	32833	39.9942°N	04.2996°E	T, U, LOAC, O ₃

Table 4. Characteristics of the 15 sounding balloon flights from Sant Lluís, Minorca Island, during the ChArMEx SOP1a/ADRIMED campaign.

Date and time of launch (UT)	Balloon Nbr and type of sensor	Last data time (UT)	Last data location	Trajectory length (km)	Flight duration (h)	Approximate float altitude (m)
16 June, 09:46	B74, LOAC	16 June, 21:51	43.0265°N 05.2285°E	368	11:57	2100
16 June, 09:53	B53, O3	17 June, 00:26	40.6541°N 06.2398°E	203	14:28	3000-3050
16 June, 09:58	B70, LOAC	16 June, 23:01	40.1825°N 06.1293°E	174	13:17	3050-3150
17 June, 09:27	B54, O3	17 June, 16:49	43.1433°N 03.5293°E	371	07:22	1850-2000
17 June, 09:29	B75, LOAC	17 June, 16:51	43.0868°N 03.6866°E	365	07:23	1950-2050
17 June, 11:07	B72, LOAC	17 June, 19:07	43.2333°N 04.7403°E	382	08:03	2750
19 June, 10:34	B77, LOAC	19 June, 17:59	43.1576°N 04.7562°E	387	07:37	2550
19 June, 10:35	B71, LOAC	19 June, 15:03	43.0560°N 05.1336°E	369	04:39	3250-3350
27 June, 10:00	B80, LOAC	28 June, 12:07	37.9165°N 12.1605°E	759	26:19	2950-3050
28 June, 05:20	B73, LOAC	28 June, 17:24	37.4095°N 09.2346°E	523	12:16	2650-2750
02 July, 13:03	B76, LOAC	03 July,, 09:38	37.8897°N 12.1312°E	731	20:39	3150-3250
02 July, 13:11	B57, O3	03 July, 22:43	35.0900°N 14.1140°E	1053	33:44	3100-3200
02 July, 17:59	B55, O3	04 July, 02:20	37.3545°N 12.21980E	762	32.32	2400-2450
02 July, 17:50	B78, LOAC	04 July, 02:13	37.5639°N 12.1507°E	755	32.25	2350-2450

Table 5. Characteristics of the 14 BPCL drifting balloon flights.

	Ersa	Ersa corrected	Lampedusa	Cagliari	Cap d'En Font
Number of observations	25		18	20	17
r_{vf} (μm)	0.16 ± 0.02	#	0.14 ± 0.01	0.15 ± 0.03	0.17 ± 0.03
σ_f	0.43 ± 0.03	#	0.50 ± 0.06	0.46 ± 0.04	0.45 ± 0.04
r_{vc} (μm)	2.49 ± 0.43	#	2.36 ± 0.48	2.52 ± 0.28	2.48 ± 0.30
σ_c	0.69 ± 0.03	#	0.68 ± 0.05	0.71 ± 0.04	0.71 ± 0.04
C_{vf} ($\mu\text{m}^3/\mu\text{m}^2$)	0.02 ± 0.01	#	0.02 ± 0.01	0.02 ± 0.01	0.02 ± 0.01
C_{vc} ($\mu\text{m}^3/\mu\text{m}^2$)	0.03 ± 0.01	0.04	0.08 ± 0.05	0.05 ± 0.03	0.04 ± 0.03

Table 6. Main aerosol volume size distribution characteristics: r_{vf} (μm), σ_f , r_{vc} (μm), σ_c , C_{vf} , C_{vc} , for the four different AERONET/PHOTONS stations: Ersa, Lampedusa, Cagliari and Cap d'En Font. C_{vi} denotes the particle volume concentration, r_{vi} is the median radius, and σ_i is the standard deviation. Each average value in the table is accompanied by its standard deviation (this is not an accuracy of the retrieval). As mentioned in the text, the concentration of the coarse mode at Ersa has been corrected to be comparable to results at other stations closer to the sea surface, using the logarithmic law proposed by Piazzola et al. (2015).

Models	Time of simulation	Horizontal resolution	Number of vertical layers	Aerosol species	Boundary Layer Forcing	Radiative transfer code
CHIMERE	01/06 31/07	- 50 km	20	Dust, Sea Salt, Secondary organic and inorganic, primary OC-BC	WRF	FastJX
CNRM-RCSM	01/06 31/07	- 50 km	31	Dust, Sea-Salt, Sulphates, primary OC-BC	ERA-Interim	SW: FMR (6 bands, Morcrette et al., 1989) LW: RRTM (Mlawer et al., 1997)
RegCM	13/06 05/07	- 25 km	23	Dust, Sea-Salt, Secondary inorganic, primary OC-BC	NCEP reanalysis	CCM3 or RRTM
COSMO-MUSCAT	15/05-31/07	28 km	40	Dust	GME	Ritter & Geleyn (1992)

Table 7. Main characteristics (period of simulations, horizontal resolution, number of vertical layers, main aerosol (primary and/or secondary) species, radiative transfer codes) of the four different 3-D models used during the SOP-1a experiment (see part. 6) (GME is for the global model of the German Weather Service).

References

- Alados-Arboledas, L., Lyamani, H., Olmo, F.J. Aerosol size properties at Armilla, Granada (Spain), Quarterly Journal of the Royal Meteorological Society, 129 (590 PART A), pp. 1395-1413, 2003.
- Alados-Arboledas, L., Alcántara, A., Olmo, F.J., Martínez-Lozano, J.A., Estellés, V., Cachorro, V., Silva, A.M., Horvath, H., Gangl, M., Díaz, A., Pujadas, M., Lorente, J., Labajo, A., Sorribas, M., Pavese, G.: Aerosol columnar properties retrieved from CIMEL radiometers during VELETA 2002, Atmos. Environ., 42, 2654-2667, 2008.
- Alados-Arboledas, L., et al.: Remote-sensing and in-situ characterization of atmospheric aerosol during ChArMEx/ADRIMED over Granada, in prep. for this special issue, 2015.
- Amiridis, V., Zerefos, C., Kazadzis, S., Gerasopoulos, E., Eleftheratos, K., Vrekoussis, M., Stohl, A., Mamouri, R.E., Kokkalis, P., Papayannis, A., Eleftheriadis, K., Diapouli, E., Keramitsoglou, I., Kontoes, C., Kotroni, V., Lagouvardos, K., Marinou, E., Giannakaki, E., Kostopoulou, E., Giannakopoulos, C., Richter, A., Burrows, J.P., Mihalopoulos, N.: Impact of the 2009 Attica wild fires on the air quality in urban Athens, Atmos. Environ. 46, 536–544, 2012.
- Ancellet, G., Pelon, J., Totems, J., Chazette, P., Bazureau, A., Sicard, M., Di Iorio, T., Dulac, F., and Mallet, M.: Mixing of aerosol sources during the North American biomass burning episode in summer 2013: analysis of lidar observations in the Mediterranean basin, Atmos. Chem. Phys. Discuss., submitted to this special issue, 2015.
- Antón, M., Valenzuela, A., Mateos, D., Alados, I., Foyo-Moreno, I., Olmo, F. J., Alados-Arboledas, L.: Longwave aerosol radiative effects during an extreme desert dust event in southeastern Spain, Atmos. Res., 148, 18-23, 2014.
- Baldassarre, G., Pozzoli, L., Schmidt, C. C., Unal, A., Kindap, T., Menzel, W. P., Whitburn, S., Coheur, P.-F., Kavgaci, A., and Kaiser, J. W.: Using SEVIRI fire observations to drive smoke plumes in the CMAQ air quality model: a case study over Antalya in 2008, Atmos. Chem. Phys., 15, 8539-8558, doi:10.5194/acp-15-8539-2015, 2015.
- Balis, D.S., Amiridis, V., Nickovic, S., Papayannis, A., and Zerefos, C.: Optical properties of Saharan dust layers as detected by a Raman lidar at Thessaloniki, Greece, Geophys. Res. Lett., 31, L13104, doi:10.1029/2004GL019881, 2004.
- Balis, D., Amiridis, V., Kazadzis, S., Papayannis, A., Tsaknakis, G., Tzortzakis, S., Kalivitis, N., Vrekoussis, M., Kanakidou, M., Mihalopoulos, N., Chourdakis, G., Nickovic, S., Pérez, C., Baldasano, J., and Drakakis, M.: Optical characteristics of desert dust over the East Mediterranean during summer: a case study, Ann. Geophys., 24, 807-821, 2006.
- Barnaba, F., Angelini, F., Curci, G., and Gobbi, G. P.: An important fingerprint of wildfires on the European aerosol load, Atmos. Chem. Phys., 11, 10487-10501, doi:10.5194/acp-11-10487-2011, 2011.
- Barragan, R., Sicard, M., Totems, J., Léon, J.-F., Renard, J.-B., Dulac, F., Mallet, M., Pelon, J., Alados-Arboledas, L., Amodeo, A., Augustin, P., Boselli, A., Bravo-Aranda, J. A., Burlizzi, P., Chazette, P., Comerón, A., D'Amico, G., Granados-Muñoz, M. J., Leto, G., Guerrero-Rascado, J. L., Madonna, F., Mona, L., Muñoz-Porcar, C., Pappalardo, G., Perrone, M. R., Pont, V., Rocadenbosch, F., Rodriguez, A., Scollo, S., Spinelli, N., Titos, G., Wang, X., and Zanmar Sanchez, R.: Characterization of aerosol transport and ageing during a multi-intrusion Saharan dust event over the western and central Mediterranean Basin in June 2013 in the framework of the ADRIMED/ChArMEx campaign, Atmos. Chem. Phys., in prep. for this special issue, 2015.
- Berthier, S., Chazette, P., Couvert, P., Pelon, J., Dulac, F., Thieuleux, F., Moulin, C., and Pain, T.: Desert dust aerosol columnar properties over ocean and continental Africa from Lidar in-Space Technology Experiment (LITE) and Meteosat synergy, J. Geophys. Res., 111, D21202, doi:10.1029/2005JD006999, 2006.
- Bessagnet, B., Hodzic, A., Vautard, R., Beekmann, M., Cheinet, S., Honoré, C., Liousse, C., and Rouil, L.: Aerosol modeling with CHIMERE: preliminary evaluation at the continental scale, Atmos. Environ., 38, 2803–2817, 2004.
- Beuvier, J., Sevault, F., Herrmann, M., Kontoyiannis, H., Ludwig, W., Rixen, M., Stanev, E., Béranger, K., and Somot, S.: Modeling the Mediterranean Sea interannual variability during 1961–2000: Focus on the Eastern Mediterranean Transient, J. Geophys. Res., 115, C08017, doi:10.1029/2009JC005950, 2010.
- Brauch, H.G.: Urbanization and natural disasters in the Mediterranean: Population growth and climate change in the 21st century, in Building Safer Cities – The Future of Disaster Risk, Edited by Kreimer, A., Arnold, M., and Carlin, A., The World Bank, Disaster Risk Management Series No.3, 149-164, 2003.
- Cachier, H., Aulagnier, F., Sarda, R., Gautier, F., Masplet, P., Besombes, J.L., Marchand, N., Despiiau, S., Croci, D., Mallet, M., Laj, P., Marinoni, A., Deveau, P.A., Roger, J.C., Putaud, J.P., Van Dingenen, R., Dell'Acqua, A., Viidanoja, J., Martins-Dos Santos, S., Liousse, C., Cousin, F., and Rosset, R.: Aerosol studies during the ESCOMPTE Experiment: an overview, Atmos. Res., 74, 547-563, doi:10.1016/j.atmosres.2004.06.013, 2005.

- Cachorro, V. E., Toledano, C., Prats, N., Sorribas, M., Mogo, S., Berjon, A., Torres, B., Rodrigo, R., J. de la Rosa, and De Frutos, A.M.: The strongest desert dust intrusion mixed with smoke over the Iberian Peninsula registered with Sun photometry, *J. Geophys. Res.*, 113, D14S04, doi:10.1029/2007JD009582, 2008.
- Casasanta, G., di Sarra, A., Meloni, D., Monteleone, F., Pace, G., Piacentino, S., and Sferlazzo, D.: Large aerosol effects on ozone photolysis in the Mediterranean, *Atmos. Environ.*, 45, 3937-3943, doi:10.1016/j.atmosenv.2011.04.065, 2011.
- Chazette, P., and Lioussé, C.: A case study of optical and chemical ground apportionment for urban aerosols in Thessaloniki, *Atmos. Environ.*, 35, 2497-2506, doi:10.1016/S1352-2310(00)00425-8, 2001.
- Chazette, P., Marnas, F., and Totems, J.: The mobile Water vapor Aerosol Raman Lidar and its implication in the framework of the HyMeX and ChArMEx programs: application to a dust transport process, *Atmos. Meas. Tech.*, 7, 1629-1647, doi:10.5194/amt-7-1629-2014, doi:10.5194/amt-7-1629-2014, 2014a.
- Chazette, P., Marnas, F., Totems, J., and X. Shang, J.: Comparison of IASI water vapor retrieval with H₂O-Raman lidar in the framework of the Mediterranean HyMeX and ChArMEx programs, *Atmos. Chem. Phys.*, 14, 9583-9596, doi:10.5194/acp-14-9583-2014, doi:10.5194/acp-14-9583-2014, 2014b.
- Chazette, P., Totems, J., Ancellet, G., Pelon, J., and Sicard, M.: Temporal consistency of lidar observables during aerosol transport events in the framework of the ChArMEx/ADRIMED campaign at Menorca Island in June 2013, *Atmos. Chem. Phys. Discuss.*, submitted to this special issue, 2015.
- Chenoweth J., Hadjinicolaou, P., Bruggeman, A., Lelieveld, J., Levin, Z., Lange, M. A., Xoplaki, E., and Hadzikakou, M.: Impact of climate change on the water resources of the eastern Mediterranean and middle east region: modeled 21st century, *Water Resour. Res.*, 47, W06506, doi:10.1029/2010WR010269, 2011.
- Ciardini, V., Di Iorio, T., Di Liberto, L., Tirelli, C., Casasanta, G., di Sarra, A., Fiocco, G., Fuà, D., and Cacciani, M.: Seasonal variability of tropospheric aerosols in Rome, *Atmos. Res.*, 118, 205-214, doi:10.1016/j.atmosres.2012.06.026, 2012.
- Claeys, M., Roberts, G., Mallet, M., Sciare, J., Sellegri, K., Sauvage, B., Tulet, P., Arndt, J.: Characterisation of a sea salt episode during ADRIMED campaign: ageing, transport and size distribution study, in prep. for this special issue, 2015.
- Collaud Coen, M., Weingartner, E., Schaub, D., Hueglin, C., Corrigan, C., Henning, S., Schwikowski, M., and Baltensperger, U.: Saharan dust events at the Jungfraujoch: detection by wavelength dependence of the single scattering albedo and first climatology analysis, *Atmos. Chem. Phys.*, 4, 2465-2480, 2004.
- Denjean, C., Chevaillier, S., Triquet, S., Grand, N., Cassola, F., Mazzino, A., Bourriane, T., Momboisse, G., Dupuy, R., Sellegri, K., Schwarzenbock, A., Mallet, M., and Formenti, P.: Size distribution and optical properties of mineral dust aerosols transported in the West Mediterranean, *Atmos. Chem. Phys. Discuss.*, 15, 21607-21669, 2015.
- Déqué, M. and Somot, S.: Extreme precipitation and high resolution with Aladin, *Idöjaras Quaterly Journal of the Hungarian Meteorological Service*, 112, 179-190, 2008.
- Derimian, Y., Karnieli, A., Kaufman, Y. J., Andreae, M. O., Andreae, T. W., Dubovik, O., Maenhaut, W., Koren, I., and Holben, B. N.: Dust and pollution aerosols over the Negev desert, Israel: Properties, transport, and radiative effect, *J. Geophys. Res.*, 111, D05205, doi:10.1029/2005JD006549, 2006.
- Deschamps, P.-Y., Bréon, F.-M., Leroy, M., Podaire, A., Bricaud, A., Buriez, J.C., and Sèze, G.: The POLDER mission: Instrument characteristics and scientific objectives, *IEEE Trans. Geosci. Remote Sens.*, 32, 598-615, 1994.
- Di Biagio, C., di Sarra, A., Meloni, D., Monteleone, F., Piacentino, S., and Sferlazzo, D.: Measurements of Mediterranean aerosol radiative forcing and influence of the single scattering albedo, *J. Geophys. Res.*, 114, D06211, doi:10.1029/2008JD011037, 2009.
- Di Biagio, C., di Sarra, A., and D. Meloni, D.: Large atmospheric shortwave radiative forcing by Mediterranean aerosol derived from simultaneous ground-based and spaceborne observations, and dependence on the aerosol type and single scattering albedo, *J. Geophys. Res.*, 115, D10209, doi:10.1029/2009JD012697, 2010.
- Di Iorio, T., Di Sarra, A., Junkermann, W., Cacciani, M., Fiocco, G., and Fuà, D.: Tropospheric aerosols in the Mediterranean: 1. Microphysical and optical properties, *J. Geophys. Res.*, 108, 4316, doi:10.1029/2002JD002815, 2003.
- Di Iorio, T., di Sarra, A., Sferlazzo, D. M., Cacciani, M., Meloni, D., Monteleone, F., Fuà, D., and Fiocco, G.: Seasonal evolution of the tropospheric aerosol vertical profile in the central Mediterranean and role of desert dust, *J. Geophys. Res.*, 114, D02201, doi:10.1029/2008JD010593, 2009.
- Di Iorio, T., Di Biagio, C., di Sarra, A., Formenti, P., Gomez Amo, J.-L., Meloni, D., and Pace, G.: Height resolved aerosol optical properties at Lampedusa during ADRIMED, in prep. for this special issue, 2015.
- di Sarra, A., Pace, G., Meloni, D., De Silvestri, L., Piacentino, S., and Monteleone, F.: Surface shortwave radiative forcing of different aerosol types in the central Mediterranean, *Geophys. Res. Lett.*, 35, L02714,

- doi:10.1029/2007GL032395, 2008.
- di Sarra, A., Di Biagio, C., Meloni, D., Monteleone, F., Pace, G., Pugnaghi, S., and Sferlazzo, D.: Shortwave and longwave radiative effects of the intense Saharan dust event of 25-26 March 2010 at Lampedusa (Mediterranean Sea), *J. Geophys. Res.*, 116, D23209, doi:10.1029/2011JD016238, 2011.
- di Sarra, A., Sferlazzo, D., Meloni, D., Anello, F., Bommarito, C., Corradini, S., De Silvestri, L., Di Iorio, T., Monteleone, F., Pace, G., Piacentino, S., and Pugnaghi, S.: Empirical correction of multi filter rotating shadowband radiometer (MFRSR) aerosol optical depths for the aerosol forward scattering and development of a long-term integrated MFRSR-Cimel dataset at Lampedusa, *Appl. Opt.*, 54, 2725-2737, doi:10.1364/AO.54.002725, 2015.
- Dubovik, O., and King, M. D.: A flexible inversion algorithm for retrieval of aerosol optical properties from Sun and sky radiance measurements, *J. Geophys. Res.*, 105, 20673–20696, doi:10.1029/2000JD900282, 2000.
- Dubovik, O., Smirnov, A., Holben, B. N., King, M. D., Kaufman, Y. J., Eck, T. F., and Slutsker, I.: Accuracy assessment of aerosol optical properties retrieval from AERONET Sun and sky radiance measurements, *J. Geophys. Res.*, 105, 9791–9806, doi:10.1029/2000JD900040, 2000.
- Dubovik, O., Holben, B., Eck, T.F., Smirnov, A., Kaufman, Y.J., King, M.D., Tanré, D., and Slutsker, I.: Variability of absorption and optical properties of key aerosol types observed in worldwide locations, *J. Atmos. Sci.*, 59, 590–608, doi:http://dx.doi.org/10.1175/1520-0469(2002)059<0590:VOAAOP>2.0.CO;2, 2002.
- Dubovik, O., Sinyuk, A., Lapyonok, T., Holben, B. N., Mishchenko, M., Yang, P., Eck, T. F., Volten, H., Muñoz, O., Veihelmann, B., van der Zande, W. J., Léon, J.-F., Sorokin, M., and Slutsker, I.: Application of spheroid models to account for aerosol particle nonsphericity in remote sensing of desert dust, *J. Geophys. Res.*, 111, D11208, doi:10.1029/2005JD006619, 2006.
- Dubovik, O., Herman, M., Holdak, A., Lapyonok, T., Tanré, D., Deuzé, J. L., Ducos, F., Sinyuk, A., and Lopatin, A.: Statistically optimized inversion algorithm for enhanced retrieval of aerosol properties from spectral multi-angle polarimetric satellite observations, *Atmos. Meas. Tech.*, 4, 975-1018, doi:10.5194/amt-4-975-2011, 2011.
- Dubuisson, P., Dessailly, D., Vesperini, M., and Frouin, R.: Water vapor retrieval over ocean using near-infrared radiometry, *J. Geophys. Res.*, 109, D19106, doi:10.1029/2004JD004516, 2004.
- Ducrocq, V., Braud, I., Davolio, S., Ferretti, R., Flamant, C., Jansa, A., Kalthoff, N., Richard, E., Taupier-Letage, I., Ayrat, P.A., Belamari, S., Berne, A., Borga, M., Boudevillain, B., Bock, O., Boichard, J.L., Bouin, M.N., Bousquet, O., Bouvier, C., Chiggiato, J., Cimini, D., Corsmeier, U., Coppola, L., Cocquerez, P., Defer, E., Delanoë, J., Delrieu, G., Di Girolamo, P., Doerenbecher, A., Drobinski, P., Dufournet, Y., Fourrié, N., Gourley, J.J., Labatut, L., Lambert, D., Le Coz, J., Marzano, F.S., Montani, A., Nuret, M., Ramage, K., Rison, B., Rousset, O., Saïd, F., Schwarzenboeck, A., Testor, P., Van Baelen, J., Vincendon, B., Aran, M., and Tamayo J.: HyMeX-SOP1, the Field Campaign Dedicated to Heavy Precipitation and Flash-Flooding in Northwestern Mediterranean. *Bull. Amer. Meteorol. Soc.*, 95, 1083-1100, doi: 10.1175/BAMS-D-12-00244.1 and doi: 10.1175/BAMS-D-12-00244.2, 2014.
- Dulac, F., and Chazette, P.: Airborne study of a multi-layer aerosol structure in the eastern Mediterranean observed with the airborne polarized lidar ALEX during a STAAARTE campaign (7 June 1997), *Atmos. Chem. Phys.*, 3, 1817-1831, 2003.
- Eleftheriadis, K., Colbeck, I., Housiada, C., Lazaridis, M., Mihalopoulos, N., Mitsakou, C., Smolik, J., and Zdimal, V.: Size distribution, composition and origin of the submicron aerosol in the marine boundary layer during the eastern Mediterranean “SUB-AERO” experiment, *Atmos. Environ.*, 40, 6245–6260, 2006.
- Foltz, G.R., and McPhaden, M.J., Impact of Saharan dust on tropical North Atlantic SST, *J. Climate*, 21, 5048-5060, doi: http://dx.doi.org/10.1175/2008JCLI2232.1, 2008.
- Formenti, P., Boucher, O., Reiner, T., Sprung, D., Andreae, M. O., Wendisch, M., Wex, H., Kindred, D., Tzortziou, M., Vasaras, A., and Zerefos, C.: STAAARTE-MED 1998 summer airborne measurements over the Aegean Sea, 2. Aerosol scattering and absorption, and radiative calculations, *J. Geophys. Res.* 107, 4451, doi:10.1029/2001JD001536, 2002.
- Formenti, P., et al.: Characterisation of aerosols in a remote marine atmosphere in the West Mediterranean, *Atmos. Chem. Phys. Discuss.*, in prep. for this special issue, 2015.
- Fotiadi, A., Hatzianastassiou, N., Drakakis, E., Matsoukas, C., Pavlakis, K.G., Hatzidimitriou, D., Gerasopoulos, E., Mihalopoulos, N., and Vardavas, I.: Aerosol physical and optical properties in the Eastern Mediterranean Basin, Crete, from Aerosol Robotic Network data, *Atmos. Chem. Phys.*, 6, 5399–5413, doi:10.5194/acp-6-5399-2006, 2006.
- Gangoiti, G., Millán, M., Salvador, R., and Mantilla, E.: Long-range transport and re-circulation of pollutants in the western Mediterranean during the project Regional Cycles of Air Pollution in the West-Central Mediterranean Area, *Atmos. Environ.*, 35, 6267-6276, doi:10.1016/S1352-2310(01)00440-X, 2001.
- Garcia, O. E., Diaz, J. P., Exposito, F. J., Diaz, A. M., Dubovik, O., Derimian, Y., Dubuisson, P., and Roger, J.-C.:

- Shortwave Radiative Forcing and Efficiency of Key Aerosol Types using AERONET Data, *Atmos. Chem. Phys.*, 12, 5129-5145, doi:10.5194/acp-12-5129-2012, 2012.
- García-Ruiz, J. M., López-Moreno, J. I., Vicente-Serrano, S. M., Lasanta-Martínez, T., and Beguería, S.: Mediterranean water resources in a global change scenario, *Earth-Sci. Rev.*, 105, 121-139, doi:10.1016/j.earscirev.2011.01.006, 2011.
- Gard, E., Mayer, J. E., Morrical, B. D., Dienes, T., Fergenson, D. P., and Prather, K.A.: Real-time analysis of individual atmospheric aerosol particles: Design and performance of a portable ATOFMS, *Anal. Chem.*, 69, 4083-4091, doi:10.1021/ac970540n, 1997.
- Gerasopoulos, E., Andreae, M.O., Zerefos, C.S., Andreae, T.W., Balis, D., Formenti, P., Merlet, P., Amiridis, V., and Papastefanou, C.: Climatological aspects of aerosol optical properties in Northern Greece, *Atmos. Chem. Phys.*, 3, 2025-2041, doi:10.5194/acp-3-2025-2003/, 2003.
- Gheusi, F., Durand, P., Verdier, N., Dulac, F., Attié, J.-L., Commun, P., Barret, B., Basdevant, C., Clenet, A., Derrien, S., Doerenbecher, El Amraoui, L., Fontaine, A., Hache, E., Lambert C., Jaumouillé, E., Meyerfeld, Y., Roblou, L., and Tocquer, F.: Adapted ECC ozone sonde for long-duration flights aboard boundary-layer pressurized balloons, *Atmos. Meas. Tech.*, in prep. for this special issue, 2015.
- Gimeno, L., Drumond, A., Nieto, R., Trigo, R. M., and Stohl, A.: On the origin of continental precipitation, *Geophys. Res. Lett.*, 37, L13804, doi:10.1029/2010GL043712, 2010.
- Giorgi, F., and Lionello, P.: Climate change projections for the Mediterranean region, *Global Planet. Change*, 63, 90-104, doi:10.1016/j.gloplacha.2007.09.005, 2008.
- Giorgi, F., Coppola, E., Solmon, F., Mariotti, L., Sylla, M. B., Bi, X., Elguindi, N., Diro, G.T., Nair, V., Giuliani, G., Turuncoglu, U. U., Cozzini, S., Guttler, I., O'Brien, T. A., Tawfik, A. B., Shalaby, A., Zakey, A. S., Steiner, A. L., Stordal, F., Sloan, L. C., and Brankovic, C.: RegCM4: Model description and preliminary tests over multiple CORDEX domains, *Clim. Res.*, 52, 7-29, doi: 10.3354/cr01018, 2012.
- Gobbi, G.P., Barnaba, F., Giorgi, R., and Santacasa, A.: Altitude-resolved properties of a Saharan dust event over the Mediterranean, *Atmos. Environ.*, 34, 5119-5127, 2000.
- Gross, D. S., Atlas, R., Rzeszutarski, J., Turetsky, E., Christensen, J., Benzaid, S., Olson, J., Smith, T., Steinberg, L. and Sulman, J.: Environmental chemistry through intelligent atmospheric data analysis, *Environ. Model. Software*, 25, 760-769, doi: 10.1016/j.envsoft.2009.12.001, 2010.
- Guenther, A., Karl, T., Harley, P., Wiedinmyer, C., Palmer, P. I., and Geron, C.: Estimates of global terrestrial isoprene emissions using MEGAN (Model of Emissions of Gases and Aerosols from Nature), *Atmos. Chem. Phys.*, 6, 3181-3210, doi:10.5194/acp-6-3181-2006, 2006.
- Guerrero-Rascado, J. L., Olmo, F. J., Avilés-Rodríguez, I., Navas-Guzmán, F., Pérez-Ramírez, D., Lyamani, H., Arboledas, L.A.: Extreme saharan dust event over the southern iberian peninsula in september 2007: Active and passive remote sensing from surface and satellite, *Atmos. Chem. and Phys.*, 9 (21), 8453-8469, 2009.
- Hamonou, E., Chazette, P., Balis, D., Dulac, F., Schneider, X., Galani, E., Ancellet, G., and Papayannis, A.: Characterization of the vertical structure of Saharan dust export to the Mediterranean basin, *J. Geophys. Res.*, 104, 22257-22270, 1999.
- Hashimoto, M., Nakajima, T., Dubovik, O., Campanelli, M., Che, H., Khatri, P., Takamura, T., and Pandithurai, G.: Development of a new data-processing method for SKYNET sky radiometer observations, *Atmos. Meas. Tech.*, 5, 2723-2737, doi:10.5194/amt-5-2723-2012, 2012.
- Harris, I, Jones, P., Osborn, T., Lister, D.: Updated high-resolution grids of monthly climatic observations—the cru ts3.10 dataset. *Int J Climatol* 34:623-642. doi:10.1002/joc.3711, 2013.
- Hatzianastassiou, N., Gkikas, A., Mihalopoulos, N., Torres, O., and Katsoulis, B. D.: Natural versus anthropogenic aerosols in the eastern Mediterranean basin derived from multiyear TOMS and MODIS satellite data, *J. Geophys. Res.*, 114, D24202, doi:10.1029/2009JD011982, 2009.
- Healy, R. M., Hellebust, S., Kourtchev, I., Allanic, A., O'Connor, I. P., Bell, J. M., Sodeau, J. R., Wenger, J. C., Healy, D. A., Sodeau, J. R., and Wenger, J. C.: Source apportionment of PM_{2.5} in Cork Harbour, Ireland using a combination of single particle mass spectrometry and quantitative semi-continuous measurements, *Atmos. Chem. Phys.*, 10, 9593-9613. doi:10.5194/acpd-10-1035-2010, 2010.
- Holben B.N., Eck, T.F., Slutsker, I., Tanré, D., Buis, J.P., Setzer, A., Vermote, E., Reagan, J.A., Kaufman, Y.J., Nakajima, T., Lavenu, F., Jankowiak, I., and Smirnov, A.: AERONET - A federated instrument network and data archive for aerosol characterization, *Rem. Sens. Environ.*, 66, 1-16, doi:10.1016/S0034-4257(98)00031-5, 1998.
- Horvath, H., Alados Arboledas, L., Olmo, F.J., Jovanovic, O., Gangl, M., Sanchez, C., Sauerzopf, H., and Seidl, S.: Optical characteristics of the aerosol in Spain and Austria and its effect on radiative forcing, *J. Geophys. Res.*, 107, 4386, doi:10.1029/2001JD001472, 2002.
- Johnson, G., Ristovski, Z., and Morawska, L.: Application of the VH-TDMA technique to coastal ambient aerosols, *Geophys. Res. Lett.*, 31, L16105, doi:10.1029/2004GL020126, 2004.

- Kahn, R. A., Gaitley, B. J., Garay, M. J., Diner, D. J., Eck, T. F., Smirnov, A., and Holben, B. N.: Multiangle Imaging SpectroRadiometer global aerosol product assessment by comparison with the Aerosol Robotic Network, *J. Geophys. Res.*, 115, D23209, doi:10.1029/2010JD014601, 2010.
- Kalnay et al.: The NCEP/NCAR 40-year reanalysis project, *Bull. Amer. Meteor. Soc.*, 77, 437-470, 1996.
- Karol, Y., Tanré, D., Goloub, P., Ververde, C., Balois, J. Y., Blarel, L., Podvin, T., Mortier, A., and Chaikovsky, A.: Airborne sun photometer PLASMA: concept, measurements, comparison of aerosol extinction vertical profile with lidar, *Atmos. Meas. Tech.*, 6, 2383-2389, 2013.
- Kaskaoutis, D. G., Kharol, S. K., Sifakis, N., Nastos, P. T., Sharma, A. R., Badarinath, K. V. S., and Kambezidis, H. D.: Satellite monitoring of the biomass-burning aerosols during the wildfires of August 2007 in Greece: Climate implications, *Atmos. Environ.*, 45, 716–726, doi:10.1016/j.atmosenv.2010.09.043, 2011.
- Kok, J. F.: A scaling theory for the size distribution of emitted dust aerosols suggests climate models underestimate the size of the global dust cycle, *P. Natl. Acad. Sci. USA*, 108, 1016–1021, doi:10.1073/pnas.1014798108, 2011.
- Kubilay, N., Cokacar, T., and Oguz, T.: Optical properties of mineral dust outbreaks over the northeastern Mediterranean, *J. Geophys. Res.*, 108, 4666, doi:10.1029/2003JD003798, 2003.
- Kumar, D., Rocadenbosch, F., Sicard, M., Comeron, A., Muñoz, C., Lange, D., Tomás, S., and Gregorio, E.: Six-channel polychromator design and implementation for the UPC elastic/Raman LIDAR, in: *SPIE Remote Sens., Int. Soc. Opt. Photon., Prague, Czech Republic, 81820W–81820W*, 2011.
- Lelieveld, J., Berresheim, H., Borrmann, S., Crutzen, P. J., Dentener, F. J., Fischer, H., Feichter, J., Flatau, P. J., Heland, J., Holzinger, R., Korrmann, R., Lawrence, M. G., Levin, Z., Markowicz, K. M., Mihalopoulos, N., Minikin, A., Ramanathan, V., de Reus, M., Roelofs, G. J., Scheeren, H. A., Sciare, J., Schlager, H., Schultz, M., Siegmund, P., Steil, B., Stephanou, E. G., Stier, P., Traub, M., Warneke, C., Williams, J., Ziereis, H.: Global air pollution crossroads over the Mediterranean, *Science*, 298, 794–799, doi:10.1126/science.1075457, 2002.
- Léon, J.F., Augustin, P., Mallet, M., Bourriane, T., Pont, V., Dulac, F., Fourmentin, M., and Lambert, D.: Aerosol vertical distribution, optical properties, and transport over Corsica (western Mediterranean), *Atmos. Chem. Phys. Discuss.*, 15, 9507-9540, 2015.
- Lionello, P., Malanotte-Rizzoli, P., Boscolo, R., Alpert, P., Artale, V., Li, L., Luterbacher, J., May, W., Trigo, R., Tsimplis, M., Ulbrich, U., and Xoplaki, E.: The Mediterranean climate: An overview of the main characteristics and issues, in *The Mediterranean Climate Variability*, P. Lionello, P. Malanotte-Rizzoli and R. Boscolo Eds., *Developments in Earth and Environmental Sciences*, 4, Elsevier, 1-26, 2006.
- Liu, Y., Kahn, R. A., Chaloulakou, A., and Koutrakis, P.: Analysis of the impact of the forest fires in August 2007 on air quality of Athens using multi-sensor aerosol remote sensing data, meteorology and surface observations, *Atmospheric Environment*, 43, 3310–3318, 2009.
- Lyamani, H., Valenzuela, A., Perez-Ramirez, D., Toledano, C., Granados-Muñoz, M.J., Olmo, F.J., Alados-Arboledas, L.: Aerosol properties over the western Mediterranean basin: Temporal and spatial variability, *Atmos. Chem. and Phys.*, 15 (5), 2473-2486, 2015.
- Mailler, S., Menut, L., Di Sarra, A.G., Becagli, S., Di Iorio, T., Formenti, P., Bessagnet, B., Briant, R., Gómez-Amo, J.L., Mallet, M., Rea, G., Siour, G., Sferlazzo, D.M., Traversi, R., Udisti, R., and Turquety, S.: On the radiative impact of aerosols on photolysis rates: comparison of simulations and observations in the Lampedusa island during the ChArMEx/ADRIMED campaign, *Atmos. Chem. Phys. Discuss.*, 15, 7585-7643, doi:10.5194/acpd-15-7585-2015, 2015.
- Mallet, M., Roger, J.C., Despiou, S., Dubovik, O., and Putaud, J.P.: Microphysical and optical properties of aerosol particles in urban zone during ESCOMPTE, *Atmos. Res.*, 69, 73-97, doi:10.1016/j.atmosres.2003.07.001, 2003.
- Mallet, M., Roger, J.C., Despiou, S., Putaud, J.P., and Dubovik, O.: A study of the mixing state of black carbon in urban zone, *J. Geophys. Res.*, 109, D04202, doi:10.1029/2003JD003940, 2004.
- Mallet, M., Van Dingenen, R., Roger, J. C., Despiou, S., and Cachier, H.: In situ airborne measurements of aerosol optical properties during photochemical pollution events. *J. Geophys. Res.*, 110, D03205, doi:10.1029/2004JD005139, 2005.
- Mallet, M., Pont, V., Lioussé, C., Roger, J.C., and Dubuisson, P.: Simulation of aerosol radiative properties with the ORISAM-RAD model during a pollution event (ESCOMPTE 2001), *Atmos. Environ.*, 40, 7696–7705, doi:10.1016/j.atmosenv.2006.08.031, 2006.
- Mallet, M., Gomes, L., Solmon, F., Sellegri, K., Pont, V., Roger, J.C., Missamou, T., and Piazzola, J.: Calculations of key optical properties over the main anthropogenic aerosols over the Western French coastal Mediterranean Sea, *Atmos. Res.*, Vol. 101, doi:10.1016/j.atmosres.2011.03.008, 396-411, 2011.
- Mallet, M., Dubovik, O., Nabat, P., Dulac, F., Kahn, R., Sciare, J., Paronis, D., and Léon, J.F.: Absorption

- properties of Mediterranean aerosols obtained from multi-year ground-based remote sensing observations, *Atmos. Chem. Phys.*, 13, 9195-9210, 2013.
- Markowicz, K. M., Flatau, P. J., Ramana, M. V., Crutzen, P. J., and Ramanathan, V.: Absorbing Mediterranean aerosols lead to a large reduction in the solar radiation at the surface, *Geophys. Res. Lett.*, 29, 1968, doi:10.1029/2002GL015767, 2002.
- Mariotti, A., Zeng, N., Yoon, J., Artale, V., Navarra, A., Alpert, P., and Li, L.Z.X.: Mediterranean water cycle changes: transition to drier 21st century conditions in observations and CMIP3 simulations, *Environ. Res. Lett.*, 3, 044001, doi:10.1088/1748-9326/3/4/044001, 2008.
- Mariotti A., Pan, Y., Zeng, N., and Alessandri, A.: Long-term climate change in the Mediterranean region in the midst of decadal variability, *Clim. Dyn.*, 44, 1437-1456, doi:10.1007/s00382-015-2487-3, 2015.
- Martcorena, B. and Bergametti, G.: Modeling the atmospheric dust cycle 1. Design of a soil-derived dust production scheme, *J. Geophys. Res.*, 100, 16415-16430, 1995.
- McConnell, C. L., Formenti, P., Highwood, E. J., and Harrison, M. A. J.: Using aircraft measurements to determine the refractive index of Saharan dust during the DODO Experiments, *Atmos. Chem. Phys.*, 10, 3081-3098, doi:10.5194/acp-10-3081-2010, 2010.
- Meloni D., Di Sarra, A., DeLuisi, J., Di Iorio, T., Fiocco, G., Junkermann, W., and Pace, G.: Tropospheric aerosols in the Mediterranean: 2. Radiative effects through model simulations and measurements, *J. Geophys. Res.*, 108, 4317, doi:10.1029/2002JD002807, 2003.
- Meloni, D., Di Sarra, A. Di Iorio, T., and Fiocco, G.: Direct radiative forcing of Saharan dust in the Mediterranean from measurements at Lampedusa Island and MISR space-borne observations, *J. Geophys. Res.*, 109, D08206, doi:10.1029/2003JD003960, 2004.
- Meloni, D., Di Sarra, A., Pace, G., and Monteleone, F.: Aerosol optical properties at Lampedusa (Central Mediterranean). 2. Determination of single scattering albedo at two wavelengths for different aerosol types, *Atmos. Chem. Phys.*, 6, 715-727, 2006.
- Meloni, D., Di Sarra, A., Monteleone, F., Pace, G., Piacentini, S., and Sferlazzo, D.M.: Seasonal transport patterns of intense dust events at the Mediterranean island of Lampedusa, *Atmos. Res.*, 88, 134-148, doi:10.1016/j.atmosres.2007.10.007, 2008.
- Meloni, D., Junkermann, W., di Sarra, A., Cacciani, M., De Silvestri, L., Di Iorio, T., Estellés, V., Gómez-Amo, J.L., Pace, G., and Sferlazzo, D.M.: Altitude-resolved shortwave and longwave radiative effects of desert dust in the Mediterranean during the GAMARF campaign: indications of a net daily cooling in the dust layer, *J. Geophys. Res. Atmos.*, 120, doi:10.1002/2014JD022312, 2015.
- Meloni, M., di Sarra, A., Brogniez, G., Denjean, C., De Silvestri, L., Di Iorio, T., Formenti, P., Gomez-Amo, J.-L., Gröbner, J., Kouremeti, N., Mallet, M. and Pace, G.: Simulating vertically resolved SW and LW irradiances and infrared brightness temperatures measured at Lampedusa during the Charmex/ADRIMED campaign, in prep. for this special issue, 2015.
- Menut, L., Bessagnet, B., Khvorostyanov, D., Beekmann, M., Blond, N., Colette, A., Coll, I., Curci, G., Foret, G., Hodzic, A., Mailler, S., Meleux, F., Monge, J.-L., Pison, I., Siour, G., Turquety, S., Valari, M., Vautard, R., and Vivanco, M. G.: CHIMERE 2013: a model for regional atmospheric composition modelling, *Geosci. Model Dev.*, 6, 981-1028, doi: 10.5194/gmd-6-981-2013, 2013.
- Menut, L., Mailler, S., Siour, G., Bessagnet, B., Turquety, S., Rea, G., Briant, R., Mallet, M., Sciare, J., and Formenti, P.: Ozone and aerosols tropospheric concentrations variability analyzed using the ADRIMED measurements and the WRF-CHIMERE models, *Atmos. Chem. Phys. Discuss.*, 15, 3063-3125, doi: 10.5194/acpd-15-3063-20, 2015.
- Millán, M.M., Salvador, R., Mantilla, E., and Kallos, G.: Photooxidant dynamics in the Mediterranean basin in summer: Results from European research projects, *J. Geophys. Res.*, 102, 8811-8823, doi:10.1029/96JD03610, 1997.
- Moosmüller, H., Chakrabarty, R. K., and Arnott, W. P.: Aerosol light absorption and its measurement: A review, *Journal of Quantitative Spectroscopy & radiative transfer*, 100, 844-878, 2009.
- Mulcahy, J. P., O'Dowd, C. D., Jennings, S. G., and Ceburnis, D.: Significant enhancement of aerosol optical depth in marine air under high wind conditions, *Geophys. Res. Letters*, Vol. 35, L16810, doi:10.1029/2008GL034303, 2008.
- Nabat, P., Solmon, F., Mallet, M., Kok, J. F., and Somot, S.: Dust emission size distribution impact on aerosol budget and radiative forcing over the Mediterranean region: a regional climate model approach, *Atmos. Chem. Phys.*, 12, 10545-10567, doi:10.5194/acp-12-10545-2012, 2012.
- Nabat, P., Somot, S., Mallet, M., Chiapello, I., Morcrette, J. J., Solmon, F., Szopa, S., Dulac, F., Collins, W., Ghan, S., Horowitz, L. W., Lamarque, J. F., Lee, Y. H., Naik, V., Nagashima, T., Shindell, D., and Skeie, R.: A 4-D climatology (1979-2009) of the monthly tropospheric aerosol optical depth distribution over the

- Mediterranean region from a comparative evaluation and blending of remote sensing and model products, *Atmos. Meas. Tech.*, 6, 1287-1314, doi:10.5194/amt-6-1287-2013, 2013.
- Nabat, P., Somot, S., Mallet, M., Sanchez-Lorenzo, A., and Wild, M.: Contribution of anthropogenic sulfate aerosols to the changing Euro-Mediterranean climate since 1980, *Geophys. Res. Lett.*, 41, 5605-5611, doi:10.1002/2014GL060798, 2014.
- Nabat, P., Somot, S., Mallet, M., Sevault, F., Chiacchio, M., and Wild, M.: Direct and semi-direct aerosol radiative effect on the Mediterranean climate variability using a coupled regional climate system model, *Clim. Dyn.*, doi:10.1007/s00382-014-2205-6, 2015a.
- Nabat, P., Somot, S., Mallet, M., Michou, M., Sevault, F., Driouech, F., Meloni, D., Di Sarra, A., Di Biagio, C., Formenti, P., Sicard, M., Léon, J.-F., and Bouin, M.-N.: Dust aerosol radiative effects during summer 2012 simulated with a coupled regional aerosol-atmosphere-ocean model over the Mediterranean, *Atmos. Chem. Phys.*, 15, 3303-3326, doi:10.5194/acp-15-3303-2015, 2015b.
- Nicolas, J., Mallet, M., Roberts, G., Denjean, C., Formenti, P., Fresney, E., Sellegri, K., Borgniez, G., Bourrienne, T., Pigué, B., Torres, B., Dubuisson, P., and Dulac, F.: Aerosol direct radiative forcing at a regional scale over the western Mediterranean in summer within the ADRIMED project: airborne observations compared to GAME simulations, *Atmos. Chem. Phys. Discuss.*, in prep. for this special issue, 2015.
- Noilhan, J. and Mahfouf, J.-F.: The ISBA land surface parameterisation scheme, *Global Planet. Change*, 13, 145-159, doi:10.1016/0921-8181(95)00043-7, 1996.
- Ortiz-Amezcuca, P., Guerrero-Rascado, J. L., Granados-Muñoz, M. J., Bravo-Aranda, J. A., Alados-Arboledas, L.: Characterization of atmospheric aerosols for a long range transport of biomass burning particles from canadian forest fires over the southern iberian peninsula in July 2013, *Optica Pura y Aplicada*, 47, 43-49, 2014.
- Otto, S., Bierwirth, E., Weinzierl, B., Kandler, K., Esselborn, M., Tesche, M., Schladitz, A., Wendisch, M., and Trautmann, T.: Solar radiative effects of a Saharan dust plume observed during SAMUM assuming spheroidal model particles, *Tellus B*, 61, 270-296, doi:10.1111/j.1600-0889.2008.00389.x, 2009.
- Pace, G., Meloni, D., and di Sarra, A.: Forest fire aerosol over the Mediterranean basin during summer 2003, *J. Geophys. Res.*, 110, D21202, doi:10.1029/2005JD005986, 2005.
- Pace, G., Di Sarra, A., Meloni, D., Piacentino, S., and Chamard, P.: Aerosol optical properties at Lampedusa (Central Mediterranean). 1. Influence of transport and identification of different aerosol types, *Atmos. Chem. Phys.*, 6, 697-713, 2006.
- Papadimas, C. D., Hatzianastassiou, N., Matsoukas, C., Kanakidou, M., Mihalopoulos, N., and Vardavas, I.: The direct effect of aerosols on solar radiation over the broader Mediterranean basin, *Atmos. Chem. Phys.*, 12, 7165-7185, doi:10.5194/acp-12-7165-2012, 2012.
- Papayannis, A., Balis, D., Amiridis, V., Chourdakis, G., Tsaknakis, G., Zerefos, C., Castanho, A.D.A., Nickovic, S., Kazadzis, S., and Grabowski, J.: Measurements of Saharan dust aerosols over the Eastern Mediterranean using elastic backscatter-Raman lidar, spectrophotometric and satellite observations in the frame of the EARLINET project, *Atmos. Chem. Phys.*, 5, 2065-2079, 2005.
- Papayannis, A., Amiridis, V., Mona, L., Tsaknakis, G., Balis, D., Bösenberg, J., Chaikovski, A., De Tomasi, F., Grigorov, I., Mattis, I., Mitev, V., Müller, D., Nickovic, S., Pérez, C., Pietruczuk, A., Pisani, G., Ravetta, F., Rizi, V., Sicard, M., Trickl, T., Wiegner, M., Gerding, M., Mamouri, R. E., D'Amico, G., and Pappalardo, G.: Systematic lidar observations of Saharan dust over Europe in the frame of EARLINET (2000-2002), *J. Geophys. Res.*, 113, D10204, doi:10.1029/2007JD009028, 2008.
- Pappalardo, G., Amodeo, A., Mona, L., Pandolfi, M., Pergola, N., and Cuomo, V.: Raman lidar observations of aerosol emitted during the 2002 Etna eruption, *Geophys. Res. Lett.*, 31, L05120, doi:10.1029/2003GL019073, 2004.
- Pappalardo, G., Amodeo, A., Apituley, A., Comeron, A., Freudenthaler, V., Linné, H., Ansmann, A., Bösenberg, J., D'Amico, G., Mattis, I., Mona, L., Wandinger, U., Amiridis, V., Alados-Arboledas, L., Nicolae, D., and Wiegner, M.: EARLINET: towards an advanced sustainable European aerosol lidar network, *Atmos. Meas. Tech.*, 7, 2389-2409, doi:10.5194/amt-7-2389-2014, 2014.
- Péré, J.C., Mallet, M., Pont, V., and Bessagnet, B.: Impact of aerosol direct radiative forcing on the radiative budget, surface heat fluxes, and atmospheric dynamics during the heat wave of summer 2013 over western Europe: A modelling study, *J. Geophys. Res.*, 116, D23119, doi:10.1029/2011JD016240, 2011.
- Pérez, C., Sicard, M., Jorba, O., Comerón, A., and Baldasano, J.M.: Summertime re-circulations of air pollutants over the north-eastern Iberian coast observed from systematic EARLINET lidar measurements in Barcelona, *Atmos. Environ.*, 38, 3983-4000, 2004.
- Pérez, C., Nickovic, S., Baldasano, J.M., Sicard, M., Rocadenbosch, F., Cachorro, V.E.: A long Saharan dust event

- over the western Mediterranean: Lidar, sun photometer observations, and regional dust modeling. *J. Geophys. Res.*, 111, D15214, doi:10.1029/2005JD006579, 2006.
- Petzold, A., Onasch, T., Kebedian, P., and Freedman, A.: Intercomparison of a Cavity Attenuated Phase Shift-based extinction monitor (CAPS PMex) with an integrating nephelometer Climate and a filter-based absorption monitor, *Atmos. Meas. Tech.*, 6, 1141–1151, 2013.
- Piazzola, J., Tedeschi, G., and Demoisson, A.: A model for a transport of sea-spray Aerosols in the coastal zone, *Boundary Layer Meteorol.*, 155:329-350, 2015.
- Ramanathan, V., et al.: Indian Ocean experiment: An integrated analysis of the climate forcing and effects of the great Indo-Asian haze, *J. Geophys. Res.*, 106, 28371–28398, doi:10.1029/2001JD900133, 2001.
- Ravetta, F., Ancellet, G., Colette, A., and Schlager, H.: Long-range transport and tropospheric ozone variability in the western Mediterranean region during the Intercontinental Transport of Ozone and Precursors (ITOP-2004) campaign, *J. of Geophys. Res.*, 112, doi:10.1029/2006JD007724, 2007.
- Rea, G., Turquety, S., Menut, L., Briant, R., Mailler, S., and Siour, G.: Source contributions to 2012 summertime aerosols in the Euro-Mediterranean region, *Atmos. Chem. Phys. Discuss.*, 15, 8191–824, doi:10.5194/acpd-15-8191-20, 2015.
- Renard, J.-B., et al.: LOAC: a small aerosol optical counter/sizer for ground-based and balloon measurements of the size distribution and nature of atmospheric particles – Part 1: Principle of measurements and instrument evaluation, *Atmos. Meas. Tech. Discuss.*, 8, 1203-1259, doi:10.5194/amtd-8-1203-2015, 2015a.
- Renard, J.-B., et al.: LOAC: a small aerosol optical counter/sizer for ground-based and balloon measurements of the size distribution and nature of atmospheric particles – Part 2: First results from balloon and unmanned aerial vehicle flights, *Atmos. Meas. Tech. Discuss.*, 8, 1261-1299, doi:10.5194/amtd-8-1261-2015, 2015b.
- Roger, J.C., Mallet, M., Dubuisson, P., Cachier, H., Vermote, E., Dubovik, O., and Despiiau, S.: A synergetic approach for estimating the local direct aerosol forcing: application to an urban zone during the Experience sur Site pour Contraindre les Modèles de Pollution et de Transport d’Emission (ESCOMPTE) experiment, *J. Geophys. Res.*, 111, D13208, doi:10.1029/2005JD006361, 2006.
- Royer, P., Raut, J.-C., Ajello, G., Berthier, S., and Chazette, P.: Synergy between CALIOP and MODIS instruments for aerosol monitoring: application to the Po Valley, *Atmos. Meas. Tech.*, 3, 893-907, doi:10.5194/amt-3-893-2010, 2010.
- Ryder, C. L., Highwood, E. J., Rosenberg, P. D., Trembath, J., Brooke, J. K., Bart, M., Dean, A., Crosier, J., Dorsey, J., Brindley, H., Banks, J., Marsham, J. H., McQuaid, J. B., Sodemann, H., and Washington, R.: Optical properties of Saharan dust aerosol and contribution from the coarse mode as measured during the Fennec 2011 aircraft campaign, *Atmos. Chem. Phys.*, 13, 303-325, doi:10.5194/acp-13-303-2013, 2013.
- Saha, A., Mallet, M., Roger, J.C., Dubuisson, P., Piazzola, J., and Despiiau, S.: One year measurements of aerosol optical properties over an urban coastal site: Effect on local direct radiative forcing, *Atmos. Res.*, 90, 195-202, doi:10.1016/j.atmosres.2008.02.003, 2008.
- Sanchez-Gomez, E., Somot, S., and Mariotti, A.: Future changes in the Mediterranean water budget projected by an ensemble of regional climate models, *Geophys. Res. Lett.*, 36, L21401, doi:10.1029/2009GL040120, 2009.
- Salameh, T., Drobinski, P., Menut, L., Bessagnet, B., Flamant, C., Hodzic, A., and Vautard, R.: Aerosol distribution over the western Mediterranean basin during a Tramontane/Mistral event, *Ann. Geophys.*, 25, 2271-2291, 2007.
- Santese, M., Perrone, M.R., Zakey, A.S., De Tomasi, F., and Giorgi, F.: Modeling of Saharan dust outbreaks over the Mediterranean by RegCM3: case studies, *Atmos. Chem. Phys.*, 10, 133–156, doi:10.5194/acp-10-133-2010, 2010.
- Sassen, K.: Lidar backscatter depolarization technique for cloud and aerosol research, in *Light Scattering by Nonspherical Particles: Theory, Measurements, and Applications*, edited by Mishchenko, M., Hovenier, J.W., and Travis, L.D., Academic Press, 393-417, 1999.
- Schepanski, K., Tegen, I., Laurent, B., Heinold, B., and Macke, A.: A new Saharan dust source activation frequency map derived from MSG-SEVIRI IR-channels, *Geophys. Res. Lett.*, 34, 18803, doi:10.1029/2007GL030168, 2007.
- Sciare, J., Cachier, H., Oikonomou, K., Ausset, P., Sarda-Estève, R., and Mihalopoulos, N.: Characterization of carbonaceous aerosols during the MINOS campaign in Crete, July–August 2001: a multi-analytical approach, *Atmos. Chem. Phys.*, 3, 1743-1757, doi:10.5194/acp-3-1743-2003, 2003.
- Sciare, J., Oikonomou, K., Favez, O., Liakakou, E., Markaki, Z., Cachier, H., and Mihalopoulos, N.: Long-term measurements of carbonaceous aerosols in the Eastern Mediterranean: evidence of long-range transport of biomass burning, *Atmos. Chem. Phys.*, 8, 5551–5563, doi:10.5194/acp-8-5551-2008, 2008.
- Schicker, I., Radanovics, S., and Seibert, P.: Origin and transport of Mediterranean moisture and air *Atmos.*

- Chem. Phys., 10, 5089–5105, doi:10.5194/acp-10-5089-2010, 2010.
- Schroeder, W., Csiszar, I., Giglio, L., and Schmidt, C. C.: On the use of fire radiative power, area, and temperature estimates to characterize biomass burning via moderate to coarse spatial resolution remote sensing data in the Brazilian Amazon, *J. Geophys. Res.*, 115, D21121, doi:10.1029/2009JD013769, 2010.
- Sellegrì, K., Rose, C., Culot, A., Sauvage, S., Roberts, G., Marchand, N., Pey, J., Sciare, J., Bourriane, T., Mallet, M., and Dulac, F.: Spatial extent, occurrence and precursors of nucleation events over the western Mediterranean basin, in prep. for publication in this special issue, 2015.
- Sellitto, P., di Sarra, A., Corradini, S., Boichu, M., Herbin, H., Dubuisson, P., Sèze, G., Meloni, D., Monteleone, F., Merucci, L., Rusaleem, J., Salerno, G., Briole, P., and Legras, B.: Synergistic use of Lagrangian dispersion modelling, satellite- and ground-based remote sensing measurements for the investigation of volcanic plumes: the Mount Etna eruption of 25-27 October 2013, *Atmos. Chem. Phys. Disc.*, submitted to this special issue, 2015.
- Sicard, M., Rocadenbosch, F., Reba, M. N. M., Comerón, A., Tomás, S., García-Vázquez, D., Batet, O., Barrios, R., Kumar, D., and Baldasano, J. M.: Seasonal variability of aerosol optical properties observed by means of a Raman lidar at an EARLINET site over Northeastern Spain, *Atmos. Chem. Phys.*, 11, doi:10.5194/acp-11-175-2011, 2011.
- Sicard, M., Bertolín, S., Mallet, M., Dubuisson, P., and Comerón, A.: Estimation of mineral dust long-wave radiative forcing: sensitivity study to particle properties and application to real cases in the region of Barcelona, *Atmos. Chem. Phys.*, 14, 9213–9231, doi:10.5194/acp-14-9213-2014, 2014a.
- Sicard, M., Bertolín, S., Muñoz, C., Rodríguez, A., Rocadenbosch, F., and Comerón, A.: Separation of aerosol fine- and coarse-mode radiative properties: Effect on the mineral dust longwave, direct radiative forcing, *Geophys. Res. Lett.*, 41, doi:10.1002/2014GL060946, 2014b.
- Sicard, M., Barragan, R., Muñoz-Porcar, C., Comerón, A., Mallet, M., Dulac, F., Pelon, J., Alados-Arboledas, L., Amodeo, A., Boselli, A., Bravo-Aranda, J. A., D'Amico, G., Granados-Muñoz, M. J., Leto, Guerrero-Rascado, J. L., Madonna, F., Mona, L., Pappalardo, G., Perrone, M. R., Burlizzi, P., Rocadenbosch, F., Rodríguez-Gómez, A., Scollo, Spinelli, N., Titos, G., Wang, X., and Zanmar Sanchez, R.: Contribution of EARLINET/ACTRIS to the summer 2013 Special Observing Period of the ChArMEx project, *Óptica Pura y Aplicada*, submitted, 2015a.
- Sicard, M., Barragan, Dulac, F., Alados-Arboledas, L., and Mallet, M.: Aerosol Aerosol optical, microphysical and radiative properties at three regional background insular sites in the western Mediterranean Basin, *Atmos. Chem. Phys. Discuss.*, submitted in this special issue, 2015b.
- Solmon, F., Giorgi, F., and Liousse, C.: Aerosol modelling for regional climate studies: application to anthropogenic particles and evaluation over a European/African domain, *Tellus*, 58B, 51–72, doi:10.1111/j.1600-0889.2005.00155.x, 2006.
- Solmon, F., Mallet, M., Elguindi, N., Giorgi, F., Zakey, A., and Konaré, A.: Dust aerosol impact on regional precipitation over western Africa: mechanisms and sensitivity to absorption properties. *Geophys Res Lett* 35, L24705, doi:10.1029/2008GL035900, 2008.
- Spada, M., Jorba, O., Pérez Garcia-Pando, C., Janjic, Z., and Baldasano, J. M.: Modeling and evaluation of the global sea-salt aerosol distribution: sensitivity to emission schemes and resolution effects at coastal/orographic sites, *Atmos. Chem. Phys.*, 13, 11735–11755, doi:10.5194/acp-13-11735-2013, 2013.
- Tafuro, A.M., Barnaba, F., De Tomasi, F., Perrone, M. R., and Gobbi, G. P.: Saharan dust particle properties over the central Mediterranean, *Atmos. Res.*, 81, 67–93, 2006.
- Tafuro, A. M., Kinne, S., De Tomasi, F., and Perrone, M. R.: Annual cycle of aerosol direct radiative effect over southeast Italy and sensitivity studies, *J. Geophys. Res.*, 112, D20202, doi:10.1029/2006JD008265, 2007.
- Tanré, D., Kaufman, Y. J., Herman, M., and Mattoo, S.: Remote sensing of aerosol properties over oceans using the MODIS/EOS spectral radiances, *J. Geophys. Res.*, 102, 16971–16988, 1997.
- Tanré, D., Bréon, F. M., Deuzé, J. L., Dubovik, O., Ducos, F., Francois, P., Goloub, P., Herman, M., Lifermann, A., and Waquet, F.: Remote sensing of aerosols by using polarized, directional and spectral measurements within the A-Train: the PARASOL mission, *Atmos. Meas. Tech.*, 4, 1383–1395, doi:10.5194/amt-4-1383-2011, 2011.
- Tegen, I., Harrison, S. P., Kohfeld, K. E., and Prentice, I. C.: Impact of vegetation and preferential source areas on global dust aerosol: Results from a model study, *J. Geophys. Res.*, 107, 4576, doi:10.1029/2001JD000963, 2002.
- Thieuleux, F., Moulin, C., Bréon, F. M., Maignan, F., Poitou, J., and Tanré, D.: Remote sensing of aerosols over the oceans using MSG/SEVIRI imagery, *Ann. Geophys.*, 23, 3561–3568, doi:10.5194/angeo-23-3561-2005, 2005.
- Torres, B., Dubovik, O., Fuertes, D., Lapyonok, T., Toledano, C., Schuster, G.L., Goloub, P., Blarel, L., Barreto, A., Mallet, M., and Tanré, D.: Advanced characterization of aerosol properties from measurements of spectral optical thickness of the atmosphere, in prep. for this special issue, 2015.
- Turco, M., Llasat, M.C., Tudela, A., Castro, X., and Provenzale, A.: Decreasing fires in a Mediterranean region

- (1970-2010, NE Spain), *Nat. Hazards Earth Syst. Sci.*, 13, 649-652, doi:10.5194/nhess-13-649-2013, 2013.
- Turquety, S., Menut, L., Bessagnet, B., Anav, A., Viovy, N., Maignan, F., and Wooster, M.: APIFLAME v1.0: high-resolution fire emission model and application to the Euro-Mediterranean region, *Geosci. Model Dev.*, 7, 587-612, 2014.
- Vaishya, A., Jennings, S. G., and O'Dowd, C.: Wind-driven influences on aerosol light scattering in north-east Atlantic air, *Geophys. Res. Lett.*, 39, L05805, doi:10.1029/2011GL050556, 2012.
- Valenzuela, A., Olmo, F. J., Lyamani, H., Antón, M., Quirantes, A., Alados-Arboledas, L.: Aerosol radiative forcing during African desert dust events (2005-2010) over Southeastern Spain, *Atmos. Chem. and Phys.*, 12, 10331-10351, 2012.
- Vialard, J., et al.: Cirene: Air-sea interactions in the Seychelles-Chagos thermocline ridge region, *Bull. Am. Meteor. Soc.*, 90, 45-61, doi:10.1175/2008BAMS2499.1, 2009.
- Wang, Y., Sartelet, K. N., Bocquet, M., Chazette, P., Sicard, M., D'Amico, G., Léon, J. F., Alados-Arboledas, L., Amodeo, A., Augustin, P., Bach, J., Belegante, L., Binietoglou, V., Bush, X., Comerón, A., Delbarre, H., García-Vázquez, D., Guerrero-Rascado, J. L., Hervo, M., Iarlori, M., Kokkalis, P., Lange, D., Molero, F., Montoux, N., Muñoz, A., Muñoz, C., Nicolae, D., Papayannis, A., Pappalardo, G., Preissler, J., Rizi, V., Rocadenbosch, F., Sellegri, K., Wagner, F., and Dulac, F.: Assimilation of lidar signals: application to aerosol forecasting in the western Mediterranean basin, *Atmos. Chem. Phys.*, 14, 12031-12053, doi:10.5194/acp-14-12031-2014, 2014.
- Waquet, F., Cornet, C., Deuzé, J.-L., Dubovik, O., Ducos, F., Goloub, P., Herman, M., Lapyonok, T., Labonnote, L.C., Riedi, J., Tanré, D., Thieuleux, F., and Vanbauce, C.: Retrieval of aerosol microphysical and optical properties above liquid clouds from POLDER/PARASOL polarization measurements, *Atmos. Meas. Tech.*, 6, 991-1016, doi:10.5194/amt-6-991, 2013.
- Wolke, R., Schroeder, W., Schroedner, R., Renner, E.: Influence of grid resolution and meteorological forcing on simulated European air quality: A sensitivity study with the modeling system COSMO-MUSCAT. *Atmos. Environ.*, 53, 110-130, 2012.
- Yue, X., Liao, H., Wang, H.J., Li, S.L., and Tang, J.P.: Role of sea surface temperature responses in simulation of the climatic effect of mineral dust aerosol, *Atmos. Chem. Phys.*, 11, 6049-6062, doi:10.5194/acp-11-6049-2011, 2011.
- Zakey, A. S., Solmon, F., and Giorgi, F.: Implementation and testing of a desert dust module in a regional climate model, *Atmos. Chem. Phys.*, 6, 4687-4704, 2006.
- Zakey, A. S., Giorgi, F., and Bi, X.: Modeling of sea salt in a regional climate model: Fluxes and radiative forcing, *J. Geophys. Res.*, 113, D14221, doi:10.1029/2007JD009209, 2008.
- Zanis, P., Ntogras, C., Zakey, A., Pytharoulis, I., and Karacostas, T.: Regional climate feedback of anthropogenic aerosols over Europe using RegCM3, *Clim. Res.*, V52, 267-278, doi:10.3354/cr01070, 2012.
- Zhu, A., Ramanathan, V., Li, F., and Kim, D.: Dust plumes over the Pacific, Indian, and Atlantic oceans: Climatology and radiative impact, *J. Geophys. Res.*, 112, D16208, doi:10.1029/2007JD008427, 2007.